Imaging and modelling nanoscale dynamics of mineral-mineral and mineral-fluid interfaces during mechano-chemical transformations

Marthe Grønlie Guren

Dissertation submitted for the degree of Philosophiae Doctor

Department of Geosciences
Faculty of Mathematics and Natural Sciences
University of Oslo, Norway

Series of dissertations submitted to the
Faculty of Mathematics and Natural Sciences, University of Oslo
No. 2596

ISSN 1501-7710

Cover: Hanne Baadsgaard Utigard.
Print production: Reprosentralen, University of Oslo.

Acknowledgements

The work with this thesis was carried out at the Njord Center at the Department of Geosciences at the University of Oslo from January 2018 to December 2021. The research presented here was conducted under supervision from François Renard, Anders Malthe-Sørenssen and Henrik Sveinsson.

First and foremost, I would like to thank all my supervisors for guiding me through this project. A special thanks to François Renard for giving me the opportunity to do a PhD and broaden my knowledge in geochemistry. You have always been supportive and an excellent mentor who always have time for discussions.

Henrik, thank you for joining my supervision team (officially) in 2021 and for all your help with the models. We have collaborated since our trip to Los Angeles in 2017 where you and Anders Hafreager introduced me to LAMMPS. I appreciate all the scientific and non-scientific meetings with you and Anders during the last four years.

I would also like to acknowledge the other colleagues and co-authors who contributed to the work presented in this thesis. Especially, I would like to thank Christine Putnis for inviting me several times to Münster to perform experiments with her.

To all my colleagues at the Njord center, thank you for providing a great work environment with time for scientific conversations, coffee breaks and after work beers.

Finally, I would like to thank Eivind for always cheering and proof-reading my writings, and thanks to my family and friends outside of work for all your moral support!

Marthe Grønlie Guren
Oslo, December 2021

Summary

This work describes nanoscale chemical and mechanical interactions along wet and dry mineral interfaces. Overall, it covers two aspects: mineral dissolution and fracturing. Mineral dissolution occurs when a mineral is in contact with a fluid over time and can be observed by a change in mass. For dissolution to proceed, a water film must be in contact with the crystal surface. If the mineral is not in contact with the fluid, the rock must provide a pathway to the mineral by a fracture, or by a fracture network. A fracture network can for example be created by reaction-induced fracturing, which is when a mineral reaction occurs with a change in volume which fractures the surrounding rock, or by exposing a mineral to tensile stress.

In the first project, a calcite crystal in contact with water or a chromium-rich fluid was studied to get a better understanding of dissolution kinetics. The aim was to quantify how the presence of chromium-ions affect dissolution and growth of calcite, and if the formation of nanoparticles at the calcite surface can be used to remove chromium-ions from the solution. The results indicates that chromium can be trapped within nanoparticles, and that the precipitated phase is more stable and more resistant to dissolution than calcite.

In the second project, models of a pore containing water when exposed to compressive stresses were developed to identify at which pressures the fluid is still present. For hydration reactions, the reaction rates of reaction-induced fracturing are thought to be dependent on the access of water to the reacting surfaces. Therefore, a confined water film between two mineral surfaces is studied to find at which stress level the water film is squeezed out from the grain contact, and how this affects the transport properties of the water film. The results indicate that when the pressure reaches a few tens of MPa, the water film collapses which decreases both the water film thickness and the self-diffusion coefficient of the water molecules.

In the third project, a mineral is exposed to tensile stresses to study how a fracture propagates through the material. This is modelled to quantify the rupture speed which controls branching at nanoscale, and the damage produced by the propagating crack and branching. Results from the simulations provide insights into crack propagation in α-quartz and identify the critical velocity for oscillations and crack branching.

Sammendrag

Doktorgradsavhandlingen beskriver småskala kjemiske og mekaniske interaksjoner mellom våte og tørre mineraloverflater. Hovedsakelig dekker den to temaer: Oppløsning og oppsprekking av mineraler, begge på nanoskala. For at oppløsning av mineraler skal skje, må en væske være i kontakt med krystallflaten og det kan observeres ved at det blir en reduksjon i massen til det faste stoffet. For å etablere kontakt mellom væsken og mineralet i en bergart må det finnes en pore, en sprekk eller et nettverk av sprekker. En måte å skape et nettverk av sprekker på er reaksjonsindusert oppsprekking, en prosess der omdannelse av mineralet fører til en økning i volum som sprekker opp materialet rundt, mens en annen er ved å utsette et mineral for strekk.

I det første prosjektet ble en kalsitt krystall eksponert for vann og en krom-rik væske for å studere hvordan kalsitt løses opp i ulike væsker. Målet var å kvantifisere hvordan tilgangen på krom-ioner påvirker oppløsningen og vekst av kalsitt, og om dannelsen av nano-partikler på overflaten til kalsitt kan fjerne krom-ionene fra væsken. Resultatene fra denne studien indikerer at krom kan bli fanget i nano-partikler, og at den nye material-sammensetningen er mer stabil og motstandsdyktig mot oppløsningen enn kalsitt.

I det andre prosjektet ble det modellert en pore som inneholdt vann og poren ble trykket sammen for å studere ved hvilke trykk vannet ville være i kontakt med mineralet. For reaksjoner som skjer på grunn av hydrering antar man at reaksjonshastigheten er kontrollert av tilgangen på vann til overflaten der reaksjonen skjer. Derfor har vi studert en vannfilm under trykk for å bestemme ved hvilket trykk hele vannfilmen blir presset ut av kontaktflaten og hvordan de ulike trykkene påvirker transportegenskapene til vannfilmen. Resultatene indikerer at når trykket når ett par mega-pascal vil vannfilmen kollapse og bli skvist ut og ut av kontakt med krystallflaten.

I det tredje prosjektet blir et mineral utsatt for strekk for å studere hvordan en sprekk beveger seg gjennom materialet. Sprekkhastigheten kontrollerer forgreining og skade i materialet. Resultatene fra simuleringen gir innsikt i hvordan en sprekk beveger seg gjennom kvarts, og identifiserer den kritiske hastigheten for når svingninger og forgreininger oppstår.

Table of contents

Papers

Appendix

Introduction

1. Aim

In the Earth's crust, interactions between aqueous solutions and rocks control critically important processes, from weathering near the Earth's surface to metamorphic reactions in the lower crust. These fluid-rock interactions depend on nanoscale processes along the mineral surfaces. To obtain a better understanding of the nanoscale mineral-mineral and mineral-fluid interactions, I focus on dissolution and coupled dissolution-precipitation processes, the behavior of a confined water film, and dynamic crack propagation under tensile stress (Figure 1).

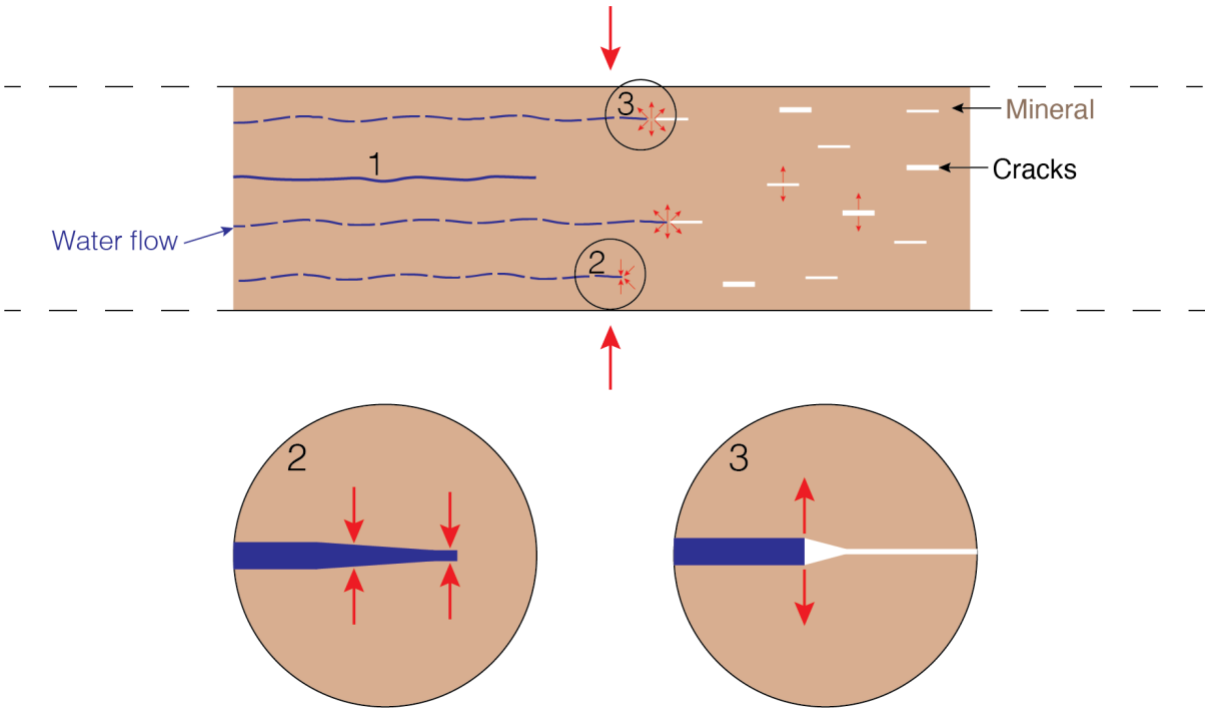

Figure 1: Sketch of a physical system where the processes studied in this thesis occur. Point 1 indicates dissolution as a mineral is in contact with a fluid. Point 2 shows how a water flow might be shut off when the surrounding pressure increases. Point 3 shows how a local tensile stress, e.g., due to hydration reactions with a volume increase, can create fracturing in the mineral.

For dissolution or hydration of minerals to occur, the reacting surface must be in contact with water and if the mineral is not exposed to a fluid, for example in pores, the rock must contain fractures such that the water can travel to the reacting surface. To obtain a better understanding of mineral dissolution kinetics, I have studied dissolution of calcite in a highly saturated solution (Figure 1, point 1). To quantify at which compressive stresses a water film remains stable, i.e., at which pressures hydration of minerals might proceed, I have studied how the thickness and transport properties of a water film changes with pressure (Figure 1, point 2). To

create new fracture surfaces where water might react with the mineral, a quartz crystal was exposed to various tensile stresses (Figure 1, point 3). These simulations do not contain water but allows to quantify the effect of tensile stress and rupture speed causing microbranching and damage in the mineral structure.

The overall aim of this thesis is therefore to provide insights into interactions between mineral-mineral or mineral-fluid interactions at nanoscale. To obtain that, each project (Papers I-III) aims to answer the following questions:

> **Paper I:** How does a $Cr^{(VI)}$-rich solution interact with calcite, and can $Cr^{(VI)}$ be removed from the solution by either a coupled dissolution-precipitation mechanism, adsorption or by Cr-substituted calcite growth?
>
> **Paper II:** What level of stress is necessary to squeeze out a water film from grain contacts, and how does the removal of the water layers influence the transport properties of this water film?
>
> **Paper III:** How does tensile loading affect fracturing of quartz at a molecular level and how does the tensile stress and rupture speed control crack branching and damage generation?

The introduction is structured as follows: Sections 2 and 3 put the work into a scientific context by describing mineral dissolution and mineral-fluid interactions, and nanoscale fracturing. Section 4 gives a short introduction to molecular dynamics simulations and how these simulations can contribute to new understandings of mineral-mineral and mineral-fluid interactions. Section 5 summarizes the content of the manuscripts, which makes up the main body of this thesis, as well as possible future research directions. Then, each manuscript is provided. Two manuscripts are published in international journals, and one manuscript will be submitted later.

2. Basis of mineral dissolution

In Paper I, I studied dissolution of calcite when exposed to water or a chromium-rich solution. The dissolution of minerals in a solution can be observed by a change in mass of the solid and a change in the composition of the solution, and this process has been studied for more than a century to get a better understanding of the dissolution thermodynamics and kinetics (e.g.,

Murray and Renard, 1891; Friedman, 1964; Helgeson, 1969; Bathurst, 1975; Moore, 1989; Johnson et al., 1992; Morse and Mackenzie, 1990; Lasaga, 1998).

Thermodynamic theory describes the equilibria between different phases. The equilibrium constant of a reaction at a given temperature can be described by the change in the standard Gibbs free energy ($\Delta G°$), which is constant for a reaction at a given temperature:

$$\Delta G° = -RT \ln(K_{\mathrm{eq}}) \text{ or } K_{\mathrm{eq}} = \exp\left(-\frac{\Delta G°}{RT}\right) \quad (2.1)$$

where K_{eq} is the thermodynamic equilibrium constant, R is the gas constant and T is the temperature. The equilibrium constant indicates whether reactants or products will be favored at equilibrium, but it does not account for the rate of the reaction (Schroeder, 2000). For an elementary reaction $\mathrm{X} + \mathrm{Y} \rightarrow \mathrm{P}$, the product (P) is favored over the reactants (X, Y) if $\Delta G° < 0$ and the reaction moves in a forward direction (dissolution of mineral X). Conversely, if $\Delta G° > 0$, the reactants are favored over the product and the reaction moves in a reverse direction (precipitation of mineral P). For example, Rimstidt (1997) measured thermodynamic data to find the solubility of quartz (SiO_2) at several temperatures. The dissolution and precipitation of the reaction of quartz is described by:

$$\mathrm{SiO_2(s)} + 2\mathrm{H_2O\ (l)} = \mathrm{H_4SiO_4(aq)} \quad (2.2)$$

Rimstidt (1997) found that e.g., at 25 °C, $\Delta G°(\mathrm{H_4SiO_4}) = -1309.231$ kJ/mol, which means that $\Delta G° < 0$ at 25 °C and quartz will dissolve in pure water. However, the dissolution stops when the solution becomes enriched into H_4SiO_4 and the concentration of this species reaches the equilibrium value, also called solubility.

Kinetics theories describe time dependent processes and provides information about the factors controlling the evolution of a reaction with time. Overall, the rate of any elementary reaction is proportional to the concentration of each reactant, so for $\mathrm{X} + \mathrm{Y} \rightarrow \mathrm{P}$, the dissolution rate is $\frac{\mathrm{d}a_P}{\mathrm{d}t} = k a_{\mathrm{X}} a_{\mathrm{Y}}$, where a is the activity of each species and k is the rate constant (Lasaga, 1998). For water and solid minerals, the activity is taken equal to one, and for the concentration of dissolved species, the activity is their concentration in solution. At equilibrium, the forward (dissolution, k_+) and reverse (precipitation, k_-) reaction rates are equal such that the concentrations of the reactants ([X], [Y]) and the product ([P]) give the equilibrium constant:

$$K_{\mathrm{eq}} = \frac{k_+}{k_-} = \frac{[\mathrm{P}]}{[\mathrm{X}][\mathrm{Y}]} \quad (2.3)$$

The rate of dissolution or precipitation of a mineral is proportional to the surface area in contact with the solution. An example is the dissolution and precipitation of quartz (Rimstidt and Barnes, 1980), where the reaction rate *R* for dissolution is given by:

$$R = \frac{\mathrm{d}m_{\mathrm{H_4SiO_4}}}{\mathrm{d}t} = \frac{A}{M}k_{+} \tag{2.4}$$

where $m_{\mathrm{H_4SiO_4}}$is the concentration of silicic acid in solution (molarity), *A* is the total surface area of silica and *M* is the mass of water in the system. Laboratory experimental data provide values needed to estimate the dissolution rate constant (k_{+}). Since there is a correlation between the equilibrium constant and the ratio of the forward and reverse rate constants (Eq. 2.3), the precipitation rate constant (k_{-}) can be calculated directly from the solubility data.

If one of the reaction rates increases, the system turns into disequilibrium (Morse and Arvidson, 2002). Then, the dissolution rate can be described by adjusting Eq. 2.4 such that it includes the saturation state, $\Omega = \mathrm{IAP}/K_{\mathrm{sp}}$, where IAP is ion activity product and K_{sp} is the solubility product. For carbonate minerals, like calcite, the dissolution rate can be expressed as (e.g., Morse and Berner, 1972; Lasaga, 1998):

$$R = -\frac{\mathrm{d}m_{\mathrm{calcite}}}{\mathrm{d}t} = \left(\frac{A}{V}k\right){k_{\mathrm{sp}}}^{n}(1-\Omega^{n}) \tag{2.5}$$

where m_{calcite} is the concentration of calcite in solution (molarity), *A* is the total surface area of the solid, *V* is the volume of the solution, k is the rate constant and n is a positive constant known as the "order" of reaction, which for calcite was found to be ½ (Sjöberg, 1976).

Several experimental approaches have been used to measure the dissolution rate of calcite, which is the most abundant form of the carbonate minerals, and which is studied in Paper I. However, there is still a gap between dissolution rates measured in the field and in laboratories (Fischer et al., 2014; Noiriel et al., 2020). The estimates of dissolution rates at room temperature and neutral to alkaline conditions differ with almost three orders of magnitude, depending on the method used to obtain the dissolution rate (e.g., Arvidson et al., 2003).

2.1. Measuring dissolution rates in calcite

Bulk dissolution rates have been determined using flow reactors containing mineral powders mixed in aqueous solutions. To determine the dissolution rate, the compositions of input and output solutions flowing through the reactor are measured, and the rates are then normalized relative to the initial total surface area (e.g., Oelkers, 2001; White and Brantley, 2003). A limitation with normalizing over the total surface area is that this parameter might change

during reaction as the total surface area of the crystals, and the reactivity of different surfaces on the same crystal might vary with time (Fischer et al., 2012; Godhino et al., 2012).

To study the specific reactivity of a crystal surface, nano-imaging techniques have been used. Equipment such as atomic force microscopy (AFM), where one can directly observe the dissolution process, have shown that surface topography, or the surface energy landscape of the crystal, plays an important role in the dissolution kinetics (Fischer et al., 2012; Lüttge et al., 2013; Ruiz-Agudo et al., 2014). The AFM, which was used to obtain the main experimental results in Paper I (Figure 2), operates by using a tip that scans across the surface in x- and y-directions while the topography is measured at every (x,y)-position by vertical movement. The tip is attached to a cantilever that has a known spring constant, and the deflection is monitored using a laser, allowing to measure topography of the mineral surface with nanometer height resolution (Rugar and Hansma, 1990; Giessibl, 2003). By adapting a fluid cell, the AFM can be used to observe the dynamics of mineral dissolution and growth *in situ* and studies using AFM provide insightful observations to the contribution of step retreat and etch pits (e.g., MacInnis and Brantley, 1992; Teng, 2004; Ruiz-Agudo and Putnis, 2012).

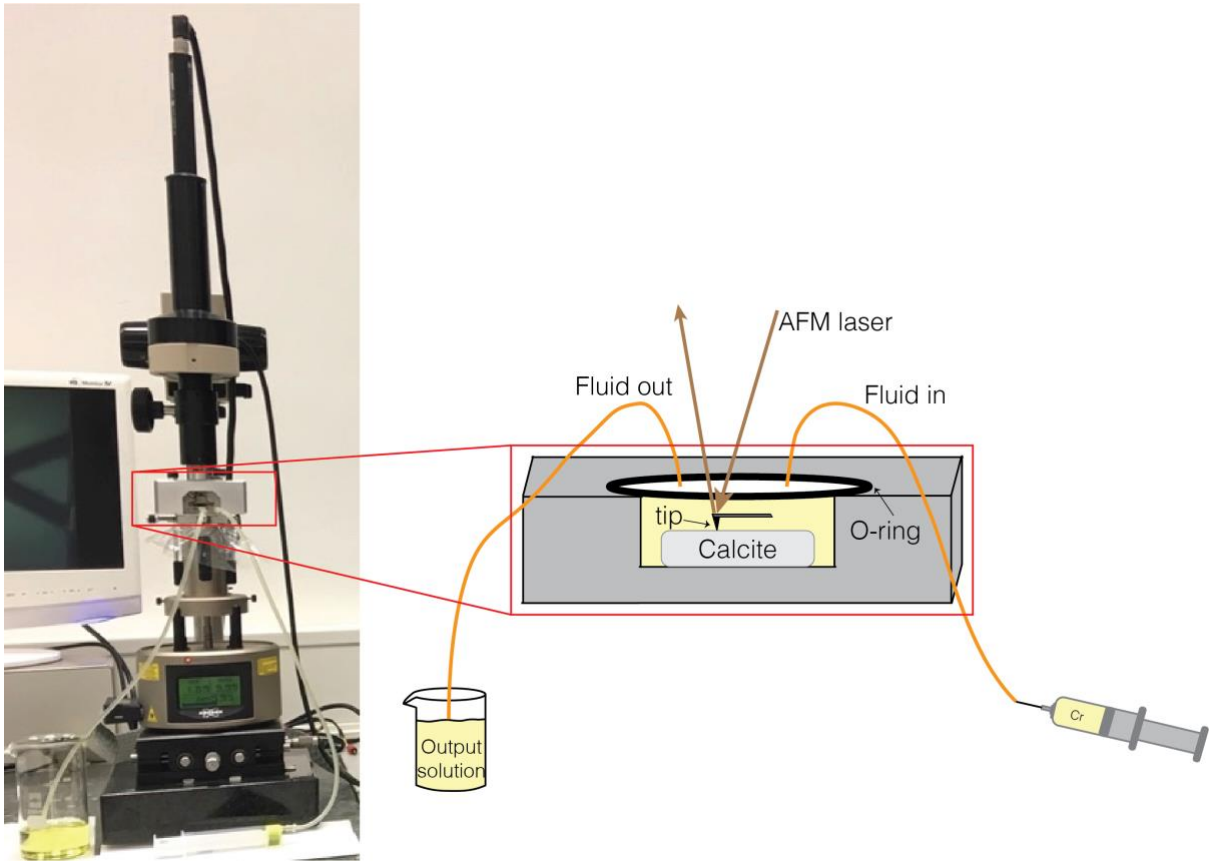

Figure 2: A picture of the Bruker Multimode atomic force microscopy that was used in the experiments in Paper I. The inset sketch shows the tip that scans the mineral surface, the laser, the O-ring creating a fluid cell as well as the tubes to get the solution in and out of the fluid cell (Guren et al., 2020).

The formation of etch pits is a fundamental process in the dissolution of calcite crystals because etch pits correspond to defects in the structure where kink sites and steps can nucleate, favoring dissolution over dissolving atomically flat surfaces (Liang et al., 1996; Ruiz-Agudo and Putnis, 2012). The dissolution rate of calcite at pH 7 is reported to be around $10^{-11.7}$ mol cm^{-2} s^{-1} when measured in the AFM (Arvidson et al., 2003; Ruiz-Agudo et al., 2010), while in mixed flow reactors containing mineral powders and vertical scanning interferometry, the dissolution rate was found to vary from 10^{-9} mol $cm^{-2}s^{-1}$ (Sjöberg, 1978) to 10^{-11} mol $cm^{-2}s^{-1}$ (Arvidson et al., 2003), respectively.

In Paper I, the AFM was used to study dissolution of calcite when exposed to deionized water and a chromium-rich solution. Calcite was chosen because it is the most abundant form of the carbonate minerals, and well-studied, both the dissolution kinetics and its ability to remove toxic ions from a solution. In the experiments, an O-ring was used to create a fluid cell, such that the fluid would be in contact with the calcite surface, and the etch pit retreat of calcite was measured when exposed to deionized water or a solution containing chromium-ions.

A limitation with the AFM experiments is that the observations are limited to two-dimensional surfaces and restricted to small surface areas of a few μm^2, and the technique requires that the surface is well cleaved or polished to become atomically flat. Therefore, the contribution of surface patterns and crystal corners and edges are not accounted for in the AFM measurements. The crystal edges and corners have long been assumed to be highly reactive sites (Schott et al., 1989). Recently, the contribution of different reactivities in various crystal areas have been quantitatively described using time-lapse three-dimensional X-ray micro-tomography (XMT) (Noiriel et al., 2019). By using XMT, the dissolution kinetics of the whole crystal are monitored over time providing information to calculate the local rates of dissolution at the mineral surface (Noiriel et al., 2019; Noiriel et al., 2020). These studies found that, during dissolution, the surface topography is dominated by the formation of etch pits, while the crystal morphology is dominated by the reactivity of the edges and corners of the crystal (Noiriel et al., 2019). The findings from Noiriel et al. (2019) were used to constrain a model that dissolves a calcite crystal.

2.2. Modelling dissolution rates in calcite

Several numerical studies have looked at the reactivity of calcite in water (e.g., De Leeuw et al., 1999; Lardge et al., 2010; Wolthers et al., 2012; Wolthers et al., 2013; Kurganskaya and Luttge, 2016; Kurganskaya and Churakov, 2018; Carrasco et al., 2021). Studies using molecular dynamics simulations have focused on enthalpies for the reactivity at different

crystal sites and confirmed experimental assumptions that reactivity is different for the obtuse and acute steps on a calcite crystal (De Leeuw et al., 1999; Spagnoli et al., 2006). Monte Carlo simulations of dissolution allow observations of the dynamics of surface topography change and characterize dissolution rates over the surface (Wehrli, 1989; Kurganskaya and Luttge, 2016). However, even though carbonate dissolution has been studied in detail with modelling at the microscopic scale, most of the Monte Carlo methods have implemented the experimental observations on an artificial crystal shape, like a Kossel crystal (e.g., Carrasco et al., 2021). The advantage of using a Kossel crystal is that it contains a simple cubic lattice, where one site might represent one molecule or one voxel with pre-defined lengths. Each site can be classified based on the numbers of nearest neighbors (n); one-bonded sites (n=1), two-bonded sites (n=2), corners (n=3), edges (n=4), faces (n=5) or bulk (n=6). The dissolution of a crystal in a far-from-equilibrium solution can be modelled by irreversible detachment of molecules or voxels from the crystal.

To study dissolution in a far-from-equilibrium solution, I have designed a simplified numerical model to simulate crystal dissolution based on the dissolution behavior described in Noiriel et al. (2019), who found that the contribution to dissolution varies over the crystal area. The corners and edges contribute 3.6 and 1.7 times more compared to the crystal faces. In the setup, the crystal is divided into equally shaped voxels, and the number of nearest neighbors (n) are identified at every time step (Figures 3a and b). For simplification, all voxels with n=1, 2 or 3 are considered as corner voxels. This is a preliminary study that was presented at the Goldschmidt conference in 2021. The code is available on Github (https://github.com/marthgg/dissolution).

In the input file, the user defines the detachment probability for each voxel group (V_c= corners, V_e= edges, V_f = faces) and either constructs a crystal shape (e.g., Figure 3a) or reads in a binary file with a predefined crystal shape (e.g., Figure 3b). At every iteration, the number of neighbors is calculated, and the voxels are removed based on the detachment probability. The system was first tested on a Kossel crystal (Figure 3a) before it was extended to a calcite spar crystal (Figure 3b) where the shape was obtained from X-ray microtomography experiments (Noiriel et al., 2019). For a calcite spar crystal, the detachment probability in the experiment was found to be V_c= 67 %, V_e= 24 %, V_f = 9 %.

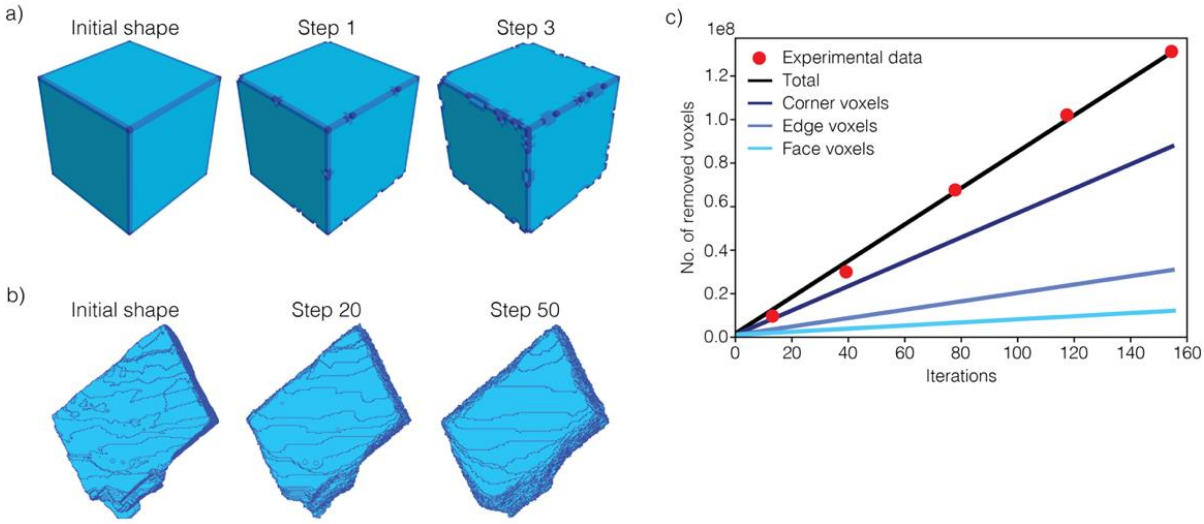

Figure 3: Simulation setup for dissolution of a) a Kossel crystal and b) a calcite spar crystal. In both a) and b), the darkest blue voxels are corners, the intermediate blue voxels are edges, and the light blue voxels are faces. The detachment probability is V_c= 67 %, V_e= 24 % and V_f = 0 %. c) Simulation results for a calcite crystal with detachment probability of V_c= 67 %, V_e= 24 % and V_f = 9 %.

Figure 3c shows that the curve of total removed voxels fits with the experimental data. The results indicate that the total number of voxels at regular intervals fit with the total number of removed voxels measured in the experiment and confirm the variability of reaction rates at different surface sites. In these models, the transport of dissolved materials away from the surface is assumed to be sufficiently fast, such that there will be no precipitation. If the dissolved material is not transported away from the mineral surface, the dissolution process could be coupled with precipitation and be controlled by a boundary layer.

2.3. Implications of a boundary layer

In Paper I, a calcite crystal was in contact with a boundary layer to study coupled dissolution-precipitation and growth processes. In the presence of water, dissolution and precipitation of minerals can be controlled by a boundary layer, i.e., a highly saturated aqueous layer located above the crystal surface, where the atoms might attach or detach from the mineral interface (Figure 4). Coupled dissolution-precipitation can take place when the crystal is dissolved in an insoluble phase, producing a boundary layer that is supersaturated with respect to a more stable phase which might nucleate and precipitate nanoparticles at the surface (Putnis and Putnis, 2007; Ruiz-Agudo et al., 2014), and the kinetics are controlled by a combination of reactions at the mineral surface, nucleation, diffusion in a boundary level, and transport in a moving fluid (Steefel and van Cappellen, 1990; Liu and Deybrodt, 1997). In the bulk fluid and in the boundary layer, the saturation index (SI) of a given mineral is defined as:

$$\mathrm{SI} = \log \Omega = \log \left(\frac{\mathrm{IAP}}{K_{\mathrm{sp}}}\right) \quad (2.6)$$

where Ω is the supersaturation, IAP is the activity product and K_{sp} is the solubility product.

A mineral will dissolve if the aqueous solution is undersaturated (SI<0) with respect to this mineral, while it will precipitate if the aqueous solution is supersaturated (SI>0) with respect to the precipitating phase (Ruiz-Agudo and Putnis, 2012). The whole coupled process has also been proposed to be at the origin of mineral replacement (Putnis, 2002). During the last years, several studies with nanoscale imaging have been performed by using AFM to measure dissolution and precipitation of nanoparticles at siderite and calcite surfaces and quantify how these minerals can trap toxic pollutants (e.g., Renard et al., 2013; 2015; 2017; 2018; Putnis et al., 2013). These studies have shown that the dissolution of a mineral, such as calcite, in the presence of oxyanions in the fluid (e.g., As, Se, Sb) can induce the formation of nanoparticles (Figure 4) that can trap the oxyanions into new minerals, and thereby effectively remove the elements from the solution (Putnis et al., 2021).

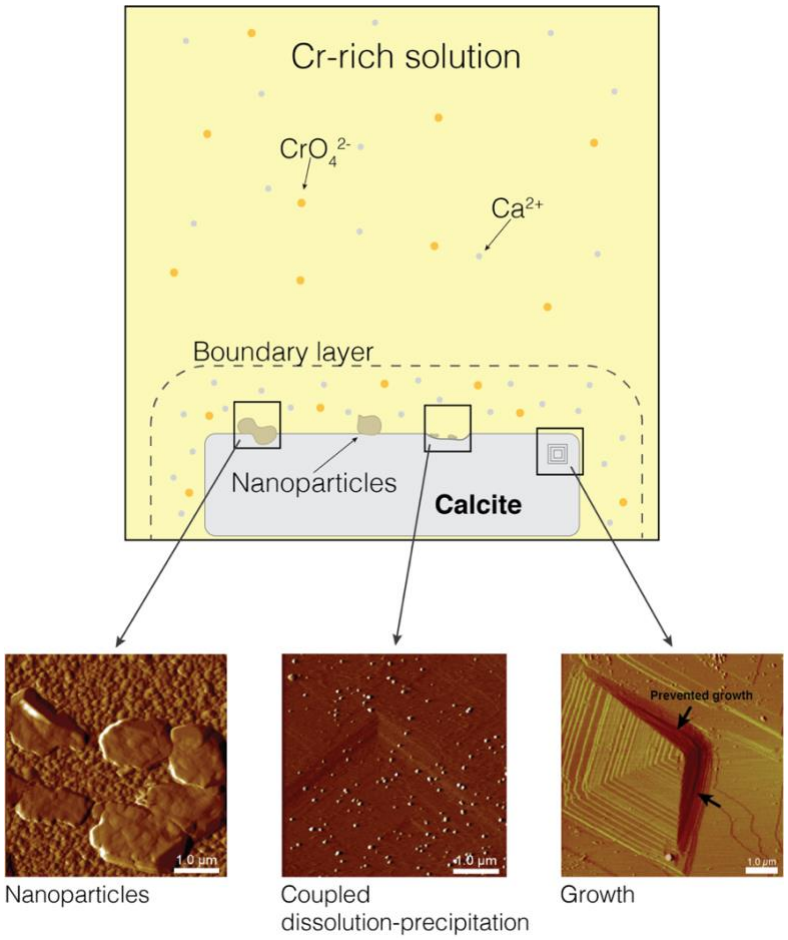

Figure 4: Sketch of a calcite crystal surrounded by a boundary layer in a chromium-rich bulk solution, modified from Putnis et al. (2021). Depending on the saturation index of the boundary layer, nanoparticles can precipitate by a coupled dissolution-precipitation process. Images are from Guren et al. (2020).

If the boundary layer is supersaturated with respect to calcite, growth occurs at the calcite surface. The growing mechanisms on the calcite surface may vary depending on the degree of supersaturation, but can either be by step advancement, by islands growth or by the formation of spirals (Dove and Hochella, 1993; Ruiz-Agudo and Putnis, 2012; Putnis et al., 2021). If the solution also contains small amounts of toxic elements, the growth process might be altered by pinning or blocking of one corner on the growth spiral due to incorporation of other elements.

In Paper I, calcite was exposed to solutions containing small amounts of the toxic element hexavalent chromium, and the aim was to quantify how the presence of chromium-ions affect dissolution and growth of calcite, and if the formation of nanoparticles at the calcite surface could be used to remove the chromium-ions from the solution. Observations from this study indicates that the formation of nanoparticles can be a process that remove chromium-ions from the a solution and that the calcite growth process will be prevented from normal growth.

3. Nanoscale fracturing

Fracturing at nanoscale can reduce the material strength, which has implications for processes that are observed at much larger scales. For example, strength of minerals may control the stability of tectonic faults and their ability to produce earthquakes (e.g., Scholz, 2019). Earthquakes correspond to the propagation of dynamic fractures that initiate at a small scale and propagate over a large distance. The driving force is imposed to the boundaries of the system by tectonic forces. These fractures tend to run along the weakest planes in the crust (i.e., along faults). However, they initiate by the breakage processes at the grain scale, and studies at the atomic scales are therefore important to better understand how the inter-atomic bonds break (Holland and Marder, 1999). Another mechanism to initiate a fracture network is by reaction-induced fracturing where the driving force is imposed internally in the volume. This situation occurs when the hydration of one mineral occurs with a volume increase, leading to volume expansion and fracture generation (Martin and Fyfe, 1970; Jamtveit et al., 2009).

3.1. Reaction-induced fracturing

In Paper II, I studied at which stress a water film is removed from grain contacts to identify at which pressures reaction-induced fracturing might occur. Reaction-induced fracturing happens when a mineral reaction occurs with a change in volume, which produces fractures in the surrounding rock. For example, the hydration of periclase into brucite ($MgO + H_2O = Mg(OH)_2$) occurs with a volume increase of 110 % (Kuleci et al., 2016). Both the hydration of

calcium oxide to portlandite ($CaO + H_2O = Ca(OH)_2$) and the hydration of olivine grains to serpentine occur with a volume increase of 50 % (Kelemen et al., 2011; Malvoisin et al., 2017). At a given temperature, the maximum pressure at which the reaction will stop can be estimated from the force of crystallization (FoC). The calculation of a FoC is based on thermodynamic data of the host and forming mineral (Weyl, 1959; Eq. 13 in Wolterbeek et al., 2018) and indicates when the reaction will reach equilibrium:

$$\sigma_{\mathrm{FoC}} = \frac{\Delta_{\mathrm{f}}G_i^{P,T} + \Delta_{\mathrm{f}}G_{\mathrm{H2O}}^{P,T} - \Delta_{\mathrm{f}}G_j^{P,T}}{V_{m,j}^{P,T} - V_{m,i}^{P,T}} \tag{3.1}$$

where the subscripts i and j correspond to the host mineral and forming mineral, respectively. $\Delta_{\mathrm{f}}G^{P,T}$ is the Gibbs free energy of formation of the species and $V_m^{P,T}$ is the molar volume, both at the given pressure and temperature. The force of crystallization calculated from thermodynamic data and measured in hydration experiments varies with one or two orders of magnitude. For example, experiments on the hydration of calcium oxide to portlandite shows that the reaction slows down around 135 MPa, which is much lower than the thermodynamic limit of 3.4 GPa (Wolterbeek et al., 2018). Similarly, experiments on the hydration of periclase to brucite observed a slowdown of the reaction when the pressure exceeded 30 MPa, while the thermodynamic limit is estimated to 1.9 GPa (Zheng et al., 2018).

Reaction-induced fracturing occurs in a variety of geological and industrial settings, e.g., weathering (Røyne et al., 2008), hydration reactions in the Earth's crust or cement in boreholes (e.g., Martin and Fyfe, 1970; Iyer et al., 2008; Jamtveit et al., 2009; Kelemen and Hirth, 2012; Lafay et al., 2018; Wolterbeek et al., 2018), salt growth and damage (Scherer, 2004), and frost heave and freeze thaw cycles (Walder and Hallet, 1985). In geological settings, a very important metamorphic hydration reaction is serpentinization, which takes place when mafic rocks in the oceanic crust interact with water. The infiltration of water, which initiates the serpentinization, occurs along both small scale microfractures and large-scale faults (e.g., Boudier and Coleman, 1981; Rouméjon and Cannat, 2014; Renard, 2021), by providing pathways for fluids to mineral surfaces where the reaction can proceed.

Figure 5 shows how reaction-induced fracturing progresses and involves feedback loops. To initiate the reaction, one mineral (A) is fractured such that water can access the mineral surface, which causes hydration of this mineral. The newly formed hydrated mineral (B) has a higher specific volume, which increases pressure on the surrounding rock volume. Depending on the stress field, the reaction will either enter a positive or a negative feedback loop (Renard, 2021). In the positive feedback loop, the additional pressure produces fracturing,

which increases the porosity and permeability in the rock and creates new pathways for the fluids to reach new reactive mineral surfaces that become hydrated and new fractures can form. In the negative feedback loop, the volume increase causes a decrease in porosity and permeability, because either the new solid volume fills the pore space (Aharanov et al., 1998), or it has been proposed to be because the pressure closes the existing fractures and squeezes the water out of the grain-grain contacts (Zheng et al., 2018).

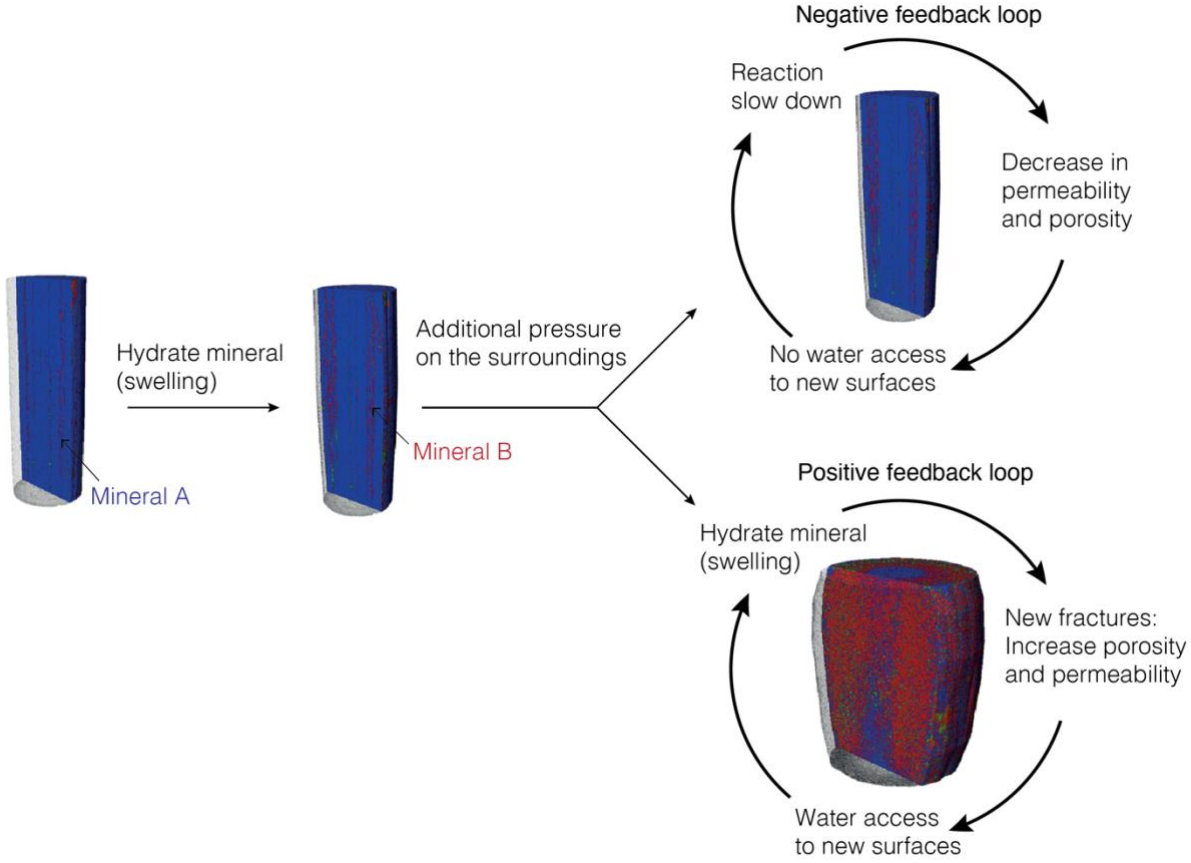

Figure 5: Sketch of the reaction-induced fracturing process. The hydration of a mineral can either lead to a positive feedback loop where the hydration induces the reaction and continues to hydrate the mineral, or it can lead to a negative feedback loop where the reaction is self-limiting and slows down. The mineral cores showing hydration of mineral A to mineral B are from Guren et al. (2021).

Recently, several experimental studies on reaction-induced fracturing have been conducted to better understand the mechanisms that control rock fracturing (e.g., Scherer, 2004; Noiriel et al., 2010; Zheng et al., 2018, 2019; Wolterbeek et al., 2018). Even though the experimental techniques have improved and provided new insights, there are still processes that cannot be fully explained by these experimental observations. Numerical models have therefore been proposed to model reaction-induced fracturing, or a distinct part of the processes that controls the reaction-induced fracturing (e.g., Røyne et al., 2008; Kelemen and Hirth, 2012; Ulven et al., 2014; Malvoisin et al., 2017; Evans et al., 2018; Skarbek et al., 2018; Zhang et al., 2019).

These models used e.g., thermodynamic (Kelemen and Hirth, 2012), 2-D discrete element model (Ulven et al., 2014), 3D discrete element model (Zhang et al., 2019), and micromechanical models combined with observations (Røyne et al., 2008; Malvoisin et al., 2017) and provided insights on subjects such as the crystallization pressure based on the stress due to volume change, and the variations of porosity on the progress of reaction-induced fracturing.

In Paper II, molecular dynamics simulations were used to test a hypothesis that had been raised during experiments: the reaction-induced fracturing slows down at a few MPa because the water is removed from the reacting surface (Zheng et al., 2018). These simulations provide insight into the molecular scale processes, like how the water film thickness varies with increasing pressure. Results indicate that when the pressure increases, the water film is squeezed out from the gain contact where the reaction occurs. This can be linked to which surrounding pressures reaction-induced fracturing will occur at, and whether the reaction will go into a positive feedback loop or a negative feedback loop.

3.2. Dynamic fracture propagation

In brittle materials, dynamic fracture propagation controls the materials strength because crack propagation is the main mode of materials failure. In Paper III, crack propagation in a brittle material (α-quartz) under tensile stress is studied at a molecular level. Processes occurring at the nanoscale have implications for the propagation of fractures across scales and it is known that brittle solids might break abruptly and catastrophically, like earthquakes (e.g., Bouchbinder et al., 2014). Brittle fracturing under tension in minerals is characterized by the breaking of atomic bonds, a process that occurs at all scales of nanometers (Broberg, 1990; Freund, 1990; Buehler, 2008), and creates an open surface while the remaining of the crystal is intact.

There are two types of crack propagation patterns, cracks that propagate straight and cracks that undergo path instabilities, leading to oscillations or crack branching (Figure 6) (e.g., Fineberg and Bouchbinder, 2015). Simple cracks propagate straight along a single fracture plane (Bouchbinder et al., 2010), and the dynamics can be described using the theory of linear elastic fracture mechanics (LEFM) (e.g., Freund, 1990). The assumption in the LEFM is formulated by Griffith's energy balance (Griffith, 1920) which states that a crack will start to propagate when the change in potential energy due to crack growth is the same as the energy necessary to create a new material surface:

$$\frac{\mathrm{d}U}{\mathrm{d}A} = \frac{\mathrm{d}W_\mathrm{p}}{\mathrm{d}A} + \frac{\mathrm{d}W_\mathrm{s}}{\mathrm{d}A} = 0 \tag{3.2}$$

where U is the energy in the system, A is the newly created surface area, W_s is the surface energy and W_p is the potential energy. $\frac{\mathrm{d}W_\mathrm{p}}{\mathrm{d}A} = G$ is the energy release rate and the cracks may propagate when $\mathrm{G} \geq 2\gamma_\mathrm{s}$, where γ_s is the surface energy of the created surface. For a crack in a thin slab with thickness ξ and subject to a tensile stress σ (Figure 6), the strain energy changes when the crack is moving with distance $\mathrm{d}A$.

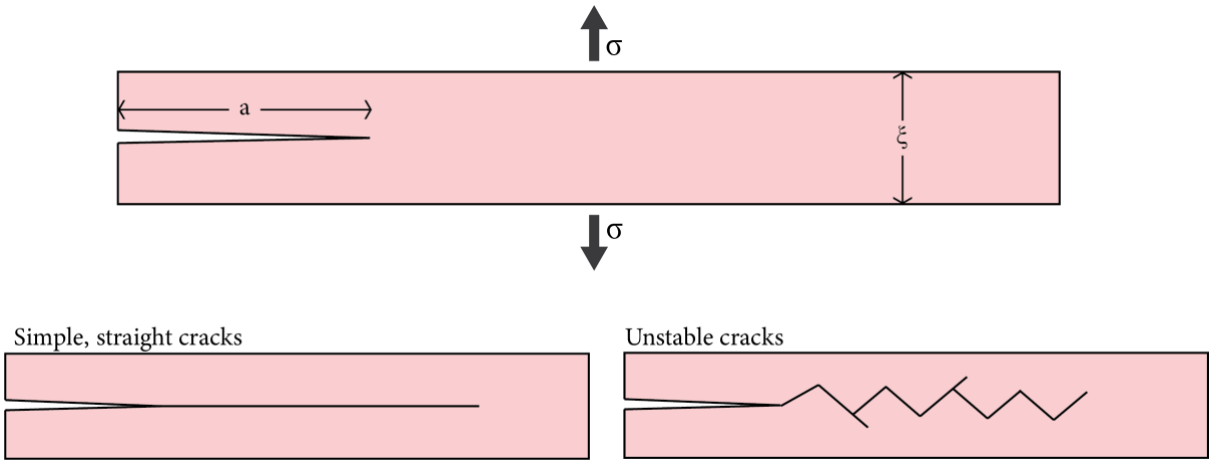

Figure 6: A thin slab geometry loaded with tensile (mode I) stress, with a stress σ. ξ is the thickness of the slab and a is the length of the crack.

The LEFM predictions, i.e., the critical stress for crack propagation, is valid is if the crack does not undergo any path instabilities. For tensile (mode I) cracks in linear elastic materials, the maximum speed the crack can reach is estimated to be the Rayleigh wave speed (C_R). However, simulations have indicated that a crack can reach velocities above the Rayleigh wave speed if the material is hyperelastic (Buehler and Gao, 2006). Experiments on brittle materials have shown that these path instabilities occur at velocities of $0.44C_\mathrm{R}$ for silica glass (Sharon and Fineberg, 1998), $0.36C_\mathrm{R}$ for polymethyl methacrylate (Fineberg et al., 1991; Sharon and Fineberg, 1996) and $0.34C_\mathrm{R}$ for neo-Hookean brittle gels (Livne et al., 2005). The type of fracture propagation varies with speed, and three regimes have been described: mirror, mist, and hackle (Fineberg et al., 1991; Bleyer et al., 2017), where the latter two represent instabilities. At low velocities, the crack surface is flat and follow the cleavage planes (mirror, Figure 7a), then, the crack surface starts to roughen (mist, Figure 7a), while at higher velocities, a more distinct surface roughening occurs with oscillations (hackle, Figure 7b) and microbranching (Figure 7c).

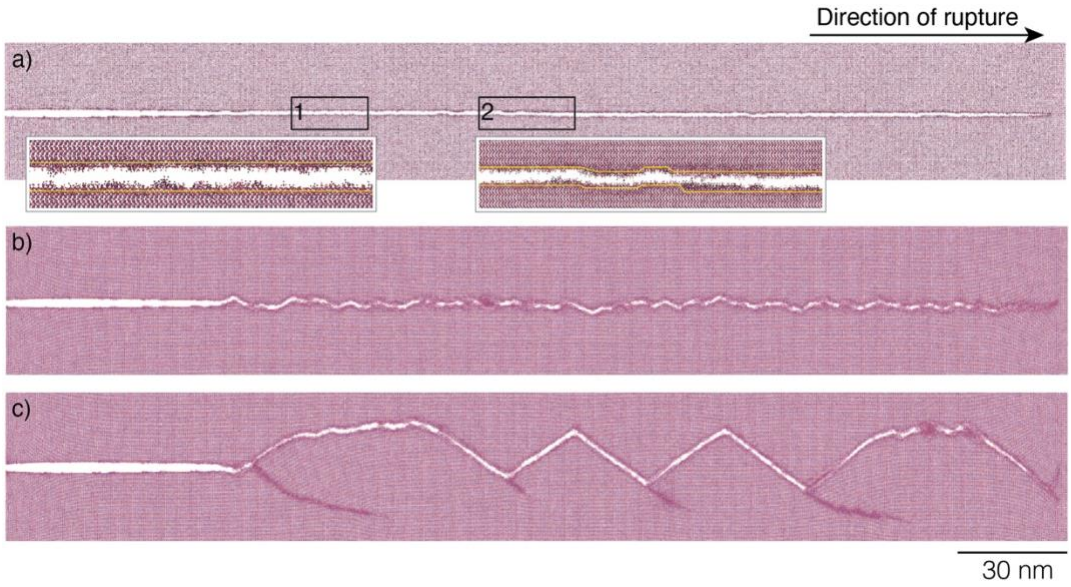

Figure 7: Three snapshots from molecular dynamics simulations show how a brittle material (α-quartz) looks after a crack has propagated through it. The figures progress from a straight crack to a crack that undergo path instabilities. a) A straight crack where 1) indicates a mirror structure and 2) show a mist structure, b) path instability by oscillations and c) path instability by microbranching.

The two types of path instabilities (oscillations and microbranching) have been observed in several brittle materials. In for example polymethyl methacrylate, Fineberg et al. (1991) and Sharon and Fineberg (1996) observed that above a certain speed, the structure changed from featureless to a jagged structure containing oscillations, and they argued that since polymethyl methacrylate is an amorphous material, the source of these oscillations cannot be linked to a material structure. Instead, the occurrence of the oscillations is correlated to a sudden increase in the crack tip speed. If the crack tip speed keeps increasing, the crack might start to branch. The microbranching consists of the break-up of a single crack into multiple cracks such that an ensemble of cracks propagates simultaneously (Fineberg et al., 1991; Fineberg and Bouchbinder 2015). The cracks that branch out from the main crack often occur at a critical speed. Experiments on brittle materials (e.g., Bouchbinder et al., 2014) have indicated that the microbranching is sensitive to the thickness of the system, such that if the thickness of the system is reduced, the microbranching will be suppressed which can increase the rupture speed up to $0.9C_R$.

In Paper III, rupture propagation in α-quartz is studied at a molecular level under conditions of stress that occur during earthquake propagation in the Earth's crust. Our results show that for rupture speeds below $0.15C_R$, a single fracture propagates straight, while at higher speeds fracture propagation undergoes path instabilities. Above $0.15C_R$, the instability is dominated by crack oscillations, while above $0.26C_R$, microbranching occurs.

4. Atomistic simulations

Many processes in mineralogy and geochemistry require an understanding at the atomic level, and the physics underlying the thermodynamics and kinetics of the reactions are described by quantum mechanics (Cygan, 2001; Sherman, 2016). Atomistic simulations are therefore a useful tool when studying processes occurring at an atomistic or molecular scale, and such simulations can be used as a supplement to field observations, experimental measurements, and interpretation of experimental data, as well as for predicting properties of complex systems (Cygan, 2001; Molinari et al., 2016).

Atomistic simulations can be divided into two groups, based on how the interatomic forces are calculated in the simulations: *ab initio* molecular dynamics and classical molecular dynamics. In *ab initio* molecular dynamics, the forces between the atoms can be calculated using density function theory (DFT), while in classical molecular dynamics, the forces are provided by interatomic potentials. One of the greatest advantages of using interatomic potentials is the system size and simulations lengths. For *ab initio* DFT simulations, the systems are limited to a few nanometers and a few hundred atoms, because for every time step, the ground electronic state is found with the Schrödinger equation:

$$\hat{H}\Psi(\mathbf{R},\mathbf{r}) = E\Psi(\mathbf{R},\mathbf{r}) \tag{4.1}$$

where $\hat{H}$ is the Hamiltonian of the system, E is the total energy and Ψ is the many-body wave function describing the system. For classical molecular dynamics simulations, effective interatomic potentials are used, and the system size can reach hundreds of nanometers and the system can contain several million atoms. The interatomic potentials of all interactions are parameterized, providing a description of the potential energy landscape of all interacting particles. Therefore, instead of solving the Schrödinger equation, the 2nd Newton's law is solved to obtain the information of where to move the atoms.

Solving the Schrödinger equation for every time step is extremely computationally expensive. In 2016, I performed *ab initio* DFT simulations to study melting relations in the lower mantle (Hernandez et al., 2021). In these simulations, one of the systems contained 453 atoms and was run for 20,000 timesteps, giving a time trajectory of 20 ps. To obtain this data trajectory, around 60,000 CPU hours were needed, which in waiting time due to parallelization, corresponds to about 40 days. On the other hand, when using interatomic potential (e.g., one of the setups used in Paper II), the system contained around 1,000,000 atoms and with a timestep of 1 fs the time trajectory contained data for 14 ns and the computational power needed was around 4500 CPU hours, or 28 hours in waiting time. Both simulations were run on the

same computer cluster, to make the numbers of CPU hours comparable. There is a continuous improvement in the computational power, so, in the future, it might be possible to run much larger systems using the DFT approach, but the interatomic potentials are still expected to be useful as we can model systems that are closer to the dimensions of systems used in laboratory experiments. However, for classical molecular dynamics simulations to be valid, it is essential that the interatomic potentials are calibrated for the physical properties under which the study is done.

4.1. Interatomic potentials

When using interatomic potentials in molecular dynamics simulations, it is crucial to choose a potential that correctly represents the properties of the simulated material (e.g., density, mechanical strength, elastic properties, etc.). In the simulations performed in Papers II and III, different potentials were used for different materials. For the simulations containing periclase, brucite and water, I used the ClayFF force field (Cygan et al., 2004) for the minerals (periclase and brucite) combined with the single point charge (SPC) water model (Berendsen et al., 1987). For the simulations with α-quartz, I used the Vashishta potential (Broughton et al., 1997). In the following sections, the interatomic potentials that were used in the simulations in Papers II and III are presented. These interatomic potentials are available in LAMMPS (Plimpton, 1995), which is the open-source molecular dynamics program I used for my simulations.

4.1.1. ClayFF force field and SPC water model

The ClayFF force field was developed to model clays and other hydrated minerals in contact with aqueous solutions at the atomic scale, by using non-bonded descriptions of the metal-oxygen interactions in hydrated phases (Cygan et al., 2004). The ClayFF force field is based on the single point charge (SPC) water model (Berendsen et al., 1987) to represent the water, hydroxyl, and oxygen-oxygen interactions. The total energy of the system is described by four parameters: the Coulomb energy (E_{Coul}), the energy of van der Waals interactions (E_{VDW}), the bond stretch energy ($E_{\mathrm{bond\ stretch}}$), and the angle bend energy ($E_{\mathrm{angle\ bend}}$), where the bonded parameters are represented in the SPC water model as harmonic terms (Cygan et al., 2004):

$$E_{\mathrm{total}} = E_{\mathrm{Coul}} + E_{\mathrm{VDW}} + E_{\mathrm{bond\ stretch}} + E_{\mathrm{angle\ bend}} \quad (4.2)$$

The Coulomb and van der Waals interactions are represented by non-bonded interactions, where the Coulomb energy is given by:

$$E_{\mathrm{Coul}} = \frac{e^2}{4\pi\epsilon_0}\sum_{i\neq j}\frac{q_i q_j}{r_{ij}} \tag{4.3}$$

where r_{ij} is the distance between two particles i and j, q_i and q_j are the partial charges, e is the charge of an electron, and ϵ_0 is the dielectric permittivity of vacuum (8.85419 × 10^{-12} F/m). The van der Waals energy is represented by the Lennard-Jones (12-6) potential, which includes short-range repulsion when two atoms approach each other:

$$E_{\mathrm{VDW}} = \sum_{i\neq \mathrm{j}} D_{0,ij}\left[\left(\frac{R_{0,ij}}{r_{ij}}\right)^{12} - 2\left(\frac{R_{0,ij}}{r_{ij}}\right)^{6}\right] \tag{4.4}$$

where $R_{0,ij}$ and $D_{0,ij}$ are empirical parameters derived to fit into the model such that results represent the observed structural and physical properties of the material. To find the parameters for the octahedral magnesium, the experimentally observed structure of brucite was used (Catti et al., 1995; Cygan et al., 2004).

To justify the use of the ClayFF force field for brucite at pressures up to 100 MPa and temperatures in the range 300-519 K, which is the conditions in Paper II and chosen such that the simulations mimic the conditions under which the experiments were performed, I calculated the unit cell parameters of brucite in the pressure range 0-1.5 GPa and temperature range 300-700 K (Figure 8) and compared the results with experimentally measured data on brucite in the same pressure and temperature ranges (Catti et al., 1995; Duffy et al., 1995; Nagai et al., 2000; Fukui et al., 2003). Results indicate that the accuracy of these lattice parameters is reasonable under ambient conditions and up to pressures and temperatures that exceeds the conditions in the simulations. There is a small shift in the unit length of the a-axis of the crystal, of about 5 %, but this shift remains constant through the pressure range. The value of the crystallographic c-axis fits very well the experimental data (Figure 8).

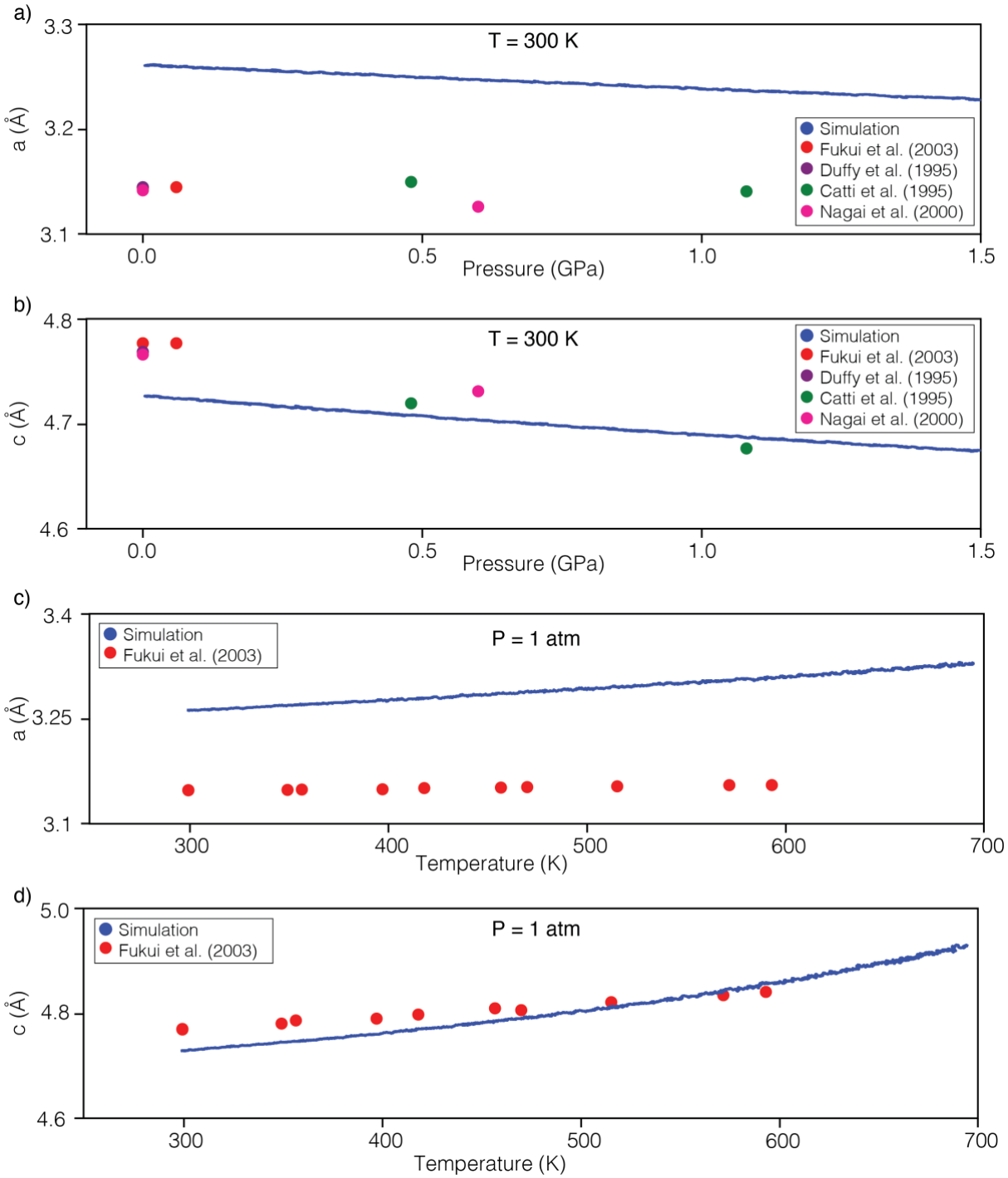

Figure 8: Unit cell parameters for brucite in the pressure range 0-1.5 GPa and temperature range 300-700 K modelled with the ClayFF force field. Changes in the a-axis (a) and c-axis (b) parameter at temperature 300 K in the range 0-1.5 GPa, compared with experimental values from four different studies. Changes in the a-axis (c) and c-axis (d) parameter at pressure 0 GPa and in the temperature range 300-700 K (Guren et al., 2021).

For the SPC water model, the pressure and temperature conditions in the simulations correspond to liquid water and are far from any critical points of solid or vaporized phases. The SPC water model has been reported to overestimate the self-diffusion coefficient of bulk water

at 300 K with self-diffusion coefficients of 3-4×10^{-9} m^2/s (Yu and van Gunsteren, 2004; Guevara-Carrion et al., 2011; Tsimpanogiannis et al., 2019), compared to experimental measurement values of 2.3×10^{-9} m^2/s (e.g., Mills, 1973; Easteal et al., 1989; Holz et al., 2000). My results show that the measured self-diffusion coefficients for bulk water at 300 K and pressures in the range 10-100 MPa are above the experimentally measured values, but within the estimate from previous calculations using the SPC water model (e.g., Yu and van Gunsteren, 2004, Guevara-Carrion et al., 2011).

4.1.2. The Vashishta potential

The Vashishta three-body potential, initially designed by Vashishta et al. (1990), and later modified by Nakano et al. (1994) was designed to describe most of the properties of molten, crystalline, and amorphous silica. The Nakano et al. (1994) version was later adjusted by Broughton et al. (1997) such that the potential more accurately describes the properties of α-quartz. In Paper III, α-quartz is modelled, and the adjusted potential parameters from Broughton et al. (1997) are used. In the potential, the potential energy (U) is the sum of the two-body ($v_{mn}^{(2)}$) and three-body ($v_{mn}^{(3)}$) energy terms:

$$U = \sum_{m<n} v_{mn}^{(2)}(r_{mn}) + \sum_{l,(m<n)} v_{mln}^{(3)}(\boldsymbol{r}_{lm}, \boldsymbol{r}_{ln}) \tag{4.5}$$

$$v_{mn}^{(2)}(r) = A\left(\frac{\sigma_m + \sigma_n}{r}\right)^{\eta_{mn}} + \frac{Z_m Z_n}{r} e^{-\frac{r}{\lambda}} - \frac{\alpha_m Z_n^2 + \alpha_n Z_m^2}{2r^4} e^{-\frac{r}{\zeta}} \tag{4.6}$$

$$v_{mln}^{(3)}(\mathbf{r}_{lm}, \mathbf{r}_{ln}) = B_{mln}\exp\left(\frac{\xi}{r_{lm} - r_0} - \frac{\xi}{r_{ln} - r_0}\right)\left(\frac{\mathbf{r}_{lm}.\mathbf{r}_{ln}}{r_{lm} r_{ln}} - \cos\overline{\theta_{mln}}\right)^2 \Theta(r_0 - r_{lm})\Theta(r_0 - r_{ln}) \tag{4.7}$$

where r is the distance between atoms, and m, n and l are the designated atom indices. The two-body energy term ($v_{mn}^{(2)}(r)$) contains three terms; the short-range repulsion, the Coulomb interaction due to ionicity, and the charge-induced dipole interaction caused by atomic polarizabilities. The three-body energy term ($v_{mln}^{(3)}(\mathbf{r}_{lm}, \mathbf{r}_{ln})$) includes the strength of the three-body interactions and the angles between triplets of atoms. In the potential, only the triplets O-Si-O and Si-O-Si are considered. The equations describing the two- and three-body interactions can be expressed in various ways, and there is a difference in how they are described by Broughton et al. (1997), and in the file that is imported by the program LAMMPS. All necessary parameters for the simulations performed in Paper III are given in the Appendix of Paper III.

To verify that the adjusted potential describes the properties of quartz, Broughton et al. (1997) found that the overall bulk modulus fits with experimental data, and that the individual elastic constants reproduce the anisotropy of the material. To illustrate that the simulated material in Paper III has properties like that of α-quartz, the elastic parameters were calculated (Table 1) and compared with experimental studies (Bechmann, 1958; Mason and Baerwald, 1951), and the parameters measured by Broughton et al. (1997). These elastic parameters show that the material is anisotropic.

Table 1: Elastic constants for α-quartz. Broughton et al. (1997) measured the constants at T=0 K and P=0.1 MPa. My measurements were performed at 1 K and 0.1 MPa. All units are given in GPa.

	Bechmann (1958)	Mason and Baerwald (1951)	Broughton et al., (1997)	Present study
C_{11}	86.74	86.05	69.45	70.04
C_{12}	6.99	5.05	19.27	20.30
C_{13}	11.91	10.45	21.21	24.10
C_{14}	-17.91	18.25	-1.75	3.18
C_{33}	107.20	107.10	74.59	81.05
C_{44}	57.94	58.65	32.22	32.07
C_{66}	39.88	40.50	24.01	23.00

To justify that the Vashishta potential is valid at temperatures in the range 1-520 K, and at pressures in the range 0-3 GPa, which is the conditions for the simulations in Paper III, the density of the material was measured at 0.1 MPa in a temperature range 300-520 K (Figure 9a) and at 298 K in the pressure range 0-12 GPa (Figure 9b). Figure 9a shows that the density is in good agreement with data from Broughton et al. (1997) at 0.1 MPa and all temperatures. At 298 K, the density is slightly lower, but has a similar slope in the range 0-3 GPa, which is within the range in my simulations, while it deviates at higher pressures. Overall, the potential I used is in good agreement with the experimental data up to 3 GPa.

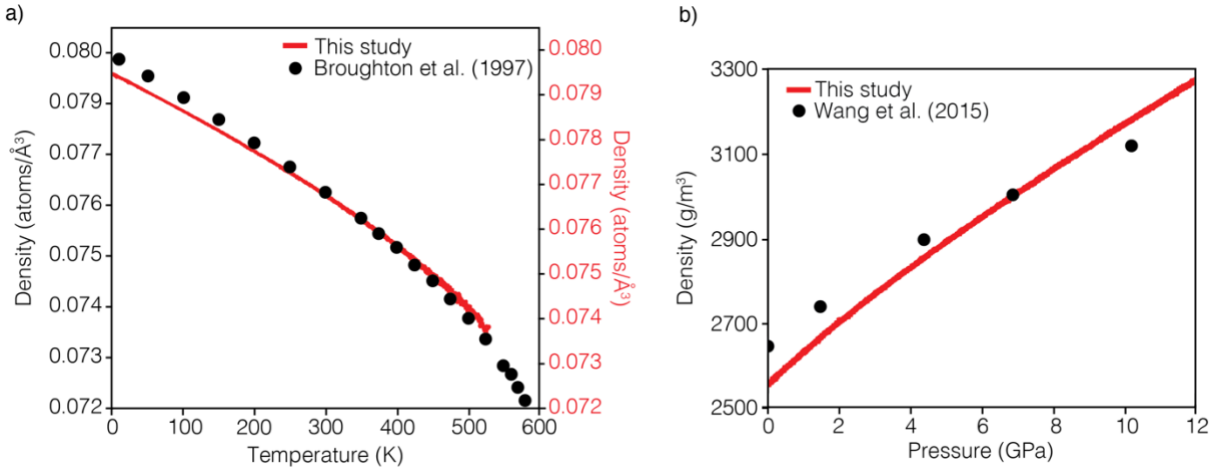

Figure 9: a) Density as a function of temperature at 0.1 MPa. The left y-axis is from Broughton et al. (1997). Notice that there is a jump between 0.077 and 0.079 atoms/Å^3, however, these authors do not provide an explanation for this jump. Therefore, the right y-axis, from my simulations, is also shown and it is continuous from 0.072 to 0.080 atoms/Å^3, i.e., the same range as from Broughton et al. (1997). b) Density as a function of pressure at 298 K.

4.2. Molecular dynamics tools and workflow

The molecular dynamics models in Papers II and III are both performed using LAMMPS. Four main steps are used when performing the simulations: 1) construct the system, 2) provide the input parameters for the simulation, 3) run the simulations, and 4) analyze the output from the simulations. Figure 10 provides a simple overview of the workflow when performing molecular dynamics simulations.

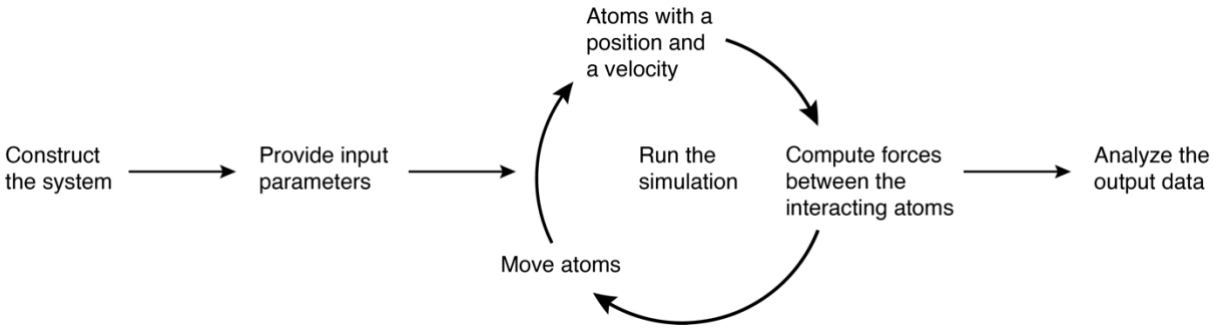

Figure 10: A simple overview of how molecular dynamics simulations are carried out. Based on the input parameters, the forces between the atoms are calculated which is used to move the atoms, and the atoms retrieve a new set of position and velocity. These three steps are repeated at every time step until the end of the simulation.

To construct the system, the user needs to define the unit cell of the crystal, i.e., the smallest replicable unit of a mineral. To create a bulk crystal, the unit cell is replicated in all three cartesian directions until it has lengths of a few nm. After creating a bulk crystal, it can be cut or carved to obtain specific geometries, and the system can contain one or more phases. The system in Paper II contains both a mineral (periclase or brucite) and water, while the system in Paper III contains only one mineral (α-quartz).

The construction of a simulation setup can be quite time consuming. Therefore, along with collaborators at the Njord Centre, I have contributed to create a Python package, called 'molecular-builder' which is hosted on GitHub and can be installed from the Python Package Index: https://pypi.org/project/molecular-builder/ (Sveinsson, 2021). This package simplifies the construction of molecular systems, with focus on input files that can be directly used in simulations with LAMMPS. The package Molecular Builder is developed using Python and is heavily based on the Atomic Simulation Environment (ASE) (Larsen et al., 2017), which generates crystals based on their space group description, and the Open Visualization Tool

(OVITO) (Stukowski, 2009), which creates bonds and write the data into a LAMMPS data input file. Molecular Builder was used to create the α-quartz structure with a pre-cracked notch used in Paper III, and a procedure that creates the brucite and water setup used in Paper II was implemented.

Once the setup is constructed, the user can define the input parameters. The input data file contains the position and velocity of all atoms in the system, while the parameters for the interatomic forces are provided separately. However, before running the simulation, a few more parameters must be specified. The user defines the *time step*, usually on the scale of fs and the *dump frequency*, i.e., how often to save the current state to the output files. The advantage of a high frequency of saving the position and velocities of all atoms is a higher temporal resolution. However, the output data files can be extremely large, so the user must find a compromise between high resolution and manageable file sizes. The *temperature* of the system must be set, and depending on the statistical ensemble, the *pressure* might be needed. In both Papers II and III, I imposed a pressure acting on the boundaries of the simulation domain. The molecular dynamics simulations can be conducted to reproduce given statistical ensembles, and the three most common ensembles are the canonical (NVT), microcanonical (NVE), and the isothermal-isobaric (NPT) ensembles (Allen and Tildesley, 1987). Depending on which ensemble is chosen, some thermodynamic parameters will be held fixed, while the rest can be found by performing various measurements on the system. In both Papers II and III, I used the canonical and the isothermal-isobaric ensembles. Finally, the *length (i.e., the duration) of the simulation* is defined, i.e., how many time iterations are calculated. The simulation length often varies from a few ps to several ns.

After providing all necessary parameters, the simulations are run. The input parameters contain an initial set of position and velocity for each atom, which is used to calculate the interatomic forces between atoms. These forces decides where each atom is moved. The atoms now contain a new position and velocity, and the forces acting on the atoms are calculated again. These three steps (Figure 10) are repeated at every time step until the end of the simulation.

When the simulation is finished the time trajectories are used to do analyze and plot the results. To visualize the behavior of the system with time, the OVITO software was used. OVITO is a 3D visualization software designed for post-processing atomistic data obtained from molecular dynamics simulations, like LAMMPS. During the simulation, the first (~10,000-50,000) time steps contain an equilibration phase where the system adjusts to the given conditions. This phase is therefore not included in the statistical analyses. For the

analyses performed in Papers II and III, I used some of the integrated functions in LAMMPS and OVITO. Parameters that are saved by LAMMPS and have been used extensively to analyze the data output are the pressure of the system, the dimensions of the simulation domain, the temperature, and the potential energy of the system. Other integrated functions that have been used are for example, the mean square displacement (MSD) and velocity autocorrelation function (VACF) of atoms in LAMMPS. These parameters were used to calculate the self-diffusion coefficient of water molecules in Paper II. The coordination analysis in OVITO was used to estimate the position of the crack tip in Paper III. Coordination analysis finds the number of neighbor particles within a cutoff. For example, in a quartz lattice, the coordination of the oxygen atoms is 2, when the cutoff is 1.9 Å. However, the crack surface is characterized by a lower density when the atoms become under coordinated. Therefore, by removing all silicon atoms and the oxygen atoms with a coordination higher than 1, only the oxygen atoms along the fracture surface remain (Figure 11). This procedure might be applied at every time step to obtain the position of the front of the crack while it propagates.

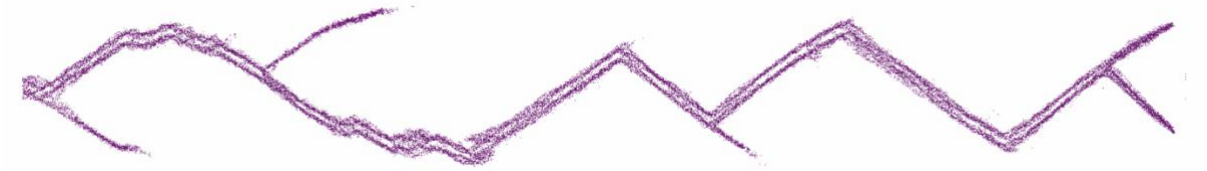

Figure 11: A snapshot of oxygen atoms with a coordination below 2, which are the atoms that provides the fracture surface.

5. Thesis summary

This thesis contains three manuscripts, which represents the main body of the work. The ordering of the manuscripts progresses from an experimental study at nanoscale to numerical models at molecular scale. Overall, the three projects have provided insights into nano-scale processes of mineral dissolution and fracturing. The projects have indicated that the access to water to reacting surfaces might be limited by the compressive stress. When the stress increases, this might shut off the water supply which will limit mineral dissolution and hydration of minerals. However, when the compressive stress is smaller, there will be a constant water flow to the reacting surface, and e.g., dissolution and hydration reactions might progress. If the hydration reaction occurs with a volume increase, the surrounding rock might fracture. These fractures can propagate through the crystal as straight, oscillating or branching cracks, which causes damage in the surrounding material.

5.1. Manuscript summaries

Paper I: Guren, M.G., Putnis, C., Montes-Hernandez, G., King, H. and Renard, F. (2020). Direct imaging of coupled dissolution-precipitation and growth processes on calcite exposed to chromium-rich fluids. *Chemical Geology, 552,* 119770.

Paper I is an experimental study where we used atomic force microscopy to study the coupled dissolution-precipitation and growth process of a calcite surface in contact with a chromium-rich solution. The aim of the paper is to asses if one could use calcite to trap hexavalent chromium ($Cr^{(VI)}$), which is a highly toxic element and a source to pollution of water in areas with industrial activity. Results indicate that chromium-ions can be trapped within nanoparticles at the calcite surface and that the precipitated phase is more stable and more resistant to dissolution than calcite.

Paper II: Guren, M.G., Sveinsson, H.A., Hafreager, A., Jamtveit, B., Malthe-Sørenssen, A. and Renard, F. (2021). Molecular dynamics simulations of confined water in the periclase-brucite system under conditions of reaction-induced fracturing. *Geochimica et Cosmochimica Acta, 294,* 13-27.

Paper II is a molecular dynamics study where we investigate the behavior of a confined water film between two periclase or brucite surfaces. The study builds on experimental studies of reaction-induced fracturing due to the hydration of periclase to brucite, and the aim is to determine at what stress level the water film is squeezed out of the grain contact and how the removal of a water film affects the transport properties. Results indicate that when the pressure reaches a few tens of MPa, the water film collapses which decreases both the water film thickness and the self-diffusion coefficient of the water molecules. We propose that water film collapse decreases the reaction rate of the hydration of periclase due to limited access of water.

Paper III: Guren, M.G., Sveinsson, H.A. and Renard, F. Nanoscale modelling of dynamic rupture and damage production in α-quartz. *In preparation for submission to Geophysical Research Letters.*

Manuscript III is a molecular dynamics study where we simulate dynamic tensile rupture propagation in a α-quartz under conditions of stress that occur during earthquake propagation. The aim is to quantify how rupture speed controls crack branching at nanoscale in α-quartz and

how crack branching produce damage and nanoparticles. Results indicate the crack propagates straight for rupture speeds below 15 % of the Rayleigh wave speed, while path instabilities like oscillations and microbranching occurs when the rupture speed exceeds 15 % of the Rayleigh wave speed. During microbranching, two cracks propagate simultaneously, which produce rock fragments with nanoscale dimensions.

5.2. Possible directions for future work

During the work with this thesis, some questions have been answered, while new questions has been raised. Here, I provide possible directions for further research.

In Paper I, the reactivity between calcite and $Cr^{(VI)}$ was studied experimentally and our main result was that $Cr^{(VI)}$ can be trapped within nanoparticles at the calcite surface and that the precipitated phase is more stable and more resistant to dissolution than calcite. $Cr^{(VI)}$ is one of the most toxic metals, and the removal of chromium from aqueous solutions is particularly important in areas with high industrial activity. Due to a wider use of chromium, the levels of pollution in soil and water have increased, and with the high mobility that chromium-ions have, this might alter the toxicity level of drinking water in the surrounding areas. A continuation of the work on capturing $Cr^{(VI)}$ could be to perform experiments with ettringite or siderite and chromium, as both ettringite and siderite has been reported to be efficient to capture chromium-ions (Zhang and Reardon, 2003; Hajji et al., 2019). Therefore, ettringite and/or siderite might be more efficient to capture chromium from solutions than what was observed with calcite.

In Paper II, the hydration force of a confined water film between periclase or brucite surfaces was determined. For reaction-induced fracturing to proceed, a stable water film is required. Therefore, the stability of a confined water film is likely to have implications for the reaction rate of reaction-induced fracturing, and the simulations provide an explanation for the slow-down of the brucite-forming reaction that is observed in experiments. The slow-down of reaction-induced fracturing is observed in other systems as well, like the hydration of calcium oxide. Therefore, it could be of interest to study a water film between other minerals, either a mineral that has a different crystallographic lattice or a mineral that have a different volume expansion during reaction-induced fracturing and quantify if the pressure where the water film is squeezed out of the grain contact is affected by these parameters. For example, in the hydration reaction of calcium oxide to portlandite, the calcium oxide has the same lattice structure as periclase, but the volume increase during hydration is 50 %, compared to 110 % in the periclase-brucite system.

Manuscript III focuses on dynamic fracture propagation in quartz. The fracture propagation, path instability and damage generation are modelled at a molecular level, and the rupture speed that controls crack branching in quartz is quantified. Dynamic fractures that initiate at a molecular scale have implications for larger scale processes because they break the interatomic bonds, which might weaken the rock, and for example earthquakes corresponds to the propagation of dynamic fractures. In the simulations presented in this thesis, the space between fracture surfaces is a void. A continuation of this work could be to add fluids and/or gases to the simulations as this might change the behavior of the propagating crack and affect the critical speed for path instability.

6. Bibliography

Aharonov, E., Tenthorey, E., & Scholz, C. H. (1998). Precipitation sealing and diagenesis 2. Theoretical analysis. *Journal of Geophysical Research: Solid Earth*, *103*(10), 23969–23981.

Allen, M. P., & Tildesley, D. J. (1987). *Computer simulation of liquids*. Oxford Science Publications.

Arvidson, R. S., Ertan, I. E., Amonette, J. E., & Luttge, A. (2003). Variation in calcite dissolution rates: A fundamental problem? *Geochimica et Cosmochimica Acta*, *67*(9), 1623–1634.

Bathurst, R. G. C. (1975). *Carbonate sediments and their diagenesis* (2nd ed.). Developments in sedimentology 12, Elsevier.

Bechmann, R. (1958). Elastic and piezoelectric constants of alpha-quartz. *Physical Review*, *110*(5), 1060.

Berendsen, H. J. C., Grigera, J. R., & Straatsma, T. P. (1987). The missing term in effective pair potentials. *Journal of Physical Chemistry*, *91*(24), 6269–6271.

Bleyer, J., Roux-Langlois, C., & Molinari, J. F. (2017). Dynamic crack propagation with a variational phase-field model: limiting speed, crack branching and velocity-toughening mechanisms. *International Journal of Fracture*, *204*(1), 79–100.

Bouchbinder, E., Fineberg, J., & Marder, M. (2010). Dynamics of simple cracks. *Annual Review of Condensed Matter Physics*, *1*(1), 371–395

Bouchbinder, E., Goldman, T., & Fineberg, J. (2014). The dynamics of rapid fracture: Instabilities, nonlinearities and length scales. *Reports on Progress in Physics*, *77*(4), 046501.

Boudier, F., & Coleman, R. G. (1981). *Cross section through the peridotite in the Samail ophiolite, southeastern Oman mountains*. *86*(80), 2573–2592.

Broberg, K. B. (1990). *Cracks and fracture*. Academic Press, San Diego, CA.

Broughton, J. Q., Meli, C. A., Vashishta, P., & Kalia, R. K. (1997). Direct atomistic simulation of quartz crystal oscillators: Bulk properties and nanoscale devices. *Physical Review B - Condensed Matter and Materials Physics*, *56*(2), 611–618.

Buehler, M. J., & Gao, H. (2006). Dynamical fracture instabilities due to local hyperelasticity at crack tips. *Nature*, *439*(7074), 307–310.

Buehler, M. J. (2008). *Atomistic modeling of materials failure*. Springer Science & Business Media.

Carrasco, I. S. S., & Aarão Reis, F. D. A. (2021). Modeling the kinetics of calcite dissolution in neutral and alkaline solutions. *Geochimica et Cosmochimica Acta*, *292*, 271–284.

Catti, M., Ferraris, G., Hull, S., & Pavese, A. (1995). Static compression and H disorder in brucite, Mg(OH)2, to 11 GPa: a powder neutron diffraction study. *Physics and Chemistry of Minerals*, *22*(3), 200–206.

Cygan, R. T. (2001). Molecular Modeling in Mineralogy and Geochemistry. *Reviews in Mineralogy and Geochemistry*, *42*(1), 1–35.

Cygan, R. T., Liang, J.-J., & Kalinichev, A. G. (2004). Molecular Models of Hydroxide, Oxyhydroxide, and Clay Phases and the Development of a General Force Field. *The Journal of Physical Chemistry B*, *108*(4), 1255–1266.

De Leeuw, N. H., Parker, S. C., & Harding, J. H. (1999). Molecular dynamics simulation of crystal dissolution from calcite steps. *Physical Review B*, *60*(19), 13792.

Dove, P. M., & Hochella, M. F. (1993). Calcite precipitation mechanisms and inhibition by orthophosphate: In situ observations by Scanning Force Microscopy. *Geochimica et Cosmochimica Acta*, *57*(3), 705–714.

Duffy, T. S., Shu, J., Mao, H. kwang, & Hemley, R. J. (1995). Single-crystal x-ray diffraction of brucite to 14 GPa. *Physics and Chemistry of Minerals*, *22*(5), 277–281.

Easteal, A. J., Price, W. E., & Woolf, L. A. (1989). Diaphragm cell for high-temperature diffusion measurements. Tracer diffusion coefficients for water to 363 K. *Journal of the Chemical Society, Faraday Transactions 1: Physical Chemistry in Condensed Phases*, *85*(5), 1091–1097.

Evans, O., Spiegelman, M., & Kelemen, P. B. (2018). A Poroelastic Model of Serpentinization: Exploring the Interplay Between Rheology, Surface Energy, Reaction, and Fluid Flow. *Journal of Geophysical Research: Solid Earth*, *123*(10), 8653–8675.

Fineberg, J., Gross, S. P., Marder, M., & Swinney, H. L. (1991). Instability in dynamic fracture. *Physical Review Letters*, *67*(4), 457–460.

Fineberg, J., & Bouchbinder, E. (2015). Recent developments in dynamic fracture: some perspectives. *International Journal of Fracture*, *196*(1–2), 33–57.

Fischer, C., Arvidson, R. S., & Lüttge, A. (2012). How predictable are dissolution rates of crystalline material? *Geochimica et Cosmochimica Acta*, *98*, 177–185.

Fischer, C., Kurganskaya, I., Schäfer, T., & Lüttge, A. (2014). Variability of crystal surface reactivity: What do we know? *Applied Geochemistry*, *43*, 132–157.

Freund, L. B. (1990). *Dynamic fracture mechanics*. Cambridge university press.

Friedman, H. L. (1964). Kinetics of thermal degradation of char-forming plastics from thermogravimetry. Application to a phenolic plastic. *Journal of Polymer Science Part C: Polymer Symposia*, *6*(1), 183–195.

Fukui, H., Ohtaka, O., Suzuki, T., & Funakoshi, K. (2003). Thermal expansion of Mg(OH)2 brucite under high pressure and pressure dependence of entropy. *Physics and Chemistry of Minerals*, *30*(9), 511–516.

Giessibl, F. J. (2003). Advances in atomic force microscopy. *Reviews of Modern Physics*, *75*(3), 949.

Godinho, J. R. A., Piazolo, S., & Evins, L. Z. (2012). Effect of surface orientation on dissolution rates and topography of CaF 2. *Geochimica et Cosmochimica Acta*, *86*, 392–403.

Griffith, A. A. (1920). The phenomena of rupture and flow in solids. *Philosophical Transactions of the Royal Society of London. Series A, Containing Papers of a Mathematical or Physical Character*, *221*(582–593), 163–198.

Guevara-Carrion, G., Vrabec, J., & Hasse, H. (2011). Prediction of self-diffusion coefficient and shear viscosity of water and its binary mixtures with methanol and ethanol by molecular simulation. *Journal of Chemical Physics*, *134*(7), 074508.

Guren, M. G., Putnis, C. V., Montes-Hernandez, G., King, H. E., & Renard, F. (2020). Direct imaging of coupled dissolution-precipitation and growth processes on calcite exposed to chromium-rich fluids. *Chemical Geology*, *552*, 119770.

Guren, M. G., Sveinsson, H. A., Hafreager, A., Jamtveit, B., Malthe-Sørenssen, A., & Renard, F. (2021). Molecular dynamics study of confined water in the periclase-brucite system under conditions of reaction-induced fracturing. *Geochimica et Cosmochimica Acta*, *294*, 13–27.

Hajji, S., Montes-Hernandez, G., Sarret, G., Tordo, A., Morin, G., Ona-Nguema, G., Bureau, S., Turki, T., & Mzoughi, N. (2019). Arsenite and chromate sequestration onto ferrihydrite, siderite and goethite nanostructured minerals: Isotherms from flow-through reactor experiments and XAS measurements. *Journal of Hazardous Materials*, *362*, 358–367.

Helgeson, H. C. (1969). Thermodynamics of hydrothermal systems at elevated temperatures and pressures. In *American Journal of Science*, *267*(7), 729–804.

Hernandez, J-A., Mohn, C.E., Guren, M.G., Baron, M.A., & Trønnes, R.G. *Ab initio* molecular dynamics simulations of Ca-perovskite melting. *Submitted to Geophysical Research Letters* (December 2021).

Holland, D., & Marder, M. (1999). Cracks and atoms. *Advanced Materials*, *11*(10), 793–806.

Holz, M., Heil, S. R., & Sacco, A. (2000). Temperature-dependent self-diffusion coefficients of water and six selected molecular liquids for calibration in accurate 1H NMR PFG measurements. *Physical Chemistry Chemical Physics*, *2*(20), 4740–4742.

Iyer, K., Jamtveit, B., Mathiesen, J., Malthe-Sørenssen, A., & Feder, J. (2008). Reaction-assisted hierarchical fracturing during serpentinization. *Earth and Planetary Science Letters*, *267*(3–4), 503–516.

Jamtveit, B., Putnis, C. V., & Malthe-Sørenssen, A. (2009). Reaction induced fracturing during replacement processes. *Contributions to Mineralogy and Petrology*, *157*(1), 127–133.

Johnson, J. W., Oelkers, E. H., & Helgeson, H. C. (1992). SUPCRT92: A software package for calculating the standard molal thermodynamic properties of minerals, gases, aqueous species, and reactions from 1 to 5000 bar and 0 to 1000°C. *Computers & Geosciences*, *18*(7), 899-947.

Kelemen, P. B., Matter, J., Streit, E. E., Rudge, J. F., Curry, W. B., & Blusztajn, J. (2011). Rates and Mechanisms of Mineral Carbonation in Peridotite: Natural Processes and Recipes for Enhanced, in situ CO 2 Capture and Storage. *Annual Review of Earth and Planetary Sciences*, *39*(1), 545–576.

Kelemen, P. B., & Hirth, G. (2012). Reaction-driven cracking during retrograde metamorphism: Olivine hydration and carbonation. *Earth and Planetary Science Letters*, *345*, 81–89.

Kuleci, H., Schmidt, C., Rybacki, E., Petrishcheva, E., & Abart, R. (2016). Hydration of periclase at 350 ∘ C to 620 ∘ C and 200 MPa: experimental calibration of reaction rate. *Mineralogy and Petrology*, *110*(1), 1–10.

Kurganskaya, I., & Luttge, A. (2016). Kinetic Monte Carlo approach to study carbonate dissolution. *The Journal of Physical Chemistry C*, *120*(12), 6482–6492.

Kurganskaya, I., & Churakov, S. V. (2018). Carbonate dissolution mechanisms in the presence of electrolytes revealed by grand canonical and kinetic Monte Carlo Modeling. *The Journal of Physical Chemistry C*, *122*(51), 29285–29297.

Lafay, R., Montes-Hernandez, G., Renard, F., & Vonlanthen, P. (2018). Intracrystalline reaction-induced cracking in olivine evidenced by hydration and carbonation experiments. *Minerals*, *8*(9), 1–18.

Lardge, J. S., Duffy, D. M., Gillan, M. J., & Watkins, M. (2010). Ab initio simulations of the interaction between water and defects on the calcite (101 4) surface. *The Journal of Physical Chemistry C*, *114*(6), 2664–2668.

Larsen, A. H., Mortensen, J. J., Blomqvist, J., Castelli, I. E., Christensen, R., Dułak, M., Friis, J., Groves, M. N., Hammer, B., Hargus, C., Hermes, E. D., Jennings, P. C., Jensen, P. B., Kermode, J., Kitchin, J. R., Kolsbjerg, E. L., Kubal, J., Kaasbjerg, K., Lysgaard, S., Maronsson, J. B., Maxson, T., Olsen, T., Pastewka, L., Peterson, A., Rostgaard, C., Schiøtz, J., Schütt, O., Strange, M., Thygesen, K. S., Vegge, T., Vilhelmsen, L., Walter, M., Zeng, Z., Jacobsen, K. W. (2017). The atomic simulation environment - A Python library for working with atoms. *Journal of Physics Condensed Matter*, *29*(27), 273002.

Lasaga, A. C. (1998). *Kinetic Theory in the Earth Sciences*. Princeton University Press.

Liang, Y., Baer, D. R., McCoy, J. M., Amonette, J. E., & LaFemina, J. P. (1996). Dissolution kinetics at the calcite-water interface. *Geochimica et Cosmochimica Acta*, *60*(23), 4883–4887.

Liu, Z., & Dreybrodt, W. (1997). Dissolution kinetics of calcium carbonate minerals in H2O-CO2 solutions in turbulent flow: The role of the diffusion boundary layer and the slow reaction H2O+CO2=H+ + HCO3-. *Geochimica et Cosmochimica Actamica And*, *61*(14), 2879–2889.

Livne, A., Cohen, G., & Fineberg, J. (2005). Universality and hysteretic dynamics in rapid fracture. *Physical Review Letters*, *94*(22), 224301.

Lüttge, A., Arvidson, R. S., & Fischer, C. (2013). A stochastic treatment of crystal dissolution kinetics. *Elements*, *9*(3), 183–188.

MacInnis, I. N., & Brantley, S. L. (1992). The role of dislocations and surface morphology in calcite dissolution. *Geochimica et Cosmochimica Acta*, *56*(3), 1113–1126.

Malvoisin, B., Brantut, N., & Kaczmarek, M. A. (2017). Control of serpentinisation rate by reaction-induced cracking. *Earth and Planetary Science Letters*, *476*, 143–152.

Martin, B., & Fyfe, W. S. (1970). Some experimental and theoretical observations on the kinetics of hydration reactions with particular reference to serpentinization. *Chemical Geology*, *6*, 185–202.

Mason, W. P., & Baerwald, H. (1951). Piezoelectric crystals and their applications to ultrasonics. *Physics Today*, *4*(5), 23.

Mills, R. (1973). Self-diffusion in normal and heavy water in the range 1-45°. *Journal of Physical Chemistry*, *77*(5), 685–688.

Molinari, M., Brukhno, A. V, Parker, S. C., & Spagnoli, D. (2016). Force field application and development. *Molecular Modeling of Geochemical Reactions: An Introduction*, John Wiley & Sons Ltd, USA, 33-76.

Moore, C. H. (1989). *Carbonate diagenesis and porosity*. Developments in sedimentology 46, Elsevier.

Morse, J. W., & Berner, R. A. (1972). Dissolution kinetics of calcium carbonate in sea water; I, A kinetic origin for the lysocline. In *American Journal of Science*, *272*(9), 840–851.

Morse, J. W., & Mackenzie, F. T. (1990). *Geochemistry of sedimentary carbonates*. Elsevier.

Morse, J. W., & Arvidson, R. S. (2002). The dissolution kinetics of major sedimentary carbonate minerals. *Earth-Science Reviews*, *58*(1–2), 51–84.

Murray, J., & Renard, A. F. (1891). *Report on deep-sea deposits based on the specimens collected during the voyage of HMS Challenger in the years 1872 to 1876*. HM Stationary Office.

Nagai, T., Hattori, T., & Yamanaka, T. (2000). Compression mechanism of brucite: An investigation by structural refinement under pressure. *American Mineralogist*, *85*(5–6), 760–764.

Nakano, A., Kalia, R. K., & Vashishta, P. (1994). First sharp diffraction peak and intermediate-range order in amorphous silica: finite-size effects in molecular dynamics simulations. *Journal of Non-Crystalline Solids*, *171*(2), 157–163.

Noiriel, C., Renard, F., Doan, M. L., & Gratier, J. P. (2010). Intense fracturing and fracture sealing induced by mineral growth in porous rocks. *Chemical Geology*, *269*(3–4), 197–209.

Noiriel, C., Oursin, M., Saldi, G., & Haberthür, D. (2019). Direct Determination of Dissolution Rates at Crystal Surfaces Using 3D X-ray Microtomography. *ACS Earth and Space Chemistry*, *3*(1), 100–108.

Noiriel, C., Oursin, M., & Daval, D. (2020). Examination of crystal dissolution in 3D: A way to reconcile dissolution rates in the laboratory? *Geochimica et Cosmochimica Acta*, *273*, 1–25.

Oelkers, E. H. (2001). General kinetic description of multioxide silicate mineral and glass dissolution. *Geochimica et Cosmochimica Acta*, *65*(21), 3703–3719.

Plimpton, S. (1995). Fast Parallel Algorithms for Short – Range Molecular Dynamics. *Journal of Computational Physics*, *117*(1), 1–19.

Putnis, A. (2002). Mineral replacement reactions: from macroscopic observations to microscopic mechanisms. *Mineralogical Magazine*, *66*(5), 689–708.

Putnis, A., & Putnis, C. V. (2007). The mechanism of reequilibration of solids in the presence of a fluid phase. *Journal of Solid State Chemistry*, *180*(5), 1783–1786.

Putnis, C. V., Renard, F., King, H. E., Montes-Hernandez, G., & Ruiz-Agudo, E. (2013). Sequestration of selenium on calcite surfaces revealed by nanoscale imaging. *Environmental Science and Technology*, *47*(23), 13469–13476

Putnis, C. V., Wang, L., Ruiz-Agudo, E., Ruiz-Agudo, C., & Renard, F. (2021). Crystallization via nonclassical pathways: Nanoscale imaging of mineral surfaces [Chapter]. *ACS Symposium Series*, *1383*, 1–35.

Renard, F., Montes-Hernandez, G., Ruiz-Agudo, E., & Putnis, C. V. (2013). Selenium incorporation into calcite and its effect on crystal growth: An atomic force microscopy study. *Chemical Geology*, *340*, 151–161.

Renard, F., Putnis, C. V., Montes-Hernandez, G., Ruiz-Agudo, E., Hovelmann, J., & Sarret, G. (2015). Interactions of arsenic with calcite surfaces revealed by in situ nanoscale imaging. *Geochimica et Cosmochimica Acta*, *159*, 61–79.

Renard, F., Putnis, C. V., Montes-Hernandez, G., & King, H. E. (2017). Siderite dissolution coupled to iron oxyhydroxide precipitation in the presence of arsenic revealed by nanoscale imaging. *Chemical Geology*, *449*, 123–134.

Renard, F., Putnis, C. V., Montes-Hernandez, G., King, H. E., Breedveld, G. D., & Okkenhaug, G. (2018). Sequestration of Antimony on Calcite Observed by Time-Resolved Nanoscale Imaging. *Environmental Science and Technology*, *52*(1), 107–113.

Renard, F. (2021). Reaction-Induced Fracturing: When Chemistry Breaks Rocks. *Journal of Geophysical Research: Solid Earth*, *126*(2), e2020JB021451.

Rimstidt, J. D., & Barnes, H. L. (1980). The kinetics of silica-water reactions. *Geochimica et Cosmochimica Acta*, *44*(11), 1683–1699.

Rimstidt, J. D. (1997). Quartz solubility at low temperatures. *Geochimica et Cosmochimica Acta*, *61*(13), 2553–2558.

Rouméjon, S., & Cannat, M. (2014). Serpentinization of mantle-derived peridotites at mid-ocean ridges: Mesh texture development in the context of tectonic exhumation. *Geochemistry, Geophysics, Geosystems*, *15*(6), 2354–2379.

Rugar, D., & Hansma, P. (1990). Atomic force microscopy. *Physics Today*, *43*(10), 23–30.

Ruiz-Agudo, E., Kowacz, M., Putnis, C. V., & Putnis, A. (2010). The role of background electrolytes on the kinetics and mechanism of calcite dissolution. *Geochimica et Cosmochimica Acta*, *74*(4), 1256–1267.

Ruiz-Agudo, E., & Putnis, C. V. (2012). Direct observations of mineral fluid reactions using atomic force microscopy: the specific example of calcite. *Mineralogical Magazine*, *76*(01), 227–253.

Ruiz-Agudo, E., Putnis, C. V., & Putnis, A. (2014). Coupled dissolution and precipitation at mineral-fluid interfaces. *Chemical Geology*, *383*, 132–146.

Røyne, A., Jamtveit, B., Mathiesen, J., & Malthe-Sørenssen, A. (2008). Controls on rock weathering rates by reaction-induced hierarchical fracturing. *Earth and Planetary Science Letters*, *275*(3–4), 364–369.

Scherer, G. W. (2004). Stress from crystallization of salt. *Cement and Concrete Research*, *34*(9), 1613–1624.

Scholz, C. H. (2019). *The mechanics of earthquakes and faulting*. Cambridge university press.

Schott, J., Brantley, S., Crerar, D., Guy, C., Borcsik, M., & Willaime, C. (1989). Dissolution kinetics of strained calcite. *Geochimica et Cosmochimica Acta*, *53*(2), 373–382.

Sharon, E., & Fineberg, J. (1996). Microbranching instability and the dynamic fracture of brittle materials. *Physical Review B - Condensed Matter and Materials Physics*, *54*(10), 7128–7139.

Sharon, E., & Fineberg, J. (1998). Universal features of the microbranching instability in dynamic fracture. *Philosophical Magazine B*, *78*(2), 243–251.

Sherman, D. M. (2016). Introduction to the Theory and Methods of Computational Chemistry. *Molecular Modeling of Geochemical Reactions: An introduction.* John Wiley & Sons Ltd., USA, 1–31.

Schroeder, D. V. (2000). *An introduction to thermal physics*. Addison Wesley Longman.

Sjöberg, E. L. (1976). A fundamental equation for calcite dissolution kinetics. *Geochimica et Cosmochimica Acta*, *40*(4), 441–447.

Sjöberg, E. L. (1978). Kinetics and mechanism of calcite dissolution in aqueous solutions at low temperatures. *Stockholm Contrib. Geol.*, *32*(92).

Skarbek, R. M., Savage, H. M., Kelemen, P. B., & Yancopoulos, D. (2018). Competition Between Crystallization-Induced Expansion and Creep Compaction During Gypsum Formation, and Implications for Serpentinization. *Journal of Geophysical Research: Solid Earth*, *123*(7), 5372–5393.

Spagnoli, D., Kerisit, S., & Parker, S. C. (2006). Atomistic simulation of the free energies of dissolution of ions from flat and stepped calcite surfaces. *Journal of Crystal Growth*, *294*(1), 103–110.

Steefel, C. I., & Van Cappellen, P. (1990). A new kinetic approach to modeling water-rock interaction: The role of nucleation, precursors, and Ostwald ripening. *Geochimica et Cosmochimica Acta*, *54*(10), 2657–2677.

Stukowski, A. (2009). Visualization and analysis of atomistic simulation data with OVITO–the Open Visualization Tool. *Modelling and Simulation in Materials Science and Engineering*, *18*(1), 15012.

Sveinsson (2021). molecular-builder (0.3.1). Zenodo. https://doi.org/10.5281/zenodo.5709801

Teng, H. H. (2004). Controls by saturation state on etch pit formation during calcite dissolution. *Geochimica et Cosmochimica Acta*, *68*(2), 253–262.

Tsimpanogiannis, I. N., Moultos, O. A., Franco, L. F. M., Spera, M. B. d. M., Erdős, M., & Economou, I. G. (2019). Self-diffusion coefficient of bulk and confined water: a critical review of classical molecular simulation studies. *Molecular Simulation*, *45*(4–5), 425–453.

Ulven, O. I., Jamtveit, B., & Malthe-Sørenssen, A. (2014). Reaction-driven fracturing of porous rock. *Journal of Geophysical Research: Solid Earth*, *119*(10), 7473-7486.

Vashishta, P., Kalia, R. K., Rino, J. P., & Ebbsjö, I. (1990). Interaction potential for SiO 2: A molecular-dynamics study of structural correlations. *Physical Review B*, *41*(17), 12197.

Walder, J., & Hallet, B. (1985). Theoretical Model of the Fracture of Rock During Freezing. *Bulletin of the Geological Society of America*, *96*(3), 336–346.

Wang, J., Mao, Z., Jiang, F., & Duffy, T. S. (2015). Elasticity of single-crystal quartz to 10 GPa. *Physics and Chemistry of Minerals*, *42*(3), 203–212.

Wehrli, B. (1989). Monte Carlo simulations of surface morphologies during mineral dissolution. *Journal of Colloid and Interface Science*, *132*(1), 230–242.

Weyl, P. K. (1959). Pressure solution and the force of crystallization: a phenomenological theory. *Journal of Geophysical Research*, *64*(11), 2001–2025

White, A. F., & Brantley, S. L. (2003). The effect of time on the weathering of silicate minerals: Why do weathering rates differ in the laboratory and field? *Chemical Geology*, *202*(3–4), 479–506.

Wolterbeek, T. K. T., van Noort, R., & Spiers, C. J. (2018). Reaction-driven casing expansion: potential for wellbore leakage mitigation. *Acta Geotechnica*, *13*(2), 341–366.

Wolthers, M., Di Tommaso, D., Du, Z., & de Leeuw, N. H. (2012). Calcite surface structure and reactivity: molecular dynamics simulations and macroscopic surface modelling of the calcite–water interface. *Physical Chemistry Chemical Physics*, *14*(43), 15145–15157.

Wolthers, M., Di Tommaso, D., Du, Z., & de Leeuw, N. H. (2013). Variations in calcite growth kinetics with surface topography: molecular dynamics simulations and process-based growth kinetics modelling. *CrystEngComm*, *15*(27), 5506–5514.

Yu, H., & Van Gunsteren, W. F. (2004). Charge-on-spring polarizable water models revisited: From water clusters to liquid water to ice. *Journal of Chemical Physics*, *121*(19), 9549–9564.

Zhang, M., & Reardon, E. J. (2003). Removal of B, Cr, Mo, and Se from wastewater by incorporation into hydrocalumite and ettringite. *Environmental Science and Technology*, *37*(13), 2947–2952.

Zhang, L., Nasika, C., Donzé, F. V., Zheng, X., Renard, F., & Scholtès, L. (2019). Modeling Porosity Evolution Throughout Reaction-Induced Fracturing in Rocks With Implications for Serpentinization. *Journal of Geophysical Research: Solid Earth*, *124*(6), 5708–5733.

Zheng, X., Cordonnier, B., Zhu, W., Renard, F., & Jamtveit, B. (2018). Effects of Confinement on Reaction-Induced Fracturing During Hydration of Periclase. *Geochemistry, Geophysics, Geosystems*, *19*(8), 2661–2672.

Zheng, X., Cordonnier, B., McBeck, J., Boller, E., Jamtveit, B., Zhu, W., & Renard, F. (2019). Mixed-Mode Strain Localization Generated by Hydration Reaction at Crustal Conditions. *Journal of Geophysical Research: Solid Earth*, *124*(5), 4507–4522.

Papers

Paper I

Direct imaging of coupled dissolution-precipitation and growth processes on calcite exposed to chromium-rich fluids

Marthe Grønlie Guren, Christine Putnis, German Montes-Hernandez, Helen King, François Renard

Published in *Chemical Geology*

I

Chemical Geology 552 (2020) 119770

Contents lists available at ScienceDirect

Chemical Geology

journal homepage: www.elsevier.com/locate/chemgeo

Direct imaging of coupled dissolution-precipitation and growth processes on calcite exposed to chromium-rich fluids

Marthe G. Guren[a,*], Christine V. Putnis[b,c], German Montes-Hernandez[d], Helen E. King[e], François Renard[a,d]

[a] The Njord Centre, Departments of Geosciences and Physics, University of Oslo, Norway
[b] Institute für Mineralogie, University of Münster, 48149 Münster, Germany
[c] School of Molecular and Life Science, Department of Chemistry, Curtin University, Perth 6845, Australia
[d] Université Grenoble Alpes, Univ. Savoie Mont Blanc, CNRS, IRD, IFSTTAR, ISTerre, 38000 Grenoble, France
[e] Department of Earth Sciences, Utrecht University, Princetonlaan 8a, 3584CB Utrecht, the Netherlands

ARTICLE INFO

Editor: Karen Johannesson

Keywords:
Hexavalent chromium
Calcite
Coupled dissolution-precipitation
Crystal growth
Atomic force microscopy
Flow-through reactor

ABSTRACT

Recent increases in industrial activity have resulted in elevated chromium (Cr) pollution in the natural environment, from the degradation of concrete and the leakage of water from landfills or mine waste. The release of toxic chromate ions into the environment could have harmful consequences. Methods for Cr removal are therefore becoming increasingly important to control the release of this highly toxic metal into the environment. This study examines how chromate (CrO_4^{2-}) can be incorporated into a new, stable solid phase at a dissolving calcite surface. To study the relationship between solutions containing chromate and calcite, we performed two series of time-lapse atomic force microscopy (AFM) experiments to identify calcite dissolution and growth rates in the presence of chromate. In addition, we conducted complementary experiments in a stirred flow-through reactor to determine the amount of Cr removal from solution. All experiments were performed at room temperature and under a constant initial pH in the range 6–12. During the AFM experiments, we observed calcite dissolution via etch pit formation and propagation. In the presence of chromate, nanoparticles of a new phase nucleated and grew at the calcite surface by a coupled dissolution-precipitation process. In experiments with concentrations above 10 ppm Cr or at pH 10 and higher, we observed many nanoparticle precipitates, while precipitates were rarely observed at lower concentrations of Cr. At pH 10.5, the precipitates covered the calcite surface. This partly passivated further calcite dissolution, an observation confirmed by the low amounts of Cr removal measured in the flow-through experiments. Scanning electron microscopy analysis demonstrated that Cr was associated with the precipitates, indicating that Cr could be captured from solution and trapped in solid nanoparticles in the presence of calcite. However, the passivation of the calcite surface by a new precipitate may eventually slow down Cr sequestration.

1. Introduction

Chromium (Cr) is one of the most toxic metals. In natural environments Cr is found in two stable oxidation states, $Cr^{(III)}$ and $Cr^{(VI)}$, where $Cr^{(VI)}$ is more soluble, has a high mobility and is toxic to animals and plants (e.g. Bartlett and James, 1979; Rakhunde et al., 2012). Thus, if the redox conditions change in the environment, the Cr oxidation state can change, altering the toxicity level. As such, the contaminant level for drinking water is dictated by the total amount of Cr. US Environmental Protection Agency (EPA) regulations stipulate that a maximum of 100 ppb Cr can be present in drinking water, whereas in European countries the limit is placed at 50 ppb by the European Food Safety Authority (EFSA, 2014; Hua et al., 2007; Moraetis et al., 2012).

Natural Cr occurrence varies depending on rock types. For example, carbonate rocks and sandstones account for low Cr concentrations (10–19 ppb) in groundwater, while the reaction of ultramafic and igneous rocks results in higher Cr concentrations (32 ppb) (Fantoni et al., 2002). Anthropogenic Cr pollution is a significant problem that has been accelerated due to increased mining and the widespread use of Cr in industrial activities due to its resistance to corrosion. Thus, the use of Cr and its mobilization behavior has attracted much interest in technique development aimed at controlling its leachability and/or its removal from wastewaters (Zhang and Reardon, 2003; Cornelis et al., 2008; Sánchez-Pastor et al., 2010; Hajji et al., 2019).

* Corresponding author.
E-mail address: m.g.guren@geo.uio.no (M.G. Guren).

https://doi.org/10.1016/j.chemgeo.2020.119770
Received 5 September 2019; Received in revised form 15 June 2020; Accepted 24 June 2020
Available online 27 June 2020

Recent studies have shown that Cr can be effectively incorporated into minerals as a method of removing it from aqueous solution. Hajji et al. (2019) used a stirred flow-through reactor to study the adsorption/sequestration of Cr and As in three different iron minerals; ferrihydrite, goethite and siderite. Their results indicated that siderite was the most effective at removing $Cr^{(VI)}$ from water, followed by ferrihydrite and goethite. Ca-bearing mineral reactants have also shown promise for removing Cr from solution. For instance, Zhang and Reardon (2003) used hydrocalumite ($Ca_2Al_2(OH)_{12}(OH)_2{\cdot}6H_2O$) and ettringite ($Ca_6Al_2(OH)_{12}(SO_4)_3{\cdot}26H_2O$) to extract B, Cr, Mo and Se from wastewater. They found that both hydrocalumite and ettringite effectively trapped Cr, where hydrocalumite was the most effective as it could reduce the Cr concentration in solution to below US drinking water standards (Zhang and Reardon, 2003).

The more toxic form of Cr in groundwater, $Cr^{(VI)}$, forms the oxyanion chromate (CrO_4^{2-}) in aqueous solution. This form has the potential to be incorporated into other oxyanion-bearing minerals, such as calcite ($CaCO_3$) as demonstrated by Hua et al. (2007) and Tang et al. (2007). Coprecipitation experiments by Hua et al. (2007) showed that chromate becomes immobilized through incorporation into the calcite structure when introduced to a calcite synthesis solution. In addition, analysis of Cr distribution using μ-X-ray fluorescence demonstrated that $Cr^{(VI)}$ phases have a preferred precipitation position along the obtuse angle on the calcite surface and that the amount of $Cr^{(VI)}$ in calcite increases with increasing $Cr^{(VI)}$ concentration in the solution. In contrast, if chromate was added after the calcite formation, the oxyanion was removed from the solution but could be released again when the calcite was exposed to acidic solutions (Hua et al., 2007).

In recent years, nanoscale imaging studies have shown that coupled carbonate dissolution and precipitation of nanoparticles occurs easily at mineral surfaces (e.g. Ruiz-Agudo et al., 2014). These nanoparticulate phases can trap various oxyanion pollutants including Se, As and Sb (e.g. Putnis et al., 2013; Renard et al., 2013, 2015, 2018). This coupled dissolution-precipitation occurs in the boundary layer at the mineral-water interface (Putnis and Putnis, 2007; Ruiz-Agudo et al., 2014; Renard et al., 2019). Therefore, although Hua et al. (2007) predict that exposure of calcite to chromate-bearing solutions results in chromate uptake via adsorption, uptake levels could equally be explained via the formation of a new phase that is below the detection limit of X-ray diffraction. The longevity of chromate uptake would be different in the two scenarios as nanoparticles have the potential to transform to more stable phases, whereas adsorption would constitute a more labile chromate pool. The aim of the present study is thus to directly observe and quantify the interaction between calcite and Cr-rich solutions and evaluate how $Cr^{(VI)}$ interacts with calcite by either a coupled dissolution-precipitation mechanism, adsorption or by Cr-substituted calcite growth.

To study the interactions between calcite and Cr-rich solutions, pH values and $Cr^{(VI)}$ concentrations were selected to represent natural systems. The amount of Cr in different systems varies from 10 to 19 ppb in carbonate rocks and sandstone (Fantoni et al., 2002) and up to 60 ppm in pore water in soils (Robertson, 1975). The presence of $Cr^{(VI)}$ in various geological and industrial systems (e.g. Robertson, 1975; Deakin et al., 2001; Cornelis et al., 2008; Fantoni et al., 2002; Moraetis et al., 2012), occurs with a wide range of alkalinity. In ground water and soils, with the presence of Cr, the pH is in the range 7.45–8.1 (Moraetis et al., 2012), while in ophiolitic rocks, serpentine and limestones, the pH varies in the range 7–10.5 (Fantoni et al., 2002; Moraetis et al., 2012). In leachates from cement systems, alkaline solid waste and smelter waste from chromate ore processing, the pH is in the range 10–13 (Deakin et al., 2001; Cornelis et al., 2008). In particular, Deakin et al. (2001) found that fluid leachate containing Ca^{2+}-cations and CrO_4^{2-}-anions were hyperalkaline with pH between 10.3 and 11. We have built on these findings, and adapted to our experimental design, e.g. a certain amount of Cr is necessary to observe reactions within experimental time. The tested solutions thus have $Cr^{(VI)}$ concentrations in the range 10–150 ppm and pH in the range 6–12.

2. Methods

2.1. Atomic force microscopy (AFM) experiments

We performed two series of AFM experiments, labelled CaCrD and CaCrG, where *Ca* and *Cr* stand for Calcium and Chromium, respectively. The *D* refers to the coupled dissolution-precipitation experiments and the *G* refers to the growth experiments.

2.1.1. Calcite and solutions

A calcite crystal (Iceland spar, Vizcaya, Mexico) was obtained from the Natural History Museum in London. Inductively Coupled Plasma-Optical Emission Spectroscopy (ICP-OES) analyses indicated the high purity of the calcite crystal, with only trace amounts of Mn (31 ppb), Mg (2.8 ppb), and Sr (11.4 ppb). Freshly cleaved rhombohedral fragments (~3 × 3 × 1 mm) were cleaved directly before each experiment from a single calcite crystal by putting pressure on a knife blade along one of the cleavage planes.

2.1.1.1. Coupled dissolution-precipitation experiments. As well as deionized water, solutions containing $Cr^{(VI)}$ oxyanions were used and tested in a range of pH values 6–12. First, double-deionized water (resistivity ≥18.2 MΩ·cm^{-1}) was injected in the flow-through fluid cell of the AFM (Fig. S1a) to initiate dissolution at the calcite surface. Then, solutions with $Cr^{(VI)}$ oxyanions were injected in the fluid cell with increasing concentrations of $Cr^{(VI)}$ but with the same pH. These solutions were prepared by diluting a stock solution with a concentration of 0.5 M $Cr^{(VI)}$ and 5 M NaCl to obtain solutions with concentrations of 1, 10, 50 and 100 ppm $Cr^{(VI)}$. Na_2CrO_4 salt was used as the $Cr^{(VI)}$ source. NaOH and NaCl were used to adjust the pH and ionic strength (0.05 M) of the solutions.

2.1.1.2. Calcite growth experiments. Three different aqueous solutions were used; deionized water and growth solutions with and without $Cr^{(VI)}$. The growth solutions contained $CaCl_2$ and $NaHCO_3$ and the amounts were adjusted based on thermodynamic calculations using the PHREEQC software (version 3, Parkhurst and Appelo, 2013) such that the solutions were supersaturated with respect to calcite, with log Ω in the range 0.7 to 1.7. For the growth experiments, we started the experiments by injecting deionized water to dissolve the calcite surface. Then we injected the growth solution without $Cr^{(VI)}$ oxyanions before we injected the growth solutions with increasing $Cr^{(VI)}$ concentrations: 1, 10, 50 and 150 ppm $Cr^{(VI)}$. The pH was constant in each initial solution and was varied in the range 8–11 between experiments. The pH of the solutions was also measured independently using a pH meter.

2.1.2. Experimental procedure

The calcite surfaces were imaged with nanometer height resolution and micrometer spatial resolution at room temperature (21 ± 2 °C) by using a Bruker Multimode Atomic Force Microscope (AFM) with a scan rate of 4 Hz and Si_3N_4 tips (Bruker, tip model NP-S20) with spring constants 0.12 N/m and 0.58 N/m. The fluid cell was sealed with an O-ring, giving a fluid cell with a volume of 50 μL. The volume of the fluid in the cell was reduced to approximately 35 μL after subtracting the volume occupied by the calcite crystal. For all the experiments, the same procedure was followed to ensure that the results would be comparable. The first image of the surface was taken in air before any fluid had been introduced. All the AFM images were sequentially acquired by scanning in the downward direction. Subsequently the aqueous solutions were manually injected after each scan, giving regular time intervals of ~70 s (scan time) and a constant volume of 2 mL using a syringe, giving an effective flow rate of ~30 μL/s. The calcite crystal was first exposed to deionized water that was injected for 20–30 min to initiate dissolution and to observe the reactivity of the surface. Then,

the solutions with $Cr^{(VI)}$ were injected with increasing $Cr^{(VI)}$ concentration.

2.1.2.1. Imaging procedure. For the dissolution experiments, we started with the lowest concentration of $Cr^{(VI)}$ and acquired at least ten scans with 2 mL of fluid injection between each scan. Then, the AFM tip was lifted up for 10 min, to leave enough time for nanoparticle precipitates to grow in experiments where they formed and to avoid the influence of the scanning tip, followed by two scans without any fluid injection before continuing the same procedure with the next solution with higher $Cr^{(VI)}$ concentration. After injecting the last solution, and waiting for 10 min, a few extra scans were acquired from different areas on the calcite surface to confirm that the observations in one area of the calcite surface were representative of the entire surface.

For the growth experiments, we acquired eight scans with 2 mL of fluid injection between each scan. In contrast to the dissolution experiment, we did not lift the tip up for 10 min between each solution, but injected the next fluid directly after the previous one. As for the dissolution experiments, we scanned in several areas on the surface after the last injection.

The samples were studied in the AFM for 2–3 h before they were removed from the fluid cell. Eight of the dissolution samples (Table 1) and five of the growth samples (Table 2) were left in contact with their last solution between 12 and 118 h before we imaged them again in the AFM to search for precipitate development.

Table 1
List of the atomic force microscopy dissolution experiments in the presence of $Cr^{(VI)}$ and formation of precipitates. All the experiments were performed at room temperature and with a constant ionic strength of 0.05 M. Two sets of experiments were performed under the same conditions for each concentration to check reproducibility. The duration that the calcite was left in solution after the experiment is indicated.

Experiment	$[Cr^{(VI)}]$	pH	Precipitates	Hours in solution after	SEM	Raman band centers (cm^{-1})
CaCrD01	1	6.7	None	24	Yes	
	10	7.7	None			
	50	7.7	A few			
	100	8.0	A few			
CaCrD02	1	11.9	A lot	24	Yes	
	10	12.0	A lot			
	50	12.0	A few			
	100	12.0	A lot			
CaCrD03	1	10.8	A few	24	Yes	362
	10	10.5	Passivation of the surface			605 818
CaCrD04	50	10.5	A few	0	No	
	100	10.4	A few			
CaCrD06	1	8.2	None	24	Yes	
	10	8.5	None			
	50	8.8	A few			
	100	8.9	None			
CaCrD07 (Same as CaCrD06)	1	8.2	None	24	Yes	
	10	8.5	None			
	50	8.8	A few			
	100	8.9	None			
CaCrD08	1	6.2	None	24	Yes	
	10	6.3	A few			
	50	6.5	None			
	100	6.3	A few			
CaCrD09 (Same as CaCrD03)	1	10.8	A few	0	No	
	10	10.5	Passivation of the surface			
CaCrD10	1	9.4	A few	52	Yes	
	10	8.1	A lot			
	50	9.5	A lot			
CaCrD12	1	10.4	A few	88	Yes	
	10	10.6	A lot			
	50	10.5	A lot			

Table 2
List of the atomic force microscopy calcite growth experiments in the presence of $Cr^{(VI)}$. All the experiments were performed at room temperature. Two sets of experiments were performed under the same conditions to check reproducibility. $[Cr^{(VI)}] = 0$: Growth solution without $Cr^{(VI)}$. The time that the calcite was left in solution after the AFM experiment is indicated. Saturation index of the solution with respect to calcite if given (log Ω, where $\Omega = [Ca^{2+}][CO_3^{2-}] / Calcite\ K_{sp}$).

Experiment	$[Cr^{(VI)}]$	pH	log Ω	Hours in solution after	SEM
CaCrG01	0	9	0.74	0	No
	1	9			
	10	9			
	50	9			
	150	9			
CaCrG02	0	11.2	1.65	112	Yes
	1	11.2			
	10	11.2			
	50	11.2			
	150	11.2			
CaCrG03	0	11.2	1.65	109	Yes
	1	11.2			
	10	11.2			
	50	11.2			
	150	11.2			
CaCrG04	0	10.2	1.60	118	Yes
	1	10.2			
	10	10.1			
	50	10.0			
	150	9.9			
CaCrG05 (Same as CaCrG04)	0	10.2	1.60	0	No
	1	10.2			
	10	10.1			
	50	10.0			
	150	9.9			
CaCrG06 (Same as CaCrG04)	0	10.2	1.60	113	Yes
	1	10.2			
	10	10.1			
	50	10.0			
	150	9.9			
CaCrG07	0	9.0	1.68	19	Yes
	1	9.2			
	10	9.0			
	50	8.8			
	150	7.9			
CaCrG08 (Same as CaCrG07)	0	9.0	1.68	0	No
	1	9.2			
	10	9.0			
	50	8.8			
	150	7.9			
CaCrG09 (Same as CaCrG07)	0	9.0	1.68	0	No
	1	9.2			
	10	9.0			
	50	8.8			
	150	7.9			

2.1.2.2. Scanning electron microscopy. After the twelve samples were removed from their corresponding solutions and imaged in the AFM, they were coated with a thin layer of gold under the conditions of 20 mA for 80 s before the surface was imaged with a Hitachi SU5000 field-emission Scanning Electron Microscope (SEM). The chemical content of major elements was acquired using semi-quantitative energy-dispersive spectrometry (EDS) in the SEM.

2.1.2.3. Raman spectroscopy. Raman spectroscopic analysis was performed after the AFM experiments to provide additional identification information of the precipitated phase. A WITec Alpha 300R Raman spectrometer equipped with an optical microscope was used for this analysis, operated with a 785 nm line of a He−Ne laser, with a grating of 300 grooves/mm. A 50× long working distance optical lens (numerical aperture: 0.55) was used, providing a lateral resolution of approximately 2 μm at the sample surface and a depth resolution of approximately 3 μm. An integration time of five seconds

and ten accumulations was required to obtain a spectrum with a high enough signal to noise ratio to detect bands related to the precipitates on the calcite surface. During the analysis, no change in the material was observed either in the optical microscope image or spectrum. Background removal and peak fitting were performed using the WITec Project Plus software (version 4).

2.1.2.4. Water resistance. For two of the samples that had been exposed to solutions for a longer period, we tried to dissolve the newly-formed layer on top of the calcite surface to test the chemical resistance of the layer. To do so, 2 mL of deionized water was injected between every scan during the first 5–10 scans, then 5 scans were acquired without any injection, one injection and 5 scans again. The sample was in the fluid cell for ~80 min.

2.1.2.5. Image processing. All AFM images were processed using the NanoScope Analysis Software (Version 1.5). Etch pit spreading rates and growth rates were calculated from sequential images where the length increase of two opposite parallel steps were measured (Ruiz-Agudo and Putnis, 2012; Renard et al., 2019).

2.2. Stirred flow-through experiments

To study if $Cr^{(VI)}$ could be incorporated into calcite, we performed a series of experiments with a stirred flow-through reactor (Fig. S1b) using synthetic calcite, following the experimental procedure as described by e.g. Hajji et al. (2019) and Renard et al. (2017). These experiments complement the dissolution experiments in the AFM as we use a solution that is undersaturated with respect to calcite. The calcite was synthesized by aqueous carbonation of portlandite with compressed CO_2 (55 bar) at room temperature, following the reaction $Ca(OH)_2 + CO_2 = CaCO_3 + H_2O$. The mineral composition and/or purity was determined by X-ray diffraction analysis. Further details on the experimental procedure for synthetic nano-calcite and determination of textural properties are found in Montes-Hernandez et al. (2007) and Montes-Hernandez et al. (2008), respectively. The flow-through setup consisted of a beaker with the initial solution, a pump, and two stirred fluid-cell reactors with an internal volume of 50 mL. We performed five flow-through experiments with solutions containing concentrations of either 10 or 100 ppm $Cr^{(VI)}$ and pH between 10 and 12. This pH range was selected because here most precipitates were observed in the AFM experiments. K_2CrO_4 salt was used as $Cr^{(VI)}$ source. The experimental conditions are given in Table 3. For all the experiments, the pump had a constant flow rate of 2.1 mL/min. The reactors were placed on a plate that maintained a temperature of 20 °C and the magnetic stirrers had a constant rate of 750 rpm. In one of the reactors, we placed 1 g synthetic chemically pure calcite, while the other reactor did not contain any mineral. The fluid injected in the reactor without calcite was used as a passive tracer, to quantify if Cr is adsorbed on the walls of the reactor during percolation (Hajji et al., 2019). We ran 1.3 L of solution through the reactors and took samples of the output solution after 5, 15 and 30 min, followed by every 30 min until it had been running for 5 h. Each output sample contained 13 mL of solution and it took around 6 min to retrieve each sample. These samples were acidified by the addition of three drops of 2 N HNO_3. All solutions with 100 ppm $Cr^{(VI)}$ were diluted ten times before they were analyzed by Inductively Coupled Plasma Atomic Emission Spectroscopy (ICP-AES). After the experiments, the remaining particles were retrieved from the reactors. The excess water was poured out and the samples were allowed to dry at 60 °C for 12 h. The amount of $Cr^{(VI)}$ in the powder retrieved from the reactor was quantified by Inductively Coupled Plasma Mass Spectrometry (ICP-MS) analysis. To dissolve the powder for analysis, 50 mg of the material was measured and dissolved in 3 mL of 14 N HNO_3 for 2 h at 120 °C. The liquid was then evaporated at the same temperature and the residue was again re-dissolved in 3 mL 7 N HNO_3 and re-evaporated at 120 °C. The final residue was re-dissolved in 7 N HNO_3 before diluted in 2% HNO_3. These liquid samples were then analyzed by ICP-MS. The amount of $Cr^{(V)}$ in each sample was normalized by the surface area of calcite (9 m^2/mg).

Table 3
List of stirred flow-through experiments. All experiments were performed at 20 °C, with a constant stirring rotation of 750 rpm and constant flow rate of 2.1 mL/min. The initial Cr concentration is given. The Cr concentration of the calcite powder was measured after dissolution in nitric acid using ICP-MS. Results are given in ppm and divided by the surface area of calcite with 10% standard deviation.

Exp. no.	$[Cr^{(VI)}]$ ppm	pH	ICP-MS $Cr^{(VI)}$ ppm	ICP-MS $Cr^{(VI)}$ mg/m^2
1	10	10	5.6	$6.2{\cdot}10^{-4}$
2	100	10	11	$1.2{\cdot}10^{-3}$
3	100	12	7.1	$7.9{\cdot}10^{-4}$
4	10	12	7.0	$7.8{\cdot}10^{-4}$
5	100	12	13	$1.4{\cdot}10^{-3}$

3. Results

3.1. Dissolution of the calcite surface in the presence of $Cr^{(VI)}$ and precipitation of nanoparticles

During the first 10–20 AFM scans (i.e. 15 to 30 min), the calcite surface was slowly dissolved when exposed to deionized water. The dissolution of the surface was characterized by the formation and growth of rhombohedral etch pits that progressively increased in size as the surface continuously dissolved. Within two scans (~3 min) after injection of the first solution containing $Cr^{(VI)}$, the shape of the etch pits changed to show a rounding of the obtuse corners. The surface then continued dissolving via etch pit propagation with the altered shape.

The dissolution rate at the calcite surface was calculated by measuring the length increase of two opposite etch pit sides between two sequential images (Ruiz-Agudo and Putnis, 2012). The dissolution rate of the etch pits, V, was calculated using:

$$V = \frac{(l_x + l_y)_{i+1} - (l_x + l_y)_i}{2 * \Delta t} \quad (1)$$

where l_x and l_y are the lengths of the etch pit sides, i is image number and Δt is the time difference between two sequential images.

The dissolution rate is dependent on $Cr^{(VI)}$ concentration and pH as shown in Fig. 1. The rate is almost constant for all the experiments with deionized water, and ranges between 0.8 ± 0.3 and 1.8 ± 0.9 nm/s, in agreement with previous studies (Ruiz-Agudo et al., 2010). A constant or slight decrease in the dissolution rate from 2.3 ± 0.6 nm/s to 1.6 ± 0.9 nm/s is observed when the $Cr^{(VI)}$ concentration is increased from 1 to 10 ppm. This slight decrease could be an effect of change in $Cr^{(VI)}$ concentration, but the dissolution rate variations are within the error bars and are therefore within experimental uncertainty. However, above 10 ppm $Cr^{(VI)}$, the dissolution rate increases with increasing $Cr^{(VI)}$ concentration from 1.6 ± 0.9 nm/s to 3.2 ± 0.7 nm/s. There is also a small correlation between etch pit dissolution rate and pH. At higher pH values, the etch pit dissolution rate is slower than at lower pH values. The measured values for Cr-rich solutions, independent of pH, varies between 1.2 and 4.3 nm/s.

In the presence of a Cr-rich solution, the formation of precipitates is observed in situ, during the dissolution of the calcite surface and within minutes of initial scanning. At high pH, rounded precipitates are observed after injecting 1 ppm $Cr^{(VI)}$ into the fluid-cell, while at lower pH values, a higher concentration of $Cr^{(VI)}$ is required to observe these precipitates (Fig. 2a). The number of precipitates is highest at high concentrations of $Cr^{(VI)}$ and/or high pH values (Fig. 2a).

During the experiments, most of the scans were acquired over a surface area of 5 × 5 μm^2. Scans over a surface area of 7 × 7 μm^2 were

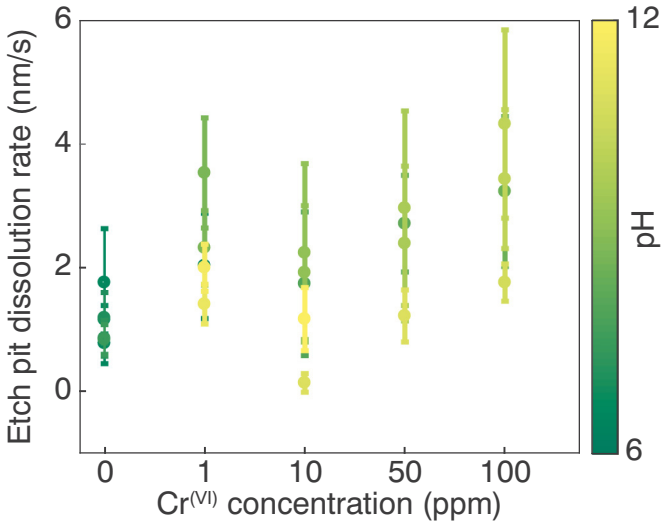

Fig. 1. Etch pit dissolution rate as a function of $Cr^{(VI)}$ concentration. Color code indicates the pH of the experiment. [$Cr^{(VI)}$] = 0: Deionized water. (For interpretation of the references to color in this figure legend, the reader is referred to the web version of this article.)

acquired to see if the tip had removed precipitates out of our initial 5 × 5 μm^2 view area. Occasionally, we observed that the precipitates had been removed out of the 5 × 5 μm^2 scan-window, probably by the scanning tip, which indicates that the precipitates were initially weakly attached to the surface.

In the scans where the precipitates were not removed by the tip, the nanoparticle precipitates are evenly distributed over the surface, except in experiment CaCrD03, where a preferred location for growth of precipitates near the edges of large etch pits is observed, similar to previous observations by Renard et al. (2018) on the calcite-antimony system. A preferred location during incorporation of Cr into the calcite structure has been reported by the experiments from Tang et al. (2007), where Cr was found mainly along the obtuse angles.

The nanoparticle diameters and heights were measured in images obtained during dissolution experiments and collected at different times and with different experimental conditions (Fig. 2b). Particle diameters have an average size of 111 ± 29 nm and height of 3 ± 2 nm, giving a very low height to diameter aspect ratio. Such low height to diameter aspect ratio was observed in other studies (e.g. Renard et al., 2017) and indicates the formation of a thin nanolayer with wider surface area, formed by the merging or coalescence of adjacent nanoparticles. This process was observed in situ in the AFM. For the samples exposed to their corresponding solution for 24 h after the AFM imaging, larger precipitates are observed with an average diameter of 1.6 μm and

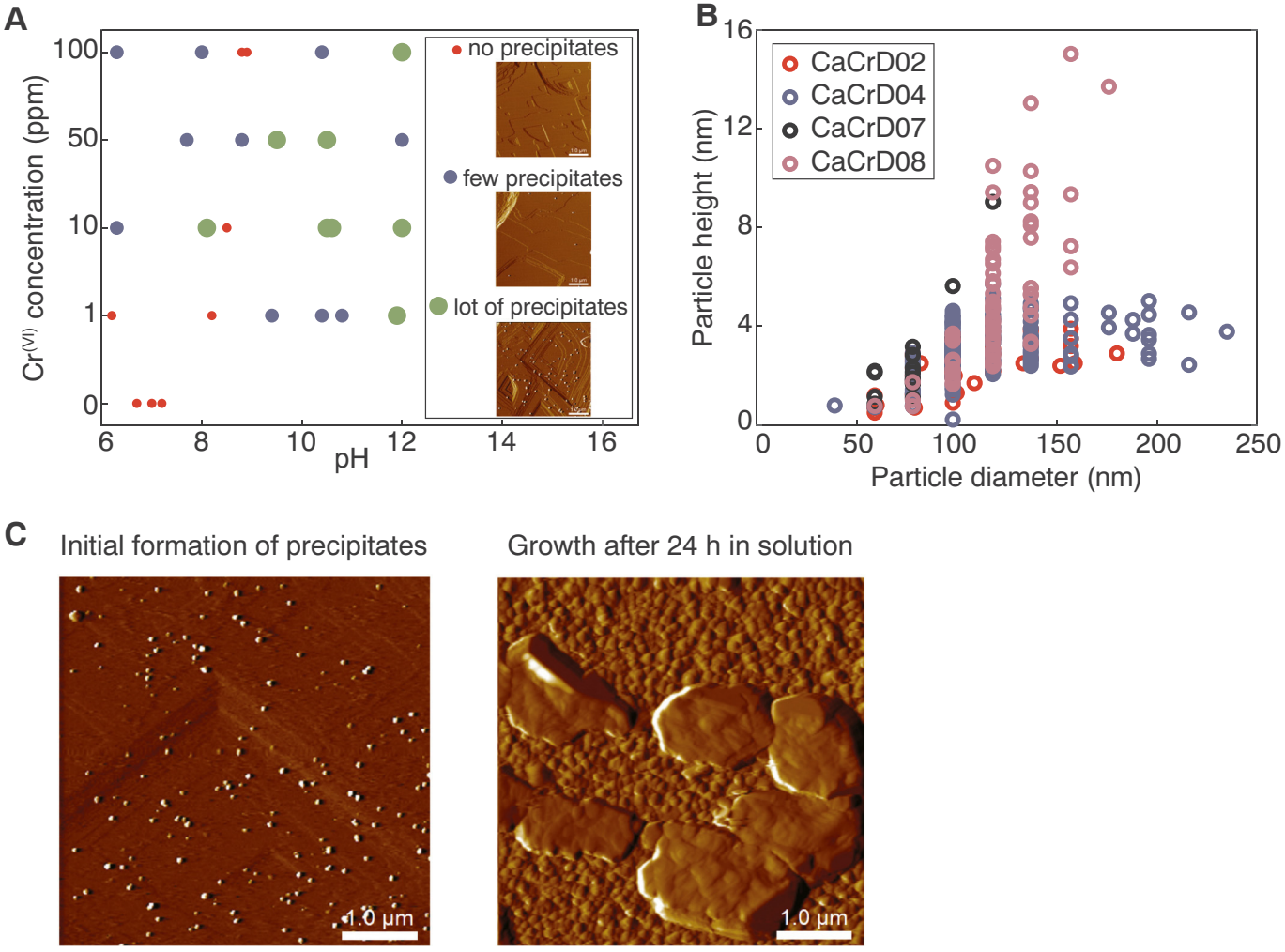

Fig. 2. A) Amount of precipitates on a calcite surface in the presence of $Cr^{(VI)}$-rich solutions with different $Cr^{(VI)}$ concentrations and pH. B) Analysis of the shape of the precipitated particles on the calcite surface given by particle height vs particle diameter (nm). C) Formation and growth of precipitates on calcite in Cr-rich solution (AFM deflection image of sample CaCrD01). Left: Nanoparticles formed during the experiment under the AFM. Right: Nanoparticles imaged after the sample was left 24 h in solution.

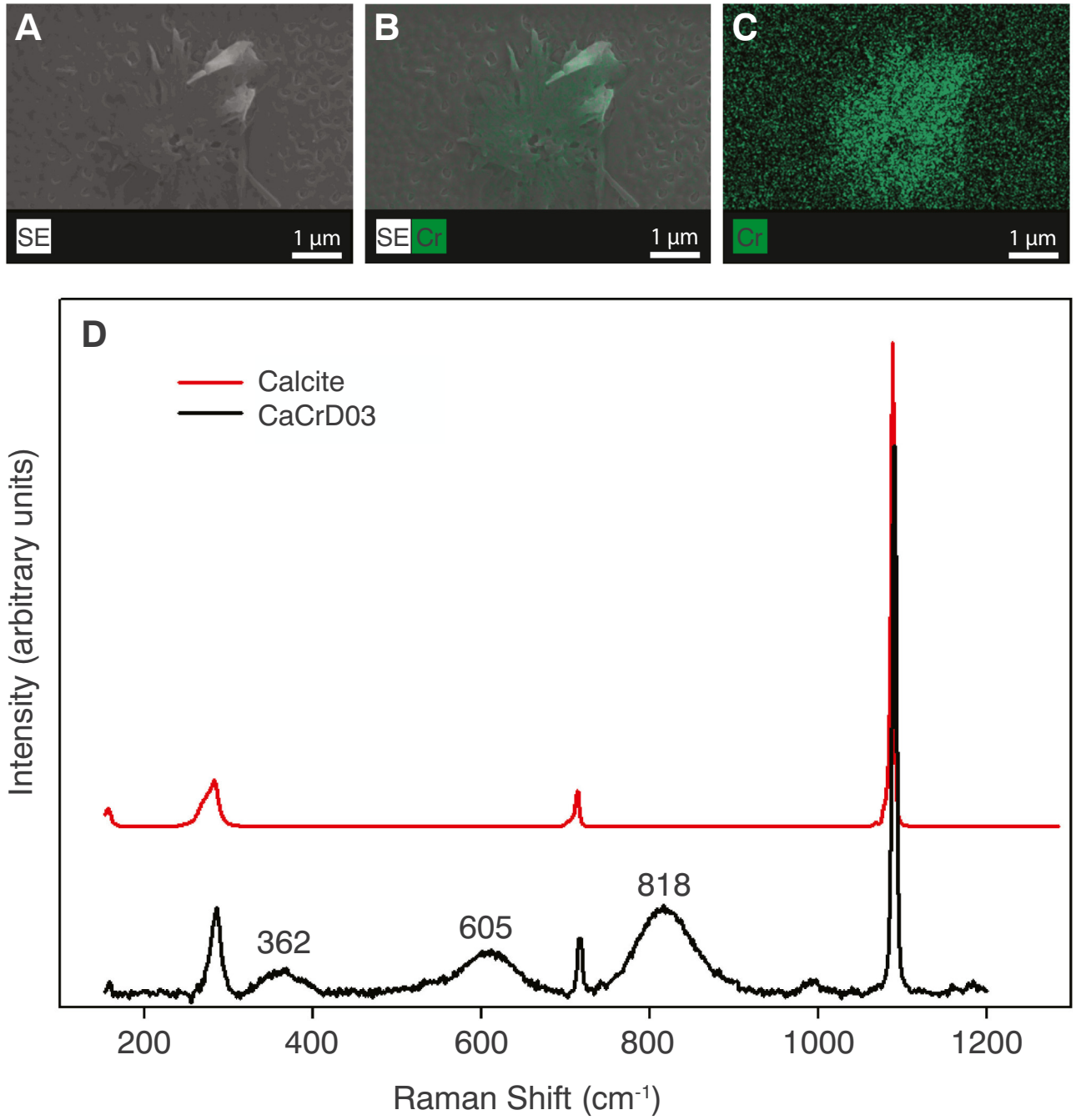

Fig. 3. Identification of the precipitates. A–C) SEM and EDS mapping of chromium (Cr). D) Raman spectra of a reference calcite and of nanoparticles from sample CaCrD03, with positions of the main Raman peaks indicated.

heights up to 320 nm (Fig. 2c). These appear to be formed via merging of smaller particles. When studying the surface in the AFM we observe that 30% of the experiments contained a lot of precipitates (e.g. sample CaCrD02) while 20% of the experiments did not contain any precipitates (e.g. sample CaCrD06).

The Raman bands associated with the precipitates indicate that they have a different composition than the background material (calcite). The precipitates consistently produce three bands at 362, 605 and 818 cm^{-1} (Table 1) where the most intense band is found at 818 cm^{-1} (Fig. 3d), a characteristic band associated with chromate-bearing minerals (Kiefer and Bernstein, 1972; Sánchez-Pastor et al., 2010). The indication of a chromate-bearing mineral is consistent with the detection of Cr in the particles using EDS (Fig. 3a-c).

3.2. Calcite growth in the presence of $Cr^{(VI)}$

For the experiments with growth solutions, the calcite surface was initially exposed to deionized water before the growth solution was injected. Etch pits formed in the presence of deionized water. However, as soon as the growth solution was injected the surface changed with islands and pyramidal hillocks (growth spirals) forming across the whole surface as well as closure of the initial etch pits. These features characterize classical calcite growth (Ruiz-Agudo and Putnis, 2012). To measure the growth rate and how it changed with pH and $Cr^{(VI)}$-concentration, the width of islands and/or pyramid hillocks was measured between two sequential images and calculated using Eq. (1). Fig. 4a displays how the growth rate changes with pH and $Cr^{(VI)}$-concentration. Results show that the growth rate depends more on pH than on $Cr^{(VI)}$-

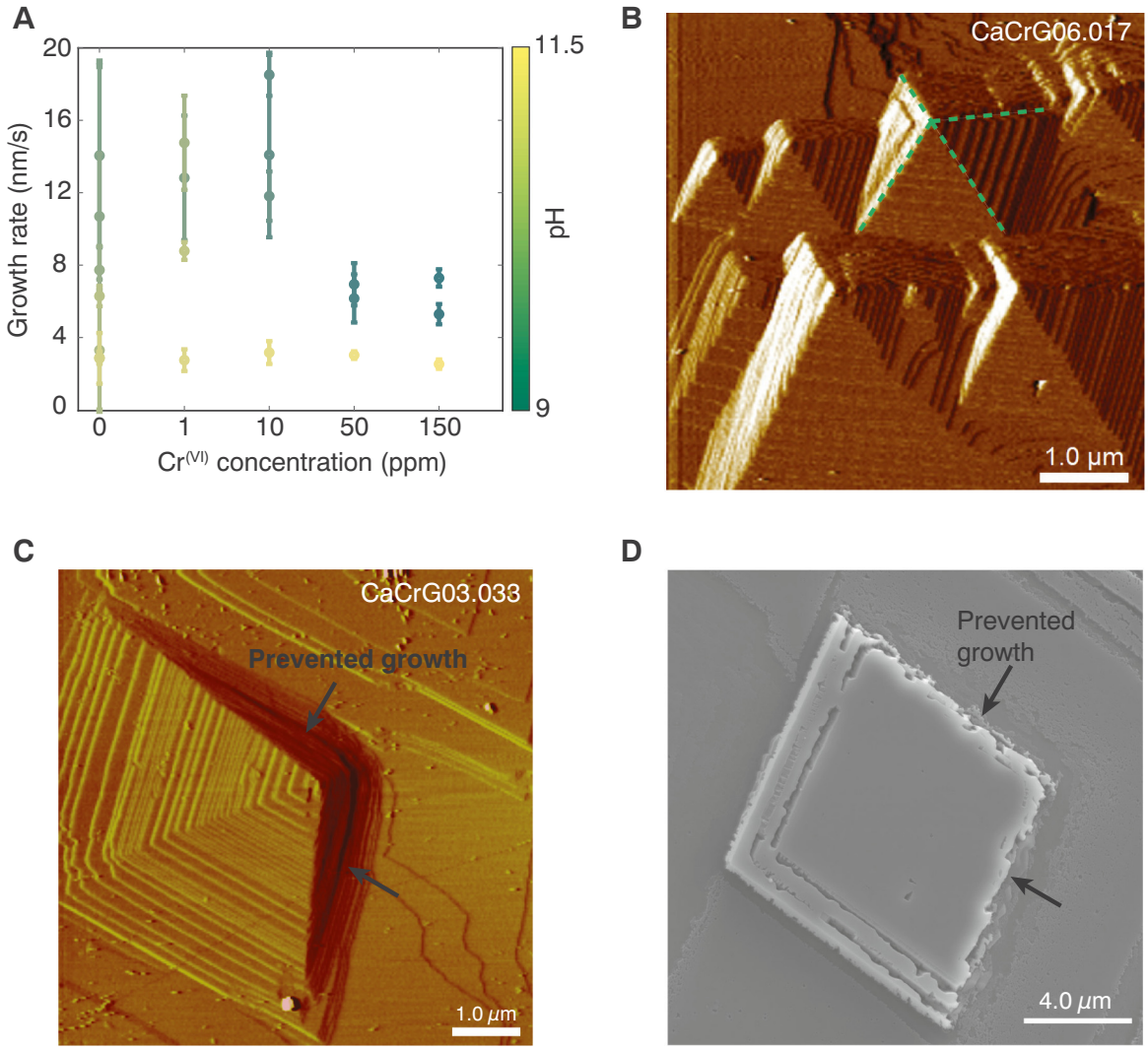

Fig. 4. A) Growth rate as a function of $Cr^{(VI)}$ concentration. Color code indicates the pH of the experiment. [$Cr^{(VI)}$] = 0: Growth solution. B) AFM deflection image (CaCrG06) showing spiral growth without any influence of Cr. The green dotted lines show the four straight sides of the pyramidal hillock. C) AFM deflection image (CaCrG03) showing inhibited step propagation on two sides of a spiral growth hillock when exposed to a Cr-rich solution. D) SEM image (CaCrG07) showing a growth island with two rough sides interpreted as related to prevented growth. (For interpretation of the references to color in this figure legend, the reader is referred to the web version of this article.)

concentration.

For the Cr-free growth solution, the growth rate decreased with increasing pH from 14.1 ± 5.1 nm/s at pH 9 to 2.9 ± 1.4 nm/s at pH 11.2. For the $Cr^{(VI)}$-rich growth solutions at pH 11.2, the growth rate was between 2.8 ± 0.6 to 3.2 ± 0.6 nm/s. At lower pH values (9–10.2), the growth rate varied more and the highest growth rate was 18.5 ± 1.2 nm/s at pH 10.2 and lowest growth rate at 5.3 ± 0.6 nm/s at pH 9.9. The experiments with solutions with pH 11.2 had a supersaturation of log Ω = 0.7 with respect to calcite while the experiments with pH 9–10.5 had a higher supersaturation with log Ω = 1.7. This difference in supersaturation would most likely impact the growth rate, but it is uncertain whether it is the pH, the supersaturation or a combination of both that causes the growth rate for the experiments at pH 11.2 to be significantly slower, however it has been shown that calcite growth decreases with increasing pH above ~9 (Ruiz-agudo et al., 2011) and both supersaturation and increasing OH^- concentration probably play a role.

During spiral growth, we observed that the obtuse corners of the pyramids were prevented from normal growth (Fig. 4c) and that corner became rougher and more curved. This corner also seemed to be pinned and grew at a slower rate. This feature appeared after the growth solution with $Cr^{(VI)}$ was introduced, indicating that the $Cr^{(VI)}$ had an effect on the growth mechanism. The samples were later studied in the SEM, and a similar feature was observed where two sides of a growth island showed rougher step edges (Fig. 4d).

3.3. Passivation of the calcite surface and resistance of the newly formed layer

Precipitates were observed to eventually completely cover the calcite surface in the coupled dissolution-precipitation experiments at pH 10.5 and 10 ppm $Cr^{(VI)}$ (CaCrD03). Fig. 4a and Supplementary Movie S1 show how these precipitates grew in diameter and, within 30 min, covered the whole surface. Even though it had been exposed continuously to a $Cr^{(VI)}$-rich solution, the surface topography was almost identical between the initial and precipitate covered surface (Fig. 5a, images taken with 18.5 min time interval). After the formation of the new surface layer, deionized water was injected into the fluid cell for around 40 min, without any observable change to the surface features indicating that a stable phase had formed and no continued dissolution of the underlying calcite occurred.

The same passivation process was observed in the growth

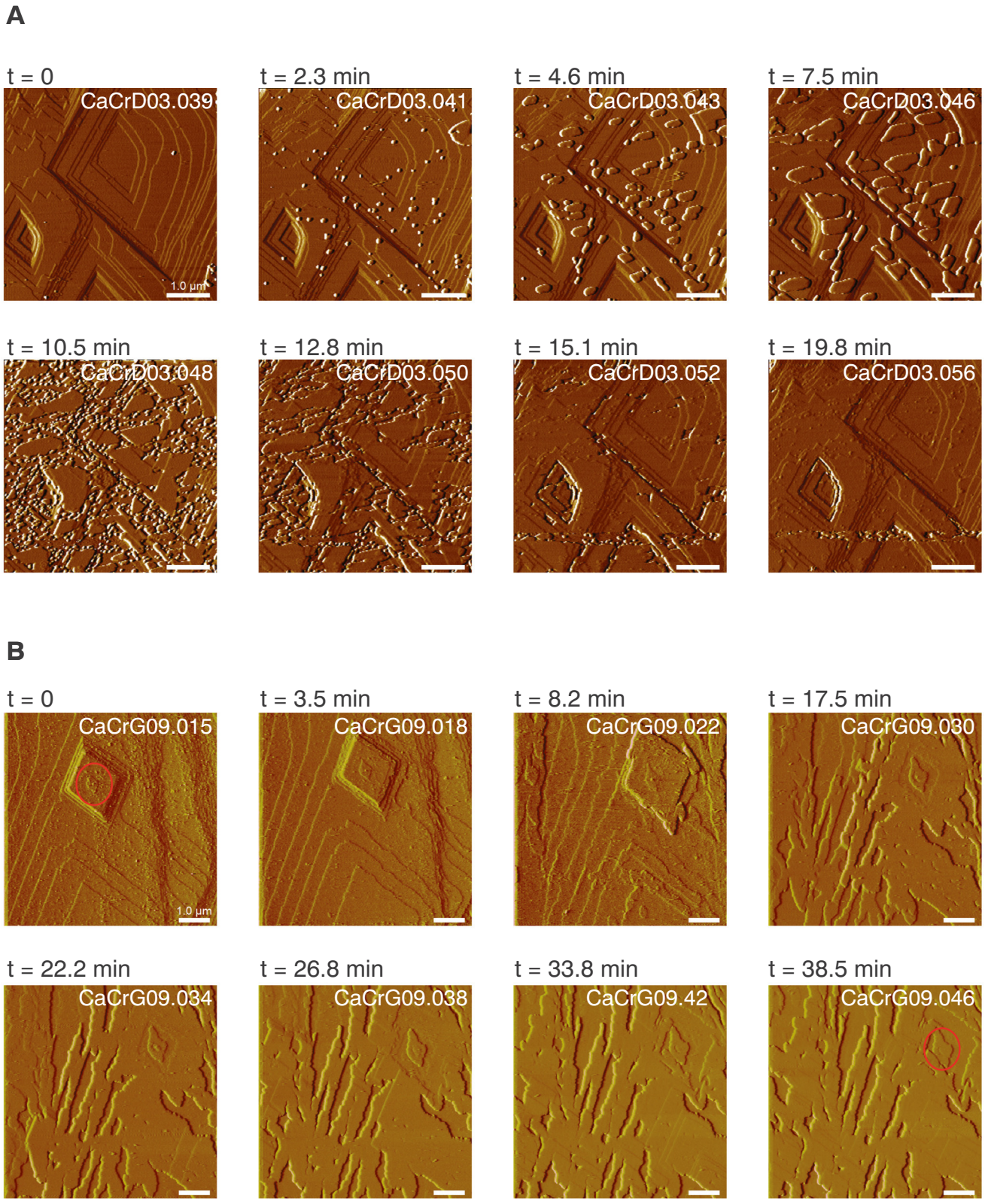

Fig. 5. Time-lapse AFM images of the passivation of the surface in a dissolution experiment (A) and a growth experiment (B). A) Formation of precipitates (CaCrD03) in a dissolution experiment. The particle shape evolves from round to elongated and eventually the precipitates cover the whole surface. Limited reactivity of the surface after layer formation is observed by comparing image with a 19.8 min time interval, that show the same features. All the scans of this experiment are displayed in the Supplementary material (Movie S1). B) Growth of a new layer, which slowly covers the whole surface in a growth experiment (CaCrG09). The red circle indicates a surface structure (image at time 0 and 38.5 min) that is still visible after 38.5 min of injection of $Cr^{(VI)}$-rich fluids. (For interpretation of the references to color in this figure legend, the reader is referred to the web version of this article.)

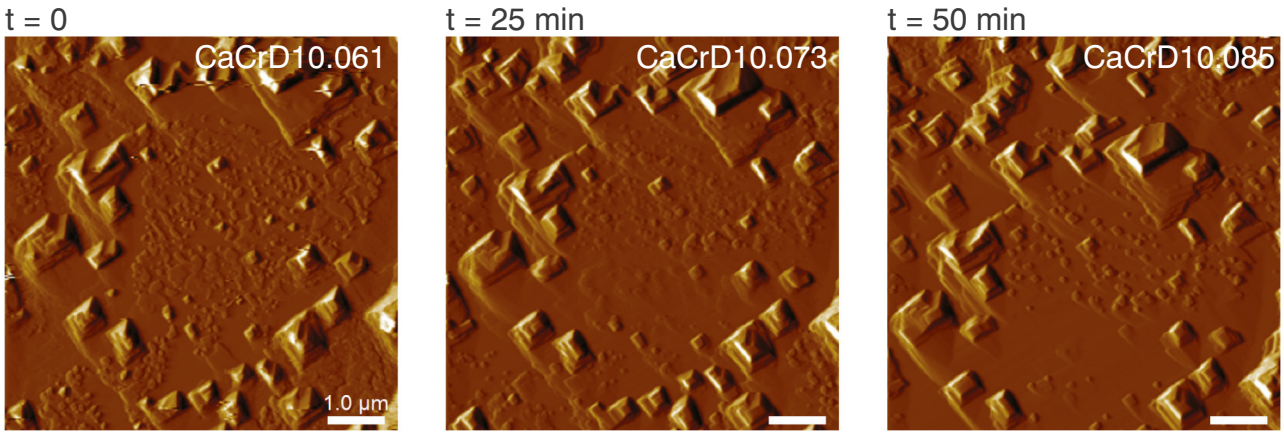

Fig. 6. Testing the solubility of the newly formed material. The images demonstrate minimal changes in surface topography on sample CaCrD10 despite being exposed to repeated injections of deionized water over 50 min.

experiments at pH 7.9–9.2 and 0–150 ppm $Cr^{(VI)}$ (CaCrG09) under the AFM. A layer was observed growing over the calcite surface (Fig. 5b) after injecting a solution with 1 ppm $Cr^{(VI)}$ at pH 9.2. Unlike the passivation in the dissolution experiments, in the growth experiments, islands still grew underneath the newly formed layer (Fig. S2) indicating that in some areas, an open space between the new layer and the calcite surface or possibly porosity within the precipitated layer allowed continuous access of the fluid and hence continued reaction.

The samples CaCrD10 and CaCrG04, that had been left in solution for 52 and 118 h, respectively, were exposed to deionized water for approximately 80 min to measure how the newly formed layer on top of the calcite surface would dissolve (Fig. 6). This layer was quite resistant to water. The formation of etch pits underneath the layer was observed, indicating that the calcite was dissolving faster than the newly-formed layer on top. Since the calcite could dissolve underneath the layer, it indicates that the layer was not completely covering the surface and that it possibly had some cavities or pores where the water accumulated and dissolved the calcite. After approx. 50 min of etch pit dissolution, the layer detached from the surface indicating that the layer was no longer attached to the underlying dissolving calcite at this point.

3.4. Flow-through experiments and adsorption of $Cr^{(VI)}$

The ICP-AES analyses of the output solutions from the stirred flow-through reactor experiments are given Fig. 7. For all of the experiments, we calculated a theoretical behavior of an inert tracer. The so-called breakthrough curve of such a tracer follows Eq. (2) (Limousin et al., 2007; Hajji et al., 2019),

$$C(t) = C_0\left[1 - \exp\left(-\frac{Q}{V_0}\cdot(t - t_0)\right)\right] \quad (2)$$

where the concentration C varies between 0 and C_0, and t_0 is the time when the tracer ($Cr^{(VI)}$ solution) is injected, Q is the flow rate (mL/min) and V_0 is the internal volume of the reactor.

In addition to the theoretical tracer, we measured the passive tracer concentration in two experiments, one with 10 and 100 ppm $Cr^{(VI)}$, such that we could validate the model of Eq. 2. Fig. 7a and c display the data of both a measured tracer and a theoretical tracer and show that there is good agreement between the two tracers, validating the Eq. 2 for our experiments. Figs. 7a-e indicate that there is no adsorption of $Cr^{(VI)}$ on the synthetic calcite. Fig. 7f shows how the released Ca^{2+} concentration changes with time for all the experiments, indicating the amount of calcite dissolved. From these data, the Ca^{2+} concentration was reduced from 3 to 4 ppm in the beginning of the experiment and to 0–1 ppm by the end of the experiments. The ICP-MS results acquired from the dissolution of the calcite product after reaction with chromium (Table 3) indicate that very small amounts of $Cr^{(VI)}$ ($5.5{\cdot}10^{-4}$ to $1.4{\cdot}10^{-3}$ mg/m^2) were adsorbed onto calcite during the stirred flow-through dissolution experiments. The amount of $Cr^{(V)}$ adsorbed onto calcite in experiment 3 and 5 varies by a factor of 2, even though the experiments had the same initial conditions (100 ppm $Cr^{(V)}$, pH 12). However, due to experimental problems, a portion of the calcite in the reactor in experiment 3 was trapped in areas without contact to the $Cr^{(VI)}$-rich solution. The results of experiment 3 are therefore less reliable than the results of experiment 5.

4. Discussion

4.1. Sequestration of $Cr^{(VI)}$ on calcite

The formation of precipitates during the AFM dissolution experiments indicates that a new mineral grew as the calcite surface was dissolving. We interpret this observation as the result of a coupled dissolution-precipitation process. In this mechanism the boundary layer of fluid at the calcite surface becomes increasingly saturated with ions as calcite dissolves. This leads to local supersaturation with respect to a new phase followed by precipitation of this phase at the calcite surface. Such a process occurs when dissolution is faster than diffusion of ions away from the reacting surface resulting in a boundary fluid layer whose composition varies greatly from the bulk composition (Putnis, 2009; Putnis and Putnis, 2007; Ruiz-Agudo et al., 2014).

Our EDS maps show that the newly formed precipitates contain Cr (Fig. 3a-c). This is corroborated by Raman spectroscopy data (Fig. 3d and Table 1). Raman bands in the region between 485 and 848 cm^{-1} are associated to $Cr^{(VI)}$-O bridging bonds in Cr-oxides (Maslar et al., 2001) and the symmetrical stretching motion in both chromate solution and minerals (Kiefer and Bernstein, 1972). Similarly, chromate incorporated into calcite produces multiple bands in the 800–900 cm^{-1} spectral region (Sánchez-Pastor et al., 2010). However, no additional bands were reported close to 400 and 600 cm^{-1} upon incorporation of chromate into calcite. Although the chromate source, Na_2CrO_4, has the characteristic bands for chromate around 800 cm^{-1} (Carter and Bricker, 1974), the band at 600 cm^{-1} in our Raman spectra does not fit this phase. Crystalline phases described in previous studies (Frost, 2004; Sánchez-Pastor et al., 2010) showed multiple, sharp bands in the chromate region. In contrast, the precipitates found here show a single, broad band in this region indicating that our chromate-rich phase had a low crystallinity and/or very small particle size (Nasdala et al., 1995).

For the growth experiments, EDS mapping shows that the layer on top of calcite contains C, Ca and O. Even though we cannot detect any $Cr^{(VI)}$ in the structure with this technique, $Cr^{(VI)}$ clearly had an effect on the calcite growth in the experiments (Fig. 4). Slowing growth in two

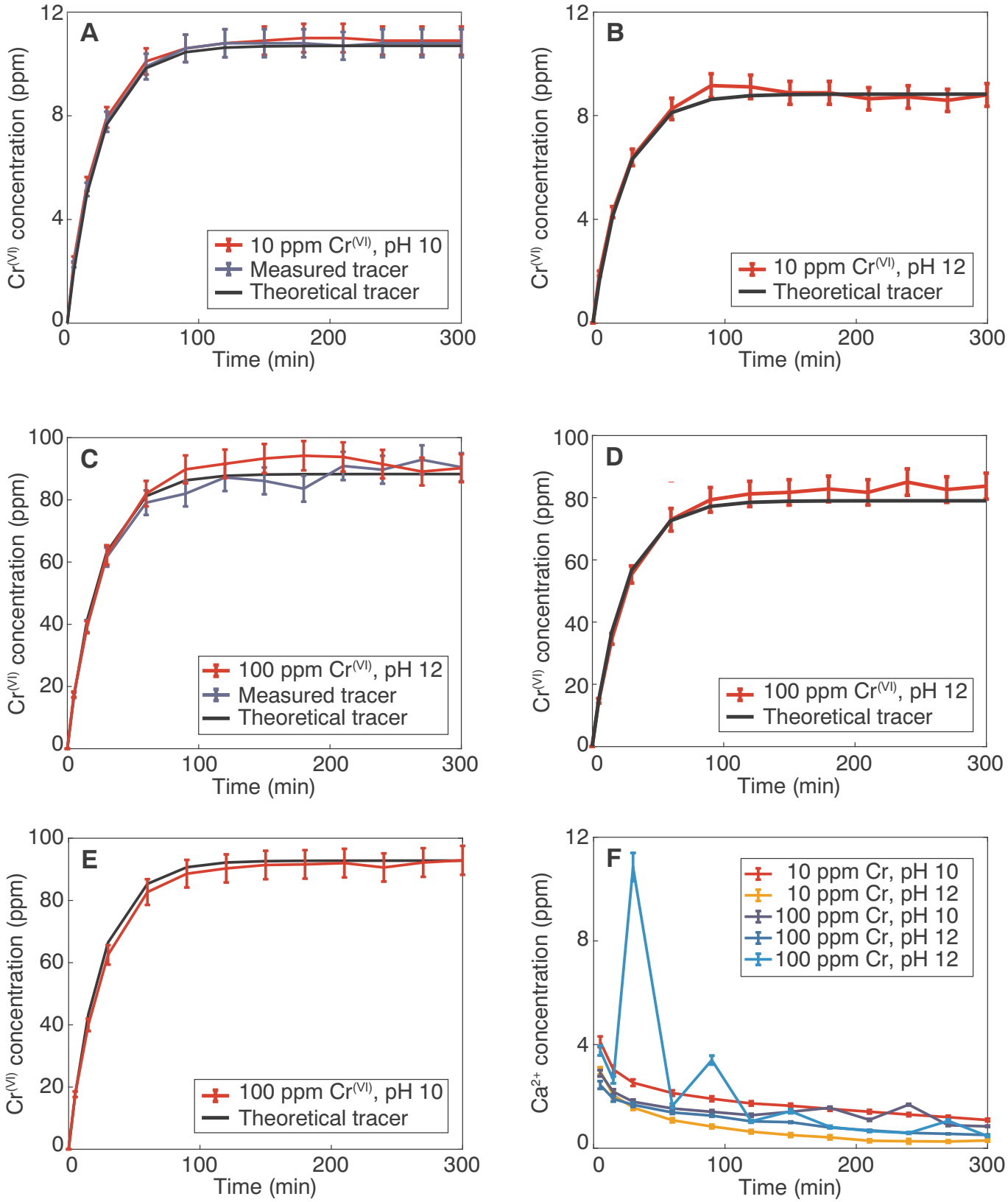

Fig. 7. Concentrations of $Cr^{(VI)}$ and Ca^{2+} in the fluids collected at the outlet of the flow-through reactors for injected solutions with A) 10 ppm Cr, pH 10. B) 10 ppm Cr, pH 12. C) 100 ppm Cr, pH 10. D) 100 ppm Cr, pH 12. E) 100 ppm Cr, pH 12. F) Change in Ca^{2+} concentration with time for all the experiments. The blue curves show the concentrations of the outlet solution for the reactor that did not contain calcite. The black curve is the theoretical tracer, calculated from Eq. (2). (For interpretation of the references to color in this figure legend, the reader is referred to the web version of this article.)

directions on the islands agrees with the results of Tang et al. (2007), who found that most of the CrO_4^{2-} was incorporated into the – steps on the $(10\bar{1}4)$ plane of the calcite surface. Our AFM and SEM data indicate that $Cr^{(VI)}$ is incorporated and retards calcite growth along the same steps. For all the samples that were left for longer times in solution, a layer was formed on the calcite surface. EDS and Raman for the dissolution experiments and EDS for the grow experiments indicate that it is a chromate-bearing layer, but we are not able to identify the exact phase, possibly because of low crystallinity.

4.2. Passivation and solubility of Cr-layer

For two of the experiments (CaCrD03 and CaCrG09), passivation of the surface was observed. García-Sánchez and Álvarez-Ayuso (2002) studied sorption of $Cr^{(III)}$ on calcite and observed a coating of $Cr^{(III)}$ precipitates which they identified as an chromium oxide hydrocarbonate with the general stoichiometry $Cr_2O_3(H_2O)_x(CO_2)_y$. They observed that this precipitation continued until the coating was thick enough to prevent further reaction with the calcite surface, i.e. it passivated the calcite surface. Our data demonstrate that $Cr^{(VI)}$ shows the same behavior and can quickly form a passivating layer on the surface of the calcite crystals. Exposure of the layer, formed in the calcite growth experiment, to deionized water indicates that the new phase has a low reactivity with respect to $Cr^{(VI)}$ release.

From the stirred flow-through experiments, we did not observe a significant adsorption of $Cr^{(VI)}$, and the ICP-MS analyses of the calcite powder left in contact with a chromium solution also indicate that little $Cr^{(VI)}$ was incorporated or adsorbed. Several scenarios could explain these results. As shown in Fig. 7f, the amount of released Ca^{2+} is decreasing with time in the flow-through experiments. This observation could be due to the fact that the calcite surface became passivated quickly by the presence of a new layer, as observed directly in AFM dissolution experiments. This effect would stop calcite dissolution and prevent the build-up of a newly precipitated layer. As the coupled dissolution-precipitation reaction is dependent on the relative rates of the calcite dissolution and Ca diffusion, another explanation is that the solution reached equilibrium with respect to calcite, which deactivated the chemical feedback that controls the formation of a precipitate. The latter hypothesis is confirmed by thermodynamic calculations using PHREEQC and the fluid composition measured by ICP-AES in the outlets of the flow-through reactor. The calculations are based on the information from the ICP-AES analyses, where we know that the concentrations of dissolved Ca^{2+}-ions are ~2 and 4 mg/L (Fig. 7f) in solutions at pH 10 and 12. These calculations indicate that the outlet fluid composition is close to equilibrium with calcite. This result shows that a fluid far-from equilibrium with respect to calcite should be injected continuously into the reactor and at a fast enough rate to maintain the dissolution-precipitation process. To obtain similar uptake to that observed by Tang et al. (2007), the flow-through experiments would need to be run for longer durations at faster flow-rates and/or be performed with much higher Cr-concentrations.

4.3. Implications and environmental relevance

Several studies have shown that Cr in groundwater can occur due to natural pollution, such as from alluvial-filled basins (Robertson, 1975), ophiolitic rocks (Fantoni et al., 2002) and ultramafic rock weathering (Moraetis et al., 2012). Interference of background natural pollution levels of Cr transported to other areas (Moraetis et al., 2012) make it difficult to estimate industrial impact (Shtiza et al., 2005) on Cr concentrations. Nevertheless, it is clear that Cr can be highly mobile in groundwater systems (Moraetis et al., 2012) and those contaminated by wastewaters. Interestingly, there is already evidence of calcite changing the local concentrations of Cr as drill cuttings from Robertson (1975) revealed that pore water in soils consisting of quartz, montmorillonite and calcite, but no Cr source rock, contained up to 60 ppm Cr. The amount of $Cr^{(VI)}$ increased with increasing pH in the range found in the soils, pH 7–9, due to oxidation of $Cr^{(III)}$ (Robertson, 1979). Analyses of the soil material indicated $Cr^{(VI)}$ concentrations between 5 ppm and 120 ppm even though there were no chromate minerals or ions present in the materials. Compared with our experiments within this pH range (7–9), we expect that new Cr-rich minerals could be formed in the presence of calcite, which could explain the presence of $Cr^{(VI)}$ in the soil material. A similar process is expected to occur in the presence of $Cr^{(III)}$ as demonstrated by García-Sánchez and Álvarez-Ayuso (2002).

Cr-containing minerals such as putnisite, $SrCa_4Cr_8^{3+}(CO_3)_8SO_4(OH)_{16}{\cdot}25H_2O$, have recently been found associated with the weathering of carbonate and ultramafic rocks (Elliott et al., 2014), supporting the critical role of chemical feedbacks between minerals and fluids to predict Cr mobility. We suggest that the presence of calcite can reduce the amounts of mobile Cr in groundwater via adsorption or incorporation into the calcite structure or the formation of a stable phase by a coupled dissolution-precipitation mechanism depending on whether calcite is forming coevally or is already present in the system.

5. Conclusion

Chromium can be found as a contaminant in several natural systems, particularly those associated with ophiolitic and ultramafic rocks (Robertson, 1975; Fantoni et al., 2002; Shtiza et al., 2005; Moraetis et al., 2012). Due to its resistance to corrosion, Cr is widely used in industry, increasing pollution levels in soils and groundwaters in industrial areas (Moraetis et al., 2012). The mobility of Cr in these environments will be controlled by chemical feedbacks between the minerals present and dissolved Cr oxyanions. By using in-situ AFM and flow-through experiments we have determined the interaction between $Cr^{(VI)}$ in solution, chromate precipitation, and growing or dissolving calcite surfaces. The results of our experiments reveal that $Cr^{(VI)}$ can become trapped as an oxyanion within nanoparticles at calcite surfaces that are formed due to a coupled dissolution-precipitation mechanism. These new precipitates grow into a layer that covers the calcite surface and this layer can passivate the reaction when porosity in the product phase is low enough. The precipitated phase is more stable and more resistant to dissolution than calcite, indicating that only a limited amount of Cr will be released if the system becomes undersaturated with respect to this phase. Calcite growing in the presence of $Cr^{(VI)}$ is also more resistant to redissolution, indicating stabilization via $Cr^{(VI)}$ adsorption or incorporation into the calcite crystal structure, as observed in previous studies (Hua et al., 2006; Tang et al., 2007). Stirred flow-through experiments did not show significant adsorption of $Cr^{(VI)}$ onto calcite surfaces during the time-scale of our experiments, but ICP-MS analyses indicated that some $Cr^{(VI)}$ was trapped. Such a small amount of Cr trapping could be related to the passivation of the calcite surface by nanoparticle precipitates. From the results presented here, the use of calcite (limestone) barriers could be a suitable remediation strategy for the removal or sequestration of toxic Cr from contaminated water if passivation can be avoided, for example if the fluid has a long enough residence time such that species can diffuse through a passivating layer.

Supplementary data to this article can be found online at https://doi.org/10.1016/j.chemgeo.2020.119770.

Declaration of competing interest

The authors declare that they have no known competing financial interests or personal relationships that could have appeared to influence the work reported in this paper.

Acknowledgment

We thank A. Røyne for fruitful discussions and feedback on the manuscript. V. Rapelius is thanked for helping with ICP-OES analyses at Münster University and Sarah Bureau and Sylvain Campillo for help with ICP-AES and ICP-MS analyses at the University Grenoble Alpes. C.V.P. acknowledges funding through the Marie Curie ITN CO2React. Funding from Labex OSUG@ 2020 (Investissement d'avenir-ANR10-LABX56) and the University of Oslo are also acknowledged.

The data (AFM images and ICP-AES data) is available upon request to the corresponding author.

References

Bartlett, R., James, B., 1979. Behavior of chromium in soils: III. Oxidation. J. Environ. Qual. 8, 31–35. https://doi.org/10.2134/jeq1979.00472425000800010008x.

Carter, R.L., Bricker, C.E., 1974. The Raman spectra of crystalline Na_2CrO_4 and $Na_2CrO_4{\cdot}4H_2O$. Spectrochim. Acta Part A Mol. Spectrosc. 30, 1793–1800. https://doi.org/10.1016/0584-8539(74)80130-3.

Cornelis, G., Johnson, C.A., Gerven, T. Van, Vandecasteele, C., 2008. Leaching mechanisms of oxyanionic metalloid and metal species in alkaline solid wastes: a review. Appl. Geochem. https://doi.org/10.1016/j.apgeochem.2008.02.001.

Deakin, D., West, L.J., Stewart, D.I., Yardley, B.W.D., 2001. Leaching behaviour of a chromium smelter waste heap. Waste Management Series 1 (C), 392–401. https://doi.org/10.1016/S0713-2743(00)80051-3.

EFSA, 2014. Scientific Opinion on the Risks to Public Health Related to the Presence of Chromium in Food and Drinking Water. Parma, Italy. https://doi.org/10.2903/j.efsa.2014.3595.

Elliott, P., Giester, G., Rowe, R., Pring, A., 2014. Putnisite, $SrCa_4Cr_8^{3+}(CO_3)8SO_4(OH)16{\cdot}25H_2O$, a new mineral from Western Australia: description and crystal structure. Mineral. Mag. 78, 131–144. https://doi.org/10.1180/minmag.2014.078.1.10.

Fantoni, D., Brozzo, G., Canepa, M., Cipolli, F., Marini, L., Ottonello, G., Vetuschi Zuccolini, M., 2002. Natural hexavalent chromium in groundwaters interacting with ophiolitic rocks. Environ. Geol. 42, 871–882. https://doi.org/10.1007/s00254-002-0605-0.

Frost, R.L., 2004. Raman microscopy of selected chromate minerals. J. Raman Spectrosc. 35, 153–158. https://doi.org/10.1002/jrs.1121.

García-Sánchez, A., Álvarez-Ayuso, E., 2002. Sorption of Zn, Cd and Cr on calcite. Application to purification of industrial wastewaters. Miner. Eng. 15, 539–547. https://doi.org/10.1016/S0892-6875(02)00072-9.

Hajji, S., Montes-Hernandez, G., Sarret, G., Tordo, A., Morin, G., Ona-Nguema, G., Bureau, S., Turki, T., Mzoughi, N., 2019. Arsenite and chromate sequestration onto ferrihydrite, siderite and goethite nanostructured minerals: Isotherms from flow-through reactor experiments and XAS measurements. J. Hazard. Mater. 362, 358–367. https://doi.org/10.1016/j.jhazmat.2018.09.031.

Hua, B., Deng, B., Thornton, E.C., Yang, J., Amonette, J.E., 2007. Incorporation of chromate into calcium carbonate structure during coprecipitation. Water Air Soil Pollut. 179, 381–390. https://doi.org/10.1007/s11270-006-9242-7.

Kiefer, W., Bernstein, H.J., 1972. The resonance Raman effect of the permanganate and chromate ions. Mol. Phys. 23, 835–851.

Limousin, G., Gaudet, J.P., Charlet, L., Szenknect, S., Barthès, V., Krimissa, M., 2007. Sorption isotherms: a review on physical bases, modeling and measurement. Appl. Geochem. 22, 249–275. https://doi.org/10.1016/j.apgeochem.2006.09.010.

Maslar, J.E., Hurst, W.S., Bowers, W.J., Hendricks, J.H., Aquino, M.I., Levin, I., 2001. In situ Raman spectroscopic investigation of chromium surfaces under hydrothermal conditions. Appl. Surf. Sci. 180, 102–118. https://doi.org/10.1016/S0169-4332(01)00338-5.

Montes-Hernandez, G., Renard, F., Geoffroy, N., Charlet, L., Pironon, J., 2007. Calcite precipitation from CO_2-H_2O-$Ca(OH)_2$ slurry under high pressure of CO_2. J. Cryst. Growth 308 (1), 228–236. https://doi.org/10.1016/j.jcrysgro.2007.08.005.

Montes-Hernandez, G., Fernández-Martínez, A., Charlet, L., Tisserand, D., Renard, F., 2008. Textural properties of synthetic nano-calcite produced by hydrothermal carbonation of calcium hydroxide. J. Cryst. Growth 310 (11), 2946–2953. https://doi.org/10.1016/j.jcrysgro.2008.02.012.

Moraetis, D., Nikolaidis, N.P., Karatzas, G.P., Dokou, Z., Kalogerakis, N., Winkel, L.H.E., Palaiogianni-Bellou, A., 2012. Origin and mobility of hexavalent chromium in North-Eastern Attica, Greece. Appl. Geochem. 27, 1170–1178. https://doi.org/10.1016/j.apgeochem.2012.03.005.

Nasdala, L., Irmer, G., Wolf, D., 1995. The degree of metamictization in zircon: a Raman spectroscopic study. Eur. J. Mineral. Beihefte 7, 471–478.

Parkhurst, D.L., Appelo, C.A.J., 2013. Description of input and examples for PHREEQC version 3—a computer program for speciation, batch-reaction, one-dimensional transport, and inverse geochemical calculations: U.S. Geological Survey Techniques and Methods. In: Geol. Surv. Tech. Methods Book. 6. pp. 497. https://doi.org/10.1016/0029-6554(94)90020-5.

Putnis, A., 2009. Mineral replacement reactions. Rev. Mineral. Geochemistry 70, 87–124. https://doi.org/10.2138/rmg.2009.70.3.

Putnis, A., Putnis, C.V., 2007. The mechanism of reequilibration of solids in the presence of a fluid phase. J. Solid State Chem. 180, 1783–1786. https://doi.org/10.1016/j.jssc.2007.03.023.

Putnis, C.V., Renard, F., King, H.E., Montes-Hernandez, G., Ruiz-Agudo, E., 2013. Sequestration of selenium on calcite surfaces revealed by nanoscale imaging. Environ. Sci. Technol. 47, 13469–13476. https://doi.org/10.1021/es403637u.

Rakhunde, R., Deshpande, L., Juneja, H.D., 2012. Chemical speciation of chromium in water: a review. Crit. Rev. Environ. Sci. Technol. 42, 776–810. https://doi.org/10.1080/10643389.2010.534029.

Renard, F., Montes-Hernandez, G., Ruiz-Agudo, E., Putnis, C.V., 2013. Selenium incorporation into calcite and its effect on crystal growth: an atomic force microscopy study. Chem. Geol. 340, 151–161. https://doi.org/10.1016/j.chemgeo.2012.12.017.

Renard, F., Putnis, C.V., Montes-Hernandez, G., Ruiz-Agudo, E., Hovelmann, J., Sarret, G., 2015. Interactions of arsenic with calcite surfaces revealed by in situ nanoscale imaging. Geochim. Cosmochim. Acta 159, 61–79. https://doi.org/10.1016/j.gca.2015.03.025.

Renard, F., Putnis, C.V., Montes-Hernandez, G., King, H.E., 2017. Siderite dissolution coupled to iron oxyhydroxide precipitation in the presence of arsenic revealed by nanoscale imaging. Chem. Geol. 449, 123–134. https://doi.org/10.1016/j.chemgeo.2016.12.001.

Renard, F., Putnis, C.V., Montes-Hernandez, G., King, H.E., Breedveld, G.D., Okkenhaug, G., 2018. Sequestration of antimony on calcite observed by time-resolved nanoscale imaging. Environ. Sci. Technol. 52, 107–113. https://doi.org/10.1021/acs.est.7b04727.

Renard, F., Røyne, A., Putnis, C.V., 2019. Timescales of interface-coupled dissolution-precipitation reactions on carbonates. Geosci. Front. 10, 17–27. https://doi.org/10.1016/j.gsf.2018.02.013.

Robertson, F.N., 1975. Hexavalent chromium in the ground water in Paradise Valley, Arizona. Groundwater 13, 516–527. https://doi.org/10.1111/j.1745-6584.1975.tb03621.x.

Ruiz-Agudo, E., Putnis, C.V., 2012. Direct observations of mineral fluid reactions using atomic force microscopy: the specific example of calcite. Mineral. Mag. 76, 227–253. https://doi.org/10.1180/minmag.2012.076.1.227.

Ruiz-Agudo, E., Kowacz, M., Putnis, C.V., Putnis, A., 2010. The role of background electrolytes on the kinetics and mechanism of calcite dissolution. Geochim. Cosmochim. Acta 74, 1256–1267. https://doi.org/10.1016/j.gca.2009.11.004.

Ruiz-agudo, E., Putnis, C.V., Rodriguez-Navarro, C., Putnis, A., 2011. Effect of pH on calcite growth at constant $a{Ca^{2+}}/a{CO_3^{2-}}$ ratio and supersaturation. Geochim. Cosmochim. Acta 75, 284–296. https://doi.org/10.1016/j.gca.2010.09.034.

Ruiz-Agudo, E., Putnis, C.V., Putnis, A., 2014. Coupled dissolution and precipitation at mineral-fluid interfaces. Chem. Geol. 383, 132–146. https://doi.org/10.1016/j.chemgeo.2014.06.007.

Sánchez-Pastor, N., Cruz, J.A., Gigler, A.M., Park, S., Jordan, G., Schmahl, W., Fernández-Díaz, L., 2010. Microprobe and Raman Investigation of the Zoning in Synthetic Ca (CO_3, CrO_4) Crystals. pp. 197–198.

Shtiza, A., Swennen, R., Tashko, A., 2005. Chromium and nickel distribution in soils, active river, overbank sediments and dust around the Burrel chromium smelter (Albania). J. Geochemical Explor. 87, 92–108. https://doi.org/10.1016/j.gexplo.2005.07.005.

Tang, Y., Elzinga, E.J., Jae Lee, Y., Reeder, R.J., 2007. Coprecipitation of chromate with calcite: batch experiments and X-ray absorption spectroscopy. Geochim. Cosmochim. Acta 71, 1480–1493. https://doi.org/10.1016/j.gca.2006.12.010.

Zhang, M., Reardon, E.J., 2003. Removal of B, Cr, Mo, and Se from wastewater by incorporation into hydrocalumite and ettringite. Environ. Sci. Technol. 37, 2947–2952. https://doi.org/10.1021/es020969i.

APPENDIX

The Appendix contains two figures.

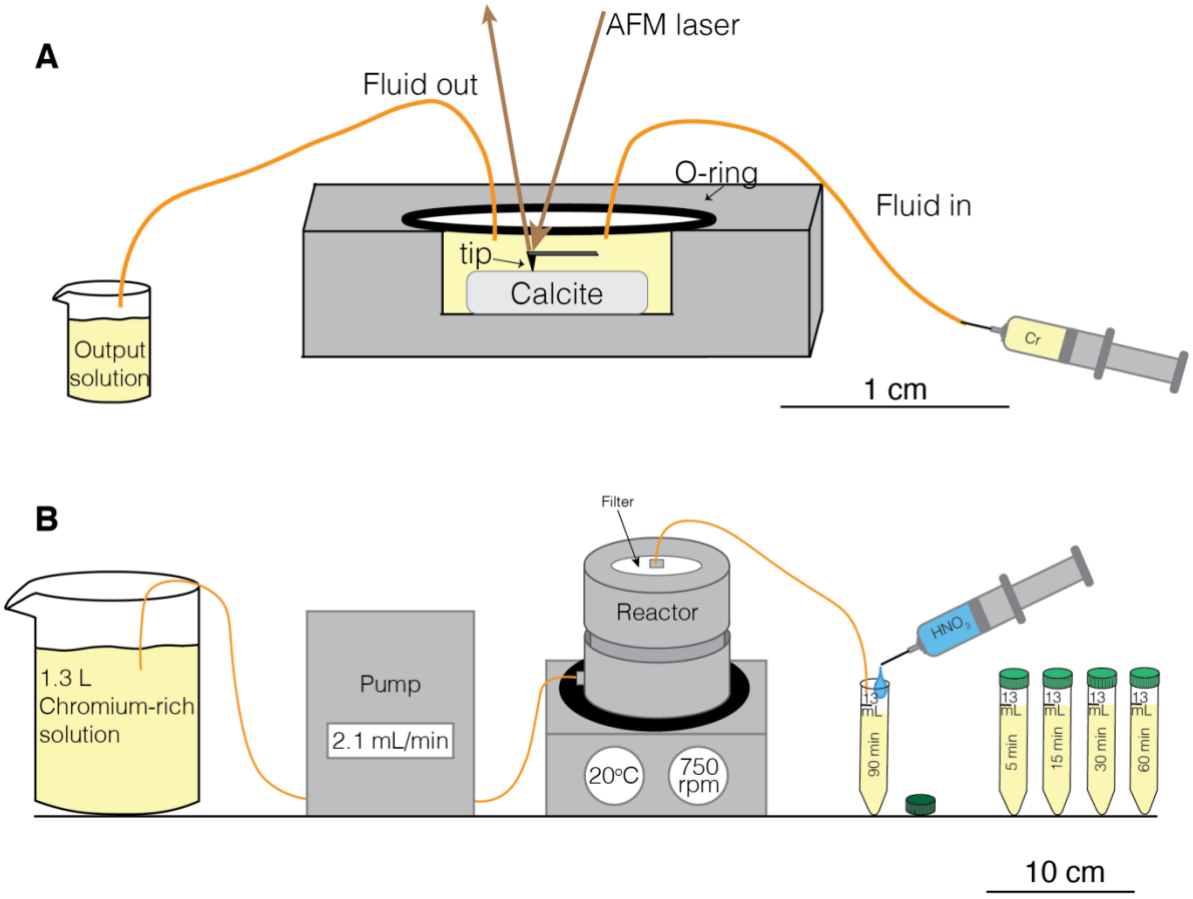

Figure S1. Experimental setups. **A)** Flow-through time-lapse resolved Atomic Force Microscopy (AFM) imaging. **B)** Stirred flow-through reactor.

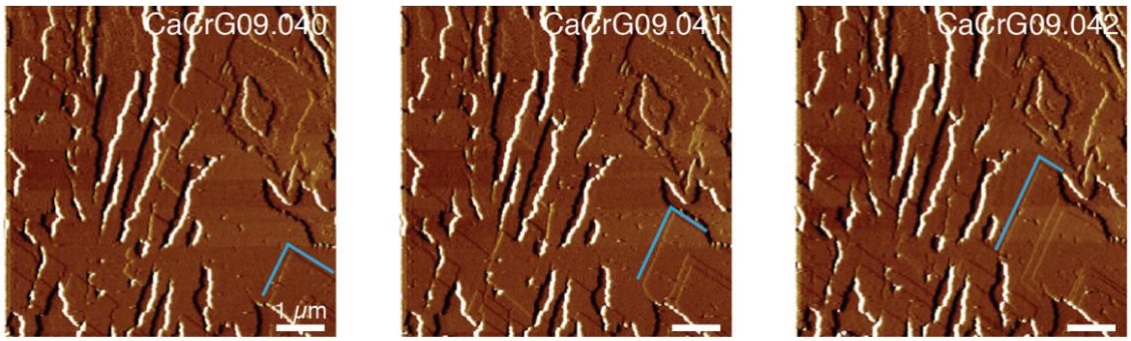

Figure S2. Growth of islands after the formation of a new layer. The blue lines are places right in front of one of the islands that is growing with time.

Paper II

Molecular dynamics study of confined water in the periclase-brucite system under conditions of reaction-induced fracturing

Marthe Grønlie Guren, Henrik Andersen Sveinsson, Anders Hafreager, Bjørn Jamtveit, Anders Malthe-Søressen, François Renard

Published in *Geochimica et Cosmochimica Acta*

II

Available online at www.sciencedirect.com

ScienceDirect

Geochimica et Cosmochimica Acta 294 (2021) 13–27

Geochimica et Cosmochimica Acta

www.elsevier.com/locate/gca

Molecular dynamics study of confined water in the periclase-brucite system under conditions of reaction-induced fracturing

Marthe G. Guren [a,*], Henrik A. Sveinsson [a], Anders Hafreager [a], Bjørn Jamtveit [a], Anders Malthe-Sørenssen [a], François Renard [a,b]

[a] The Njord Centre, Departments of Geoscience and Physics, University of Oslo, Norway
[b] University Grenoble Alpes, University Savoie Mont Blanc, CNRS, IRD IFSTTAR, ISTerre, 38000 Grenoble, France

Received 7 July 2020; accepted in revised form 16 November 2020; Available online 24 November 2020

Abstract

The volume-increase associated with hydration reactions in rocks may lead to reaction-induced fracturing, but requires a stable water film to be present at reactive grain boundaries even when subject to compressive stress. Hydration of periclase to brucite is associated with a solid volume increase of ca. 110%. Recent experiments on the periclase-brucite system observed that when the effective mean stress exceeds 30 MPa, the reaction rate slows down dramatically. We hypothesize that for the brucite forming reaction to progress, the fluid film between grains must remain stable. If the applied pressure becomes larger than the hydration force, the fluid film will collapse and be squeezed out of the grain contacts. To quantify this effect, we study the behavior of a water film confined between periclase or brucite surfaces subject to compressive stress, by performing molecular dynamics simulations. The simulations are carried out using the ClayFF force field and the single point charge (SPC) water model in the molecular dynamics simulations program LAMMPS. The setup consists of two interfaces of either periclase or brucite surrounded by water. Our simulations show that when the pressure reaches a few tens of MPa, the water film collapses and reduces the water film to one or two water layers, while the self-diffusion coefficient of water molecules by a factor of eight. A water film thickness below two water layers is thinner than the size of the hydration shell around Mg^{2+}-ions, which will limit ion-transport. The observed collapse of the water film to a single layer at a normal pressure of 25–30 MPa might explain the observed slow-down of reaction-induced fracturing in the periclase-brucite system.

Keywords: Brucite; Periclase; Hydration force; Confined water; Reaction-induced fracturing

1. INTRODUCTION

Interactions between aqueous solutions and rocks occur in a wide range of environments, from weathering near the Earth's surface to metamorphic reactions in the lower crust. These interactions control the transformations of rocks from one type to another (Jamtveit and Hammer, 2012; Harlov and Austrheim, 2012; Putnis, 2014). Such transformations depend on nanoscale mechanisms controlled by fluid-rock interactions and porosity evolution (Røyne and Jamtveit, 2015). Fluids control the transport of chemical components to and from the grain surfaces where the reactions occur and the supply rate of these components affects the overall rock transformation rate, for example during serpentinization of peridotites (Martin and Fyfe, 1970; Putnis, 2002; Zhang et al., 2019). Reactions at grain contacts in rocks require the presence of porosity, that provides

* Corresponding author.
E-mail address: m.g.guren@geo.uio.no (M.G. Guren).

https://doi.org/10.1016/j.gca.2020.11.016
0016-7037/

fluid pathways, and a fluid film confined along grain boundaries. When this fluid film collapses to two or one water layers, water transport rates decrease, slowing down the reaction rate, as proposed in the context of rock deformation by pressure solution creep (Renard and Ortoleva, 1997; Dysthe et al., 2002). In the present study, we explore the behavior of water confined between periclase or brucite surfaces under conditions where reaction-induced fracturing occurs.

Reaction-induced fracturing is a process whereby the hydration reaction of minerals produces a volume increase leading to the build-up of a force of crystallization and rock fracturing (Martin and Fyfe, 1970; Scherer, 2004). Examples are the hydration of periclase to brucite that occurs with a 110 % solid volume increase and a 45 % weight increase (Kuleci et al., 2016; Zheng et al., 2018), the hydration of calcium oxide to portlandite with a 50 % volume increase (Kelemen et al., 2011), and reactions leading to rock weathering (Røyne et al., 2008). Reaction-induced fracturing may also occur in geo-engineering applications, for example in slowly expanding cements used to prevent leakage in borehole casings (Wolterbeek et al., 2018).

In the Earth's crust, one of the most important reaction-induced fracturing processes is serpentinization (e.g. Martin and Fyfe, 1970) where the hydration of olivine grains can lead to 50 % volume increase (Malvoisin et al., 2017), creating a fracture network in the host rock and enabling fluid circulation and creation of new reactive surface areas. These fractures have been studied extensively in both experiments and numerical models (e.g. Jamtveit et al., 2009; Kelemen and Hirth, 2012; Plümper et al., 2012; Zheng et al., 2018; Zhang et al., 2019), and it has been suggested that the rate of serpentinization is controlled by the rate of water supply to the reaction surface (Martin and Fyfe, 1970). Observations imply that, as the olivine grains are fragmented, the hydration reaction is accelerated because it provides fluid pathways to newly exposed reactive surfaces (Iyer et al., 2008; Zhang et al., 2019).

During mineral hydration and volume increase, a pressure, called the force of crystallization, is produced. This pressure, exerted when a crystal grows from a supersaturated fluid, corresponds to the maximum force this crystal can exert on a solid surface before the reaction stops (Weyl, 1959). The force of crystallization of a hydration reaction can be calculated from thermodynamic data of both the host and forming crystals (Weyl 1959; Eq. 13 in Wolterbeek et al., 2018):

$$\sigma_{force of \ \ crystallization} = \frac{\Delta_f G_i^{P,T} + \Delta_f G_{H2O}^{P,T} - \Delta_f G_j^{P,T}}{V_{m,j}^{P,T} - V_{m,i}^{P,T}} \quad (1)$$

where the subscripts i and j correspond to the host mineral and forming mineral, $\Delta_f G^{P,T}$ is the Gibbs free energy and $V_m^{P,T}$is the molar volume, both at the given pressure and temperature conditions. This force has been measured in a series of experiments where crystals were grown from a supersaturated solution (e.g. Becker and Day, 1916; Correns, 1949; Ostapenko, 1976; Scherer, 2004). Recent studies on the hydration of minerals indicate that the experimental and theoretical values of the force of crystallization may differ by one or two orders of magnitude (Hövelmann et al. (2012); Kelemen and Hirth, 2012; Kuleci et al., 2016; Wolterbeek et al., 2018; Zheng et al., 2018). These large differences could come from a different thermodynamic limit than that given by equation (1) or from a kinetics effect where the reaction would slow down or stop at a pressure much lower than the thermodynamic limit. Experiments have shown that the kinetics of hydration of calcium oxide to portlandite slows down above 135 MPa, compared to the thermodynamic limit of 3.4 GPa (Wolterbeek et al., 2018). Zheng et al. (2018) observed a similar trend for the hydration of periclase to brucite, with a slowdown of the kinetics of transformation above 30 MPa, compared to a calculated thermodynamic limit of 1.9 GPa.

Our study builds on the experimental results of Zheng et al. (2018) who quantified the reaction-induced fracturing process when periclase (MgO) is hydrated into brucite ($Mg(OH)_2$) at temperatures in the range 453–473 K, through the reaction $MgO + H_2O \rightarrow Mg(OH)_2$. This reaction leads to the build-up of a force of crystallization and fracturing of the solid. Zheng et al. (2018) characterized the processes by *in situ* imaging using 4D synchrotron X-ray microtomography with micrometer spatial sampling. They showed that when the effective mean stress applied on the periclase core exceeds ca. 30 MPa, the rate of reaction-induced fracturing slowed down dramatically (Fig. 1a). They interpreted this effect to arise from the removal of water from the grain-grain interfaces. Kuleci et al. (2016) proposed that three kinetic parameters may control the overall rate of the reaction-induced process in the periclase-brucite system: the dissolution rate of periclase; the diffusion rate of ions from periclase to brucite; and the growth rate of brucite. These parameters may control why the brucite-forming reaction slows down under certain conditions of pressure and temperature (Kuleci et al., 2016; Zheng et al., 2018). However, a physical understanding of Zheng et al. (2018) interpretation is lacking and the effect of pressure on the proposed parameters (Kuleci et al., 2016) remains to be characterized.

To increase our understanding of why theoretical and experimental approaches gives such different force of crystallization values, we explore the hypothesis proposed by Zheng et al. (2018) and Kuleci et al. (2016). We study if the water is removed from the grain-grain interface when the normal stress is increasing, and how this affects the diffusion rate of Mg^{2+} ions from periclase to brucite along the grain contacts. The results are obtained from several series of molecular dynamic simulations under conditions relevant for reaction-induced fracturing. Our goal is to characterize the transport properties and hydration force in a water film confined along the interface between two grains.

The grains in the simulations consist of brucite or periclase. Experiments on the hydroxylation process of periclase (e.g. Refson et al., 1995; Oviedo et al., 1998; Lee et al., 2003; Jug et al., 2007) have demonstrated that the periclase (1 0 0) surface restructures into the (1 1 1) crystallographic face when it hydroxylates. This hydroxylated surface shows a similar organization of the atoms as a brucite (0 0 1) surface (Fig. 1b). In periclase (1 1 1) and brucite (0 0 1), the Mg and O atoms are organized in alternating

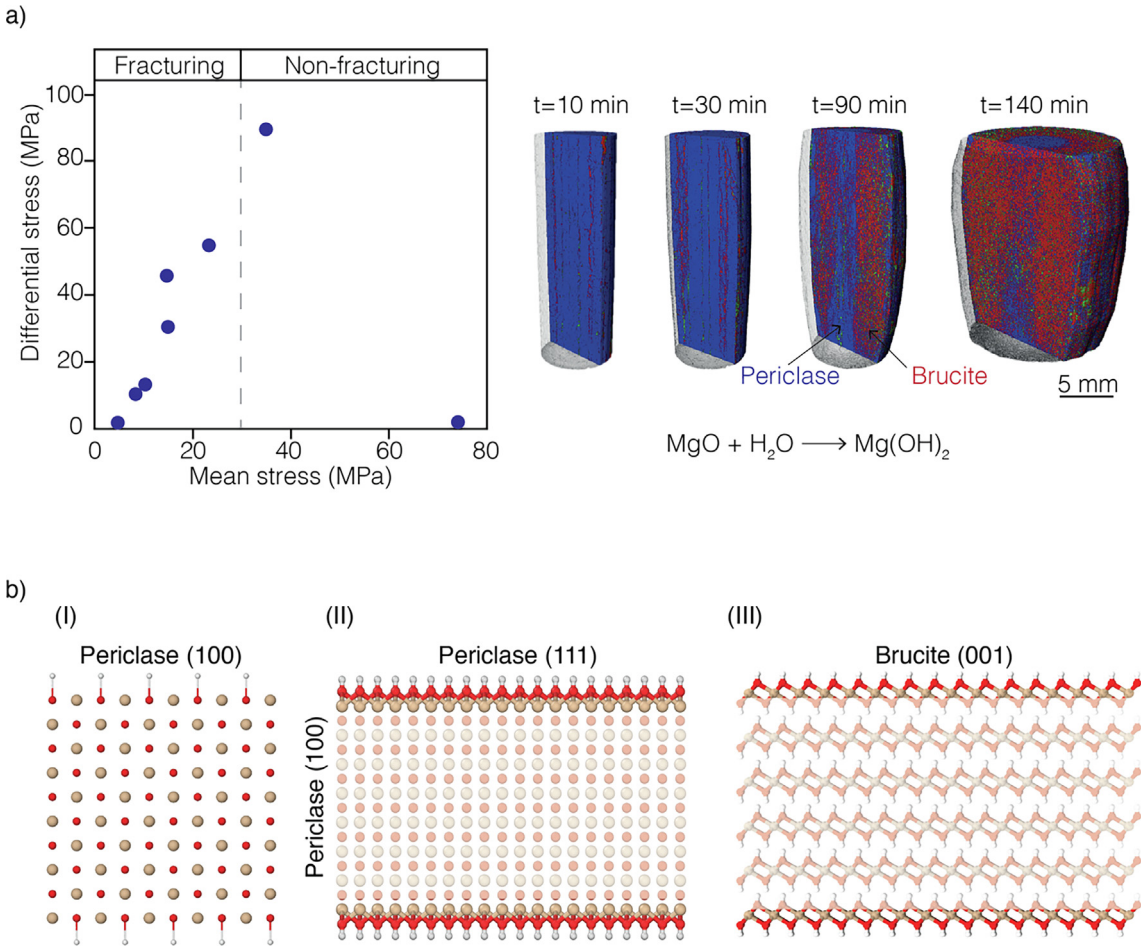

Fig. 1. (a) Experiments of reaction-induced fracturing in the periclase-brucite system performed by Zheng et al. (2018). The blue circles in the diagram represent experimental conditions and the dashed line separates two domains: below ~30 MPa mean effective stress, reaction-induced fracturing of periclase was observed, and above 30 MPa this reaction was not observed during the duration of these experiments. The four cylinders show an experiment performed below 30 MPa mean stress where the transformation from periclase (blue) to brucite (red) with time occurred with a volume increase of 110 % and reaction-induced fracturing of the initial periclase core. (b) Molecular-scale representation of the hydrated surfaces of periclase and brucite. Magnesium atoms are beige, oxygen atoms are red and hydrogen atoms are white. (I) A theoretical hydroxylated periclase (1 0 0) surface. (II) A hydrated periclase (1 1 1) surface, where the top and bottom layers are almost identical to brucite. (III) A brucite (0 0 1) surface. (For interpretation of the references to colour in this figure legend, the reader is referred to the web version of this article.)

planes (Wogelius et al., 1995). We assume that a non-hydroxylated (1 0 0) periclase surface will hydroxylate when it comes in contact with water, creating the (1 1 1) face. The ClayFF force field and later improvements (Cygan et al., 2004; Zeitler et al., 2014; Pouvreau et al., 2017) have been developed for the brucite (0 0 1) face and these values are not necessarily transferrable to the periclase (1 1 1) face. We build on these findings and consider a water film confined between two brucite (0 0 1) surfaces or two non-hydroxylated periclase (1 0 0) surfaces and identify the behavior and properties of the water film under conditions relevant for reaction-induced fracturing. In particular, we determine what stress is necessary to squeeze out layers of the water film from the grain contacts, and how the removal of water layers influences the transport properties of the water film.

2. COMPUTATIONAL METHODS

To study the behavior and properties of a confined water film, we perform four series of simulations; labelled *Brucite-squeeze, Periclase-squeeze, Brucite-transport* and *Periclase-transport* (Table 1). The first name refers to the mineral system, and the second name represents the procedure (*squeeze* out the water film or *transport* properties of a confined water film). Each setup consists of one or two mineral blocks surrounded by water molecules (Figs. 2 and 3a). The studied minerals are brucite ($Mg(OH)_2$) and periclase (MgO).

The transport properties of a water film confined between mineral surfaces are characterized by two parameters: the water film thickness and the self-diffusion coefficient of water molecules in this film (Renard and

Table 1
Overview of the molecular dynamics simulations conditions.

Simulation type	Slab [unit cells]	Pressure [MPa]	Temperature [K]
Brucite-squeeze	10 × 10 × 7	10–100	300, 360, 432, 520
	10 × 20 × 7	53	300, 520
	20 × 10 × 7	53	300, 520
	40 × 40 × 7	53	300, 520
Periclase-squeeze	7 × 13 × 7	10–100	300, 360, 432, 520
Brucite-transport	6 × 6 × 4	10–100	300, 360, 432, 520
Periclase-transport	5 × 5 × 5	10–100	300, 360, 432, 520

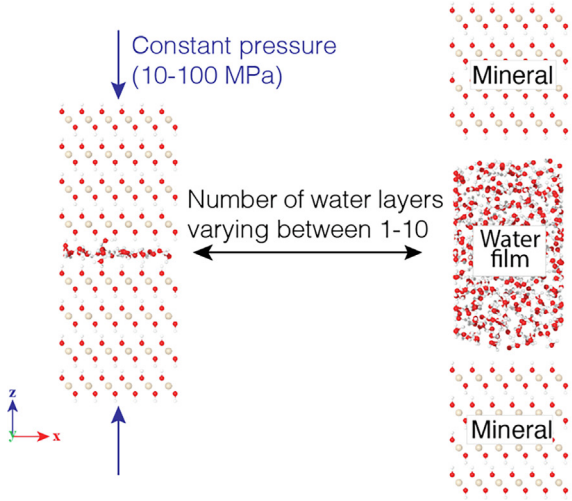

No. of water layers	*Brucite-transport*	*Periclase-transport*
1	35	-
2	70	78
3	105	96
4	140	119
5	175	173
6	210	-
10	350	-

Fig. 2. Molecular dynamics simulation setups for the *Brucite-transport* and *Periclase-transport*. The setup consists of two mineral slabs with a water film confined between them. Conditions are periodic in the three directions. The water film thickness is varied between 1 and 10 layers and the number of water molecules in each layer is given in the table. The thickness of the water film is kept constant through each simulation, independent on pressure and temperature conditions. The mineral slab is periodic in the x- and y-directions. A gap between the mineral and water film is added for clarity. During the simulations, the dimensions of the 3D simulation domain vary with time.

Ortoleva, 1997; Dysthe et al., 2002). To address these two parameters, we use two different methods. The first method (*Brucite-transport* and *Periclase-transport*, Section 3.1, Fig. 2) is used to describe the self-diffusion coefficient of a confined water film. The second method (*Brucite-squeeze* and *Periclase-squeeze,* Section 3.2, Fig. 3) is used to study the change of the thickness of a water film with time when two solids are pushed towards each other. An alternative numerical setup to calculate the effect of pressure on water film thickness is presented in the Appendix (Texts A1, A2 and Fig. A1, A2).

In molecular dynamics simulations, we select a particular thermodynamic ensemble for the simulation. Depending on which ensemble is chosen, three thermodynamic parameters (e.g. temperature, pressure and number of atoms or energy, volume and number of atoms) will be held fixed, while the other parameters are calculated by performing various measurements on the system (Allen and Tildesley, 1987). In the present study, we apply a mechanical load on a solid surrounded by water by letting the simulation domain change with time in x-, y- and z-directions separately to achieve a particular mechanical stress in each coordinate direction (Fig. 3a). This lets us model a quasi-2D pore throat, representing a grain boundary, coupled to a large pore space. The mechanical stress and the temperature are applied by a Nosé-Hoover barostat and thermostat (Shinoda et al., 2004).

We run the simulations with the open source program LAMMPS (Plimpton, 1995), together with the ClayFF force field for the minerals (Cygan et al., 2004). To simulate water, the single point charge (SPC) water model is used because it is compatible with the ClayFF force field (Berendsen et al., 1987; Cygan et al., 2004). Table 2 provides the force field parameters for periclase, brucite and water. The ClayFF force field was developed for clays and hydrated mineral in aqueous solutions, and reproduces bulk properties of clays, including infinite hydroxylated surfaces (Cygan et al., 2004). However, one limitation is that hydroxyl groups on edges and corners of finite size nanoparticles may detach unrealistically and migrate away from the mineral structure (Zeitler et al., 2014; Pouvreau et al., 2017). Zeitler et al. (2014) developed a non-bonded three-body angle term for Mg-O-H in brucite, later improved by Pouvreau et al. (2017), to limit this detachment. We observe that the number of hydroxyl groups that detach in simulations with and without the angle term is quite similar. However, with an angle term, the simulation will stop if hydroxyl-groups detach and move away from

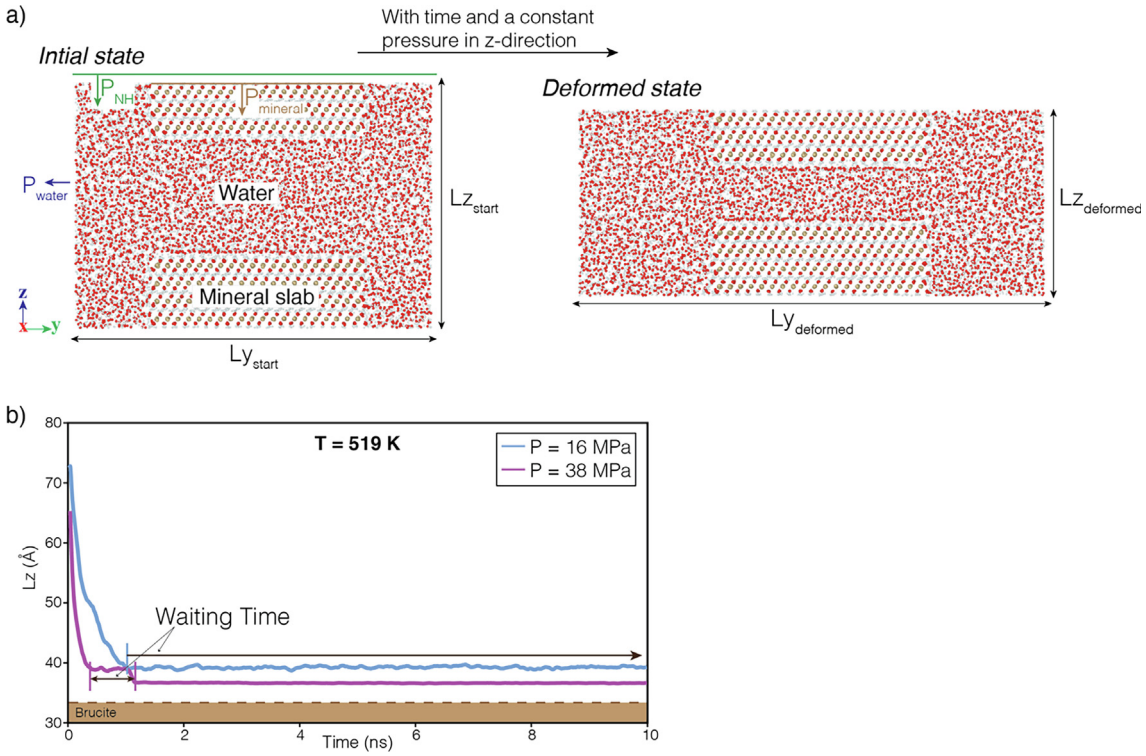

Fig. 3. (a) Molecular dynamics simulation setup for the *Brucite-squeeze* and *Periclase-squeeze* systems. The setup consists of one mineral slab surrounded by water in a three-dimensional domain with periodic boundary conditions. The mineral slab is continuous and periodic in the x-direction (pointing out of the paper plane) and surrounded by water in the y- and z-directions. A Nosé-Hoover barostat (P_{NH}) is applied in the z-direction of the simulation domain. With time, this pressure condition causes the simulation domain to deform ($Lz_{start} > Lz_{deformed}$ and $Ly_{start} < Ly_{deformed}$), slowly thinning the water films near the top and bottom surfaces of the brucite slab. (b) An example of two results from the *Brucite-squeeze* system showing the thickness (Lz) of the simulation domain in the z-direction as a function of time. This figure illustrates how we measure the waiting time. The waiting time is the time it takes for the water film to stabilize at one water layer between brucite grains and two water layers between periclase grains, within 10 ns time limit.

Table 2
Bonded and non-bonded parameters for the ClayFF force field. [1]Values from Zeitler et al. (2014). [2]Values from Cygan et al. (2004).

Non-bonded parameters			
Species	**Charge (e)** [1]	**D_0 (kcal/mol)** [1]	**r (Å)** [1]
H $_{H2O}$	0.41	0	0
O $_{H2O}$	−0.82	1.554	3.16684492
Mg $_{MgO}$	1.36	$9.030\ 10^{-7}$	4.69188948
O $_{MgO}$	−1.36	0.1554	3.16684492
Mg $_{Mg(OH)2}$	1.05	$9.030\ 10^{-7}$	4.69188948
O $_{OH}$	−0.95	0.1554	3.16684492
H $_{OH}$	0.425	0	0

Bonded parameters	
Bond stretch (H_{H2O}-O_{H2O})	
k_1 (kcal/mol Å^2) [2]	Rigid
r_0 (Å) [2]	1.0
Angle bend (H_{H2O}-O_{H2O}-H_{H2O})	
k_1 (kcal/mol rad^2) [2]	Rigid
angle (degrees) [2]	109.47

the solid. Therefore, we run our simulations without the angle term, and ignore the detachment of hydroxyl groups.

We performed all simulations in the pressure range 10–100 MPa and temperature range 300–520 K, relevant for thermodynamic conditions in the Earth's upper crust. To confirm that the force field parameters can be used at these conditions, we studied the evolution of the lattice parameters of brucite at these pressure and temperature ranges and compared with experimental values (Catti et al., 1995; Duffy et al., 1995; Nagai et al., 2000; Fukui et al.,

2003). The results of these simulations can be found in the Appendix (Text A3, Fig. A3) and show that the ClayFF force field can be used at the pressure and temperature conditions used in the present study. The conditions for the different simulations are given in Table 1.

2.1. Water transport and structural properties

The *Brucite-transport* and *Periclase-transport* simulations were performed to study the transport and structural properties of confined water films. The setup consists of two slabs of the same mineral, either periclase or brucite, with a water film confined between them (Fig. 2). These simulations were conducted in the NPT ensemble, where the number of atoms, the pressure and the temperature are held fixed. We used seven different water film thicknesses, varying in the range 1–10 water layers (Fig. 2). To study the structural properties of a confined water film between mineral surfaces, we calculated atomic density profiles for hydrogen and oxygen atoms between brucite surfaces in the *Brucite-transport* simulations, using a similar setup as in Wang et al. (2004). The self-diffusion coefficient of water molecules is calculated with two metrics. First, it is calculated as the average of the mean square displacement of water molecules over ten simulations where each run was executed for a duration of 10 ps with a timestep of 1 fs. Second, we used the velocity autocorrelation function and the simulation duration was decreased to 1 ps and sampled 100 times with a timestep of 1 fs. The velocity autocorrelation function (Fig. A4) was used to verify that the results are identical with both methods. The self-diffusion coefficients given in the results and discussions are measured with the mean square displacement. To estimate the activation energy, the diffusion constant is calculated at different temperatures and then an Arrhenius plot based on the equation $D = D_0 \times \exp(-E_a/R(T-T_0))$ is made, where D is the self-diffusion coefficient at temperature T, D_0 is the self-diffusion coefficient at $T_0 = 300$ K, E_a is the activations energy, and R is the gas constant. The activation energy of self-diffusion of water is calculated for all the water film thicknesses.

2.2. Setup to squeeze out a confined water film

For the *Brucite-squeeze* and *Periclase-squeeze* simulations, we placed a slab of either brucite or periclase in the middle of the simulation domain, and the slab was surrounded by water (Fig. 3a). For brucite, we used three different sizes of the slab (Table 1), where the larger systems are used to characterize the effect of domain size on the removal of water from the interface. For periclase, we used one size of the slab which was chosen such that the surface area was the same as for the smallest brucite slab. The slab spans the whole simulation domain in the x-direction, but leaves room for water in the y- and z-directions. Conditions are periodic in the three directions. The simulation domain contains an initial extra space of 4.1 nm in the y-direction and 3.4 nm in the z-direction, both spaces being filled with water (Fig. 3a). The simulations are run with a barostat set in the z-direction of the simulation domain. With time, the domain dimensions vary (Fig. 3a) as the domain is compressed in the z-direction. At the same time, the domain extends in the y-direction to accommodate the water removed from the brucite interface, such that the water density in the entire system is conserved. We update the pressure on the domain walls (P_{NH}) every 10 ps to keep the pressure acting on the mineral surface (P_{mineral}) constant as the domain dimensions changes, following equation (2):

$$P_{NH} = \frac{P_{mineral} \cdot A_{mineral} + P_{water} \cdot (A_{box} - A_{mineral})}{A_{box}} \quad (2)$$

where P_{mineral} is the pressure acting on the mineral slabs (Fig. 3), P_{water} is the water pressure on the boundaries of the simulation domain. P_{water} is set to be constant and equal to 10 MPa, while P_{mineral} is kept constant by adjusting P_{NH} with time. A_{mineral} and A_{box} are the surface areas of the brucite slab and simulation domain, respectively, in the x- and y-directions.

The simulations are run for up to 10 ns. We measure the time it takes for the water film to stabilize at one water layer between brucite grains and two water layers between periclase grains, within 10 ns time limit. The last layer(s) of water are weakly bonded to the surfaces and will therefore stay trapped between the mineral surfaces. The waiting time to reach one or two water layers is measured in a series of simulations in the pressure range 15–40 MPa and 519 K.

2.3. Computational details

The mineral structures of periclase and brucite, with space groups Fm3m and $P\bar{3}m1$ are constructed from published unit cells (Zigan and Rothbauer, 1967; Sasaki et al., 1979) using the Atomic Simulation Environment (ASE) software (Larsen et al., 2017). The water is simulated with the single point charge (SPC) model (Berendsen et al., 1987). In the simulation domain, the water has an initial density of 1000 kg/m^3. To pack the water, randomly and without overlap, we use the software package packmol (Martinez and Martinez, 2003), and set the tolerance distance to 2.0 Å, which is the minimum distance between a mineral structure and water molecules. All simulations are run using periodic boundary conditions in the three directions of space. The ClayFF potential has a 12–6 Lennard-Jones potential. We set the cut-off distance to be 8.0 Å and set the long-range Coulombic interactions, calculated using particle–particle particle-mesh (pppm), with a relative precision of 10^{-4} (dimensionless). Harmonic bond stretching and angle bending between bonded atoms are optional. We enforce rigid bonds and angles of the water molecules and in hydroxyl groups of brucite using the SHAKE algorithm (Ryckaert et al., 1977). This allows for a time step of 1 fs during simulations.

3. RESULTS

3.1. Self-diffusion coefficient and density profiles in the confined water films

The atomic density profiles of oxygen (Fig. 4a) and hydrogen (Fig. A5) atoms in a direction perpendicular to

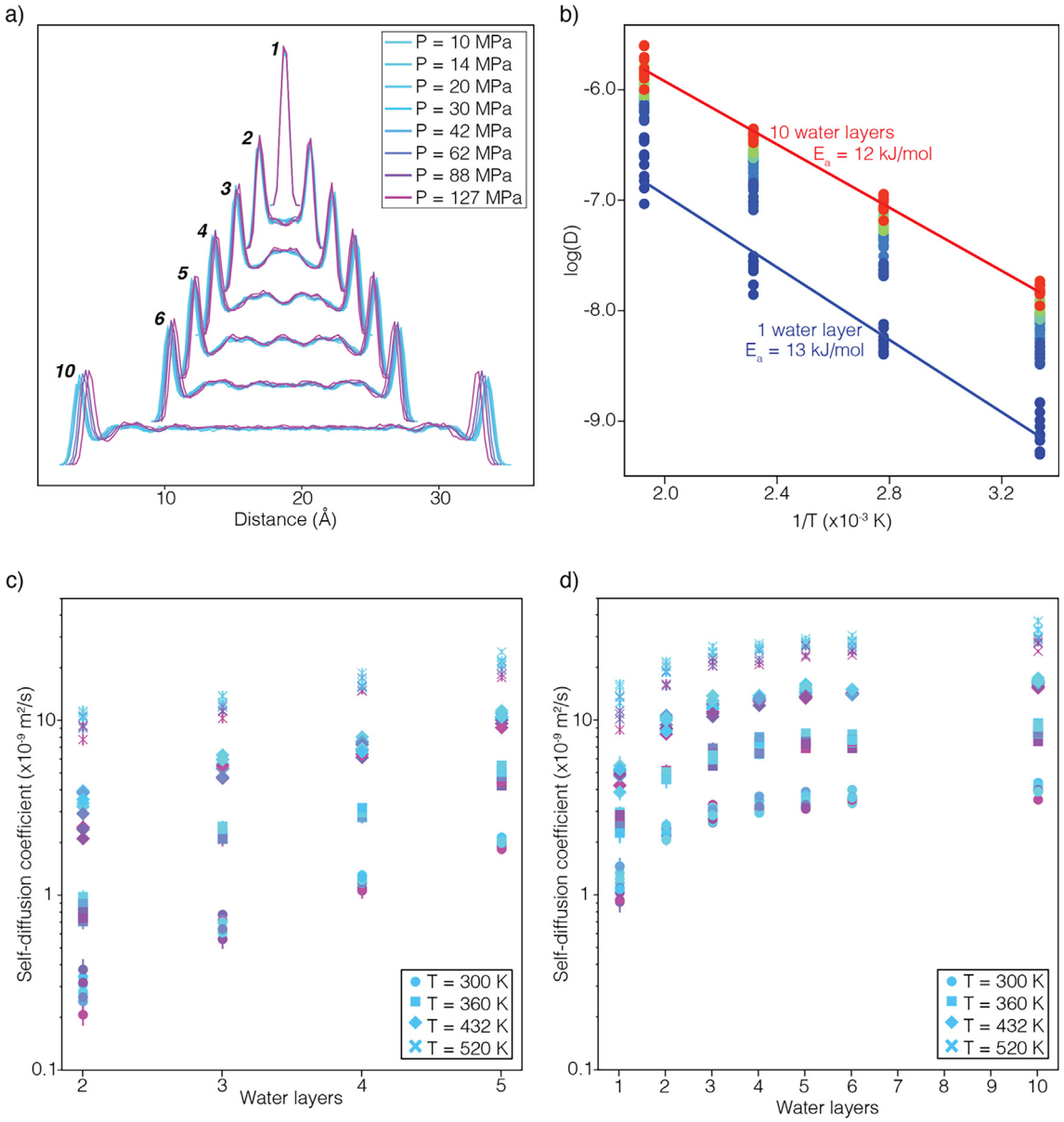

Fig. 4. Atomic density profiles and diffusion coefficient of water films confined between periclase or brucite surfaces (see Fig. 2 for geometry). (a) Atomic density profiles for the oxygen atoms in a water film confined between two brucite grains. The digits on the left side of each curve indicate the number of water layers contained in the water film. The curves are shifted vertically for clarity. Fig. A5 displays similar profiles for the hydrogen atoms. b) Self-diffusion coefficient of water as a function of 1/T for 1 (dark blue) to 10 (red) water layers between brucite surfaces. E_a = Activation energy. Fig. A6 displays a similar plot for periclase. (c-d) Self-diffusion coefficient in the xy-directions of water molecules between (c) brucite and (d) periclase slabs, calculated with mean square displacement. Each point corresponds to a pressure between 10 and 100 MPa, and is colored from low (light blue, 10 MPa) to high (purple, 100 MPa) pressure. Symbols show results at different temperatures in the range 300–520 K. (For interpretation of the references to colour in this figure legend, the reader is referred to the web version of this article.)

the plane of the water film between brucite surfaces demonstrate a structural organization of the atoms. This organization in layers with different densities is present for thin film thicknesses of up to five water layers. When the water film is thicker, only the two layers closest to each surface show a density structural organization.

The self-diffusion of bulk water, measured in the xy-directions, does not vary much with mineral interface (periclase or brucite) or the pressure, with variations less than a factor of 2 in the pressure range 10–100 MPa. The temperature and water film thickness have significant effects on the self-diffusion coefficient of water molecules (Fig. 4c and d).

For periclase, the self-diffusion coefficient of water increases by a factor of 8 when the water film thickness increases from two to five water layers, and a factor of 16 when increasing the temperature from 300 to 520 K. For

brucite, the self-diffusion coefficient increases by a factor of 10 with increasing temperature in the range 300–520 K and by a factor of 3 when the film thickness increases from one to ten water layers.

The activation energy for water molecules diffusion between brucite grains (Fig. 4b) increases from 11.9 kJ/mol to 13.6 kJ/mol when the thickness of the water film decreases from ten to one water layer. For water molecules between periclase grains, the activation energy of diffusion increases from 13.9 kJ/mol to 20.9 kJ/mol (Fig. A6) when the water film thickness decreases from five to two water layers.

3.2. Behavior of a confined water film when squeezed out of grain contact

In the *Brucite-squeeze* and *Periclase-squeeze* systems, the thickness of the simulation domain (Lz, Fig. 3a) changes with time for different pressures, temperatures and slab sizes. The removal rate of water from the interface increases both with increasing pressure and with increasing temperature.

For the *Brucite-squeeze* simulations, Fig. 5a shows that with pressures in the range 40–100 MPa and temperatures in the range 432–519 K, the duration required to reach a water film thickness of one water layer is less than 1 ns while at lower pressures and temperatures this duration can increase to more than 3 ns. At a temperature of 300 K, a pressure higher than 67 MPa is required to decrease the water film thickness to one water layer, while for a temperature of 519 K, the pressure must exceed 18 MPa to reach one water layer within 2 ns.

To study the effect of the size of the brucite slab on the film thickness, we performed simulations with brucite slab sizes in the range 10–40 × 10–40 × 7 unit cells repetitions. These simulations show that when the size of the brucite slab increases from 10 to 40 unit cell repetitions in the y-direction, the time required to reach a thickness of one water layer increases from less than 1 ns to more than 3 ns. Conversely, since the slab is periodic in the x-direction, we observe that increasing the size in the x-direction from 10 × 10 × 7 to 20 × 10 × 7 unit cell repetitions does not affect the duration to reach one water layer (Fig. A7).

For the *Periclase-squeeze* simulations we measure the time necessary to reach a water film thickness of two water layers. Fig. 5b shows that at a temperature of 300 K, the duration to reach a two-layer water film thickness is ~2 ns when the pressure in the range 53–100 MPa, while at lower pressure the water film thickness remains at three or four water layers after 3 ns. At 519 K, the duration to reach two water layers is less than 2 ns for all pressures in the range 15–100 MPa. The results presented in Text A2 and Fig. A2 are consistent with the *Periclase-squeeze* simulations. Fig. A2 shows that when the pressure is below 30 MPa at 453 K, the duration to reach two water layers varies from 2 to 12 ns depending on the crystallographic orientation (Fig. A2b). However, at 453 K and with a pressure above 30 MPa, the duration to reach a two water layer thickness is less than 3 ns, whatever the crystallographic orientation.

For both *Brucite-squeeze* and *Periclase-squeeze* we measured the waiting time for squeezing out the water film at a temperature of 519 K (Fig. 3b). For brucite, we measure the time needed to reach one water layer, while for periclase, we measure the time needed to reach two water layers, because the periclase surface binds water much more strongly than brucite. We interpret these results such that there is a transition between a pressure regime where it is difficult to remove the water layers to a pressure regime where it is easy to remove the water layers. In the *Brucite-squeeze* simulations at 519 K (Fig. 6), we observe that when the pressure is below 25–30 MPa, most of the simulations do not reach the one water layer level, while for pressures above 25–30 MPa a single water layer is reached within a few ns. A few simulations within the pressure range 15–25 MPa reached a water film thickness of one water layer within 2 ns. The deviation from the trend that simulations in this pressure range do not reach one water layer could be due to fluctuations pushing the system over the energy barrier to squeezing out the water film. Results from simulations with an initial shorter distance (decreased from 32 Å to 17 Å) are in agreement and indicate a transition around 25–35 MPa (Fig. A8a). In the *Periclase-squeeze* simulations (Fig. A8b), the transition between simulations that reach two water layers or not is ~15 MPa.

4. DISCUSSION

4.1. Water film thickness and self-diffusion coefficient of a confined water film

The water film thickness is calculated as a function of time under different pressures and temperatures. We observe that the number of water layers that can be removed from the confined water film depends on the mineral interface above and below that water film. For example, for un-hydroxylated periclase surfaces, the last two layers of water remain trapped, while for brucite only one water layer remains (Fig. 5). These results are in agreement with previous numerical and experimental studies performed on un-hydroxylated periclase, which have shown that water binds strongly to the periclase surfaces due to high surface charges and the lattice parameters that maximize interactions between water molecules and MgO units with a ratio of one water molecule for one MgO unit (Stirniman et al., 1996; Engkvist and Stone, 1999). Calculated adsorption energy of water molecules to periclase (0 0 1) and brucite surfaces support that water binds more strongly to periclase than brucite. Asaduzzaman (2020) found the adsorption energy of water molecules in a monolayer to an un-hydroxylated periclase (0 0 1) surface to be −54.5 kJ/mol. For brucite, the adsorption energy of water molecules to the brucite surface is estimated to be ~25 kJ/mol (Sakuma et al., 2004).

The self-diffusion coefficient of water molecules is higher between brucite surfaces than periclase surfaces. The self-diffusion coefficient is also higher in thick water films than in thin ones. The activation energy for self-diffusion increases with a decreasing water film thickness and the sensitivity of this activation energy due to water film thickness

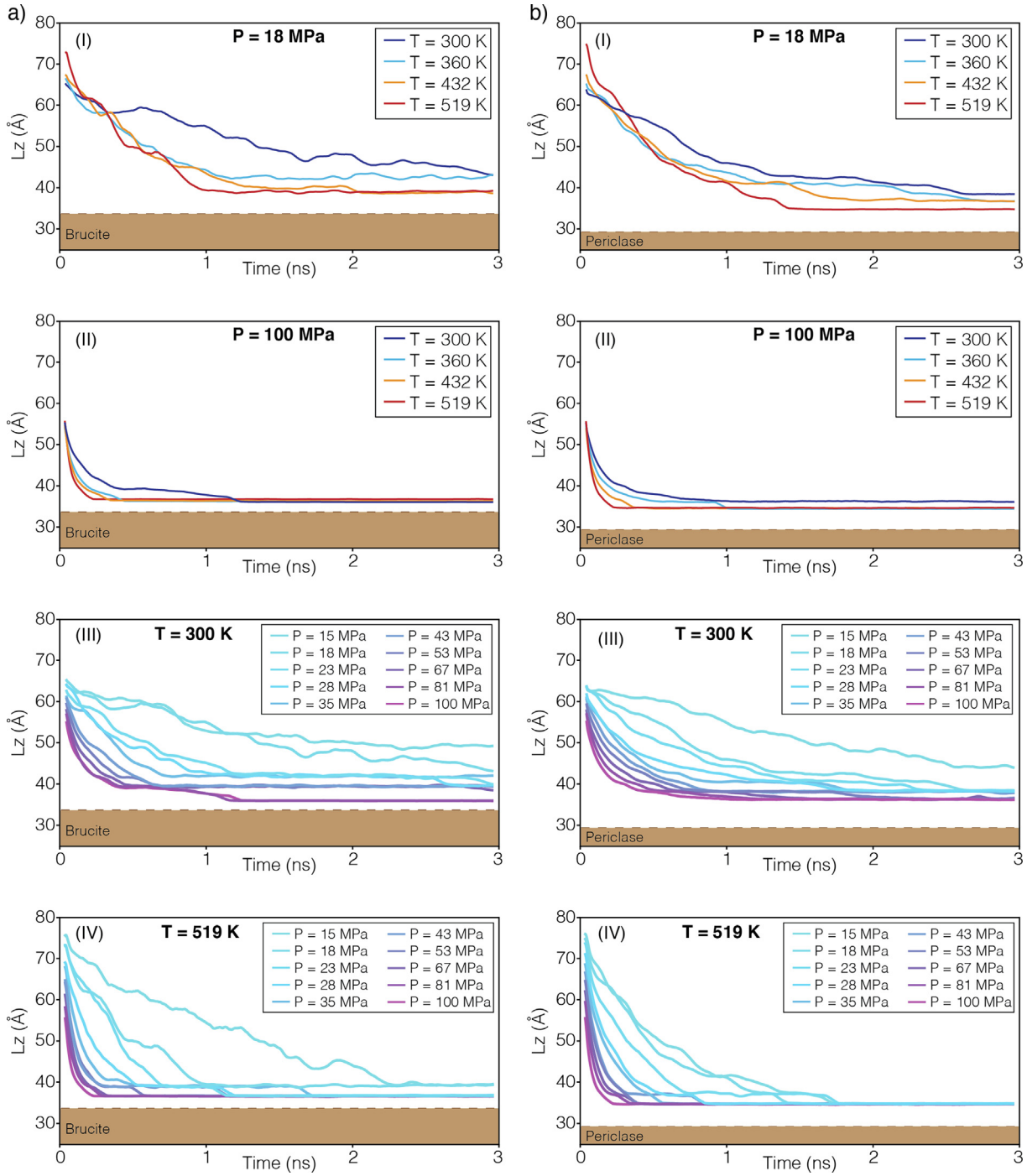

Fig. 5. Thickness (Lz) of the simulation domain in the z-direction as a function of time in the (a) *Brucite-squeeze* and (b) *Periclase-squeeze* simulations (see Fig. 3a for the geometry). (I) and (II) Simulations of the evolution of the water film thickness as a function of time for different temperatures in the range 300–519 K at two pressures (18 and 100 MPa). (III) and (IV) Simulations of the evolution of the water film thickness as a function of four different pressures in the range 15–100 MPa at two temperatures (300 and 519 K).

is higher between periclase surfaces than between brucite surfaces. Numerical studies indicate that the self-diffusion coefficient for bulk water, using single point charge water model at 300 K, is in the range 3–4 $\times$ 10^{-9} m^2/s (Yu and van Gunsteren, 2004; Guevara-Carrion et al., 2011; Tsimpanogiannis et al., 2019), while experimental studies that used nuclear magnetic resonance (e.g. Holz et al., 2000) or a diaphragm cell (Mills, 1973; Easteal et al., 1989) report the self-diffusion coefficient of water to be $\sim$2.3 $\times$ 10^{-9} m^2/s at 300 K. These studies also report the activation energy for water molecules. From experimental studies, the activation energy is reported to be in the range 14.3–18.0 kJ/mol (Mills, 1973; Easteal et al., 1989) while numerical models report slightly lower activation energies

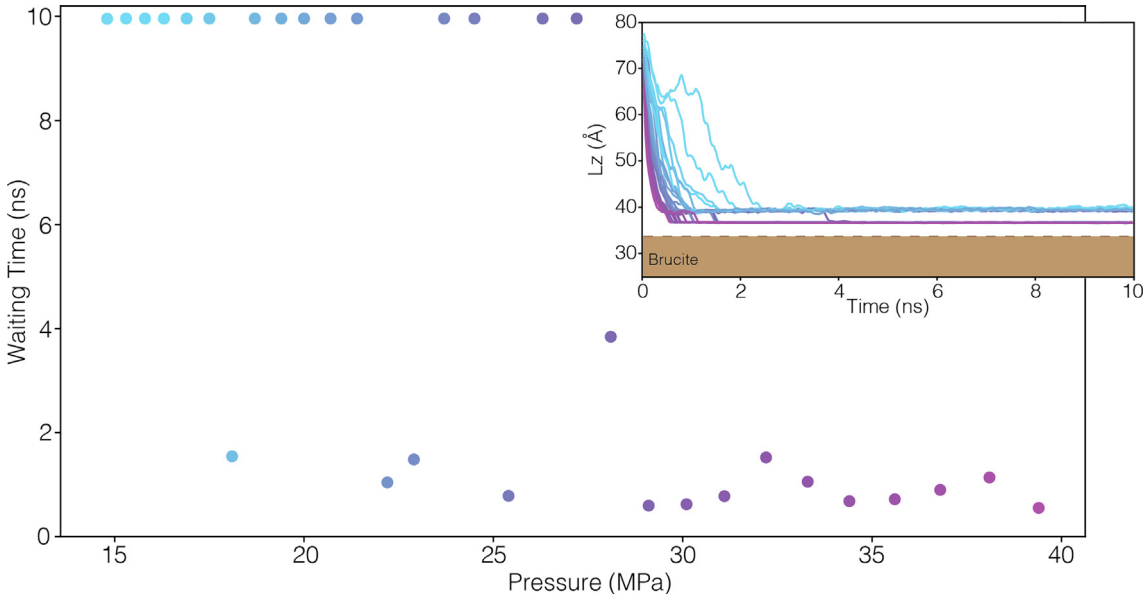

Fig. 6. Waiting time to reach one water layer for the *Brucite-squeeze* simulations. When the waiting time is equal to 10 ns, the water film thickness after 10 ns contained at least two water layers and the waiting time to reach one water layer will be longer than 10 ns. The simulations were performed in the pressure range 15–40 MPa at 519 K. The inset shows how the thickness (Lz) of the simulation domain change as a function of time during 10 ns. Each point corresponds to the waiting time for one line in the inset figure at a pressure between 15–40 MPa and both the lines and points are colored from light blue (15 MPa) to purple (40 MPa). (For interpretation of the references to colour in this figure legend, the reader is referred to the web version of this article.)

between 9.998 and 12.890 kJ/mol (Espinosa et al., 2014; Ding et al., 2016; Tsimpanogiannis et al., 2019). The latter values fit with our estimated activation energies. For a film thickness of five water layers at 300 K, the self-diffusion coefficients for water molecules between periclase and brucite interfaces are $\sim 2 \times 10^{-9}$ m^2/s and $\sim 3 \times 10^{-9}$ m^2/s, respectively. These diffusion rates are slightly lower than the bulk coefficients. The most likely cause is that two of the water layers bind to the surface, as indicated by e.g. Engkvist and Stone (1999) and Lee et al. (2003), decreasing the overall diffusion rate. The activation energy increases by 13 % when the water film thickness decreases from ten to one water layers between brucite surfaces and by 33 % with a reduction from five to two water layer between periclase surfaces. This indicates that the binding of water is stronger between the periclase surfaces than between the brucite surfaces, which also affects the kinetics of diffusion, even though both are hydrophilic minerals.

Several studies characterized the behavior of water on hydrophilic mineral surfaces, such as periclase and brucite (e.g. Lee and Rossky 1994; Marmier et al., 1998; Malani et al., 2009; Phan et al., 2012; Ou et al., 2014 and references therein). These studies showed that in most cases the water molecules form hydrogen bonds at the mineral surface and become structurally ordered, with a reduction in diffusion rate by a factor of 2–5 compared to bulk water. For the periclase system, the diffusion rate can be five times lower than in bulk water (Marmier et al., 1998). However, simulations performed on the brucite system indicate that, in contrast to most hydrophilic minerals, brucite barely affects the diffusion dynamic of water in a thin layer near the mineral surface (Ou et al., 2014). These results are in agreement with our results where the diffusion coefficient of water between brucite surfaces decreases by a factor of 3 when the film thickness decreases from five to one water layers. Conversely, between periclase surfaces, the diffusion coefficient decreases by a factor of almost ten when the water film thickness decreases from five to two water layers, giving a lower self-diffusion coefficient of water molecules than between brucite surfaces. Moreover, the self-diffusion coefficient of water between brucite surfaces is also reduced substantially when the water film thickness is decreased.

4.2. Hydration forces between mineral interfaces

Several types of hydration forces operate between mineral surfaces in aqueous solutions: strongly monotonically repulsive forces, attractive forces, oscillatory forces and combinations of all three forces (e.g. Israelachvili, 2011). The existence of monotonically repulsive forces was first proposed by Langmuir (1938), and described in several other studies (e.g. Parsegian and Zemb, 2011; Kilpatrick et al., 2013; Shen et al., 2018). These studies have demonstrated the existence of two kinds of repulsive hydration forces acting over short distances, depending on the nature of the surfaces. In our case, we consider repulsive hydration forces between solid hydrophilic minerals. If the repulsive forces are smaller than the applied pressure on the system, the water film may collapse to one or two water layers, which reduces the transport properties along the grain boundaries (e.g. Weyl, 1959; Renard and Ortoleva, 1997). Our simulations show that a water film between brucite surfaces is reduced to one layer of molecules when the applied pressure exceeds 25–30 MPa. Our simulations were performed

in the pressure range 10–100 MPa. Even at 100 MPa, the remaining single water layer between the surfaces appears to be stable. Other numerical studies of solvation layers between surfaces of other minerals, such as calcite or aragonite, indicate that two or three water layers remain stable up to 1 GPa (Brekke-Svaland and Bresme, 2018).

4.3. Implications for reaction-induced fracturing

Hydration of periclase to form brucite and associated reaction-induced fracturing due to the expansion of solid volume, requires sustained supply of water to the reactive interfaces. The same applies to the hydration of peridotite to form serpentine. Previous studies of the brucite-forming reaction show that the access of water at the reacting surface could be rate limiting. At high pressures, either the diffusion of ions is significantly slower (Kuleci et al., 2016) or the water film is squeezed out of the grain-grain contact (Zheng et al., 2018) or.

Zheng et al. (2018) quantified the periclase to brucite transition by *in situ* X-ray tomography imaging and characterized the evolution of porosity during the reaction progress. They observed two different behaviors, depending on whether the effective mean stress applied to the samples was above or below 30 MPa. In the experiments where the effective mean stress was below 30 MPa, reaction-induced fracturing was observed. The reaction proceeded through three different stages (Fig. 7a). Stage 1 was characterized by slow replacement of periclase to brucite. During stage

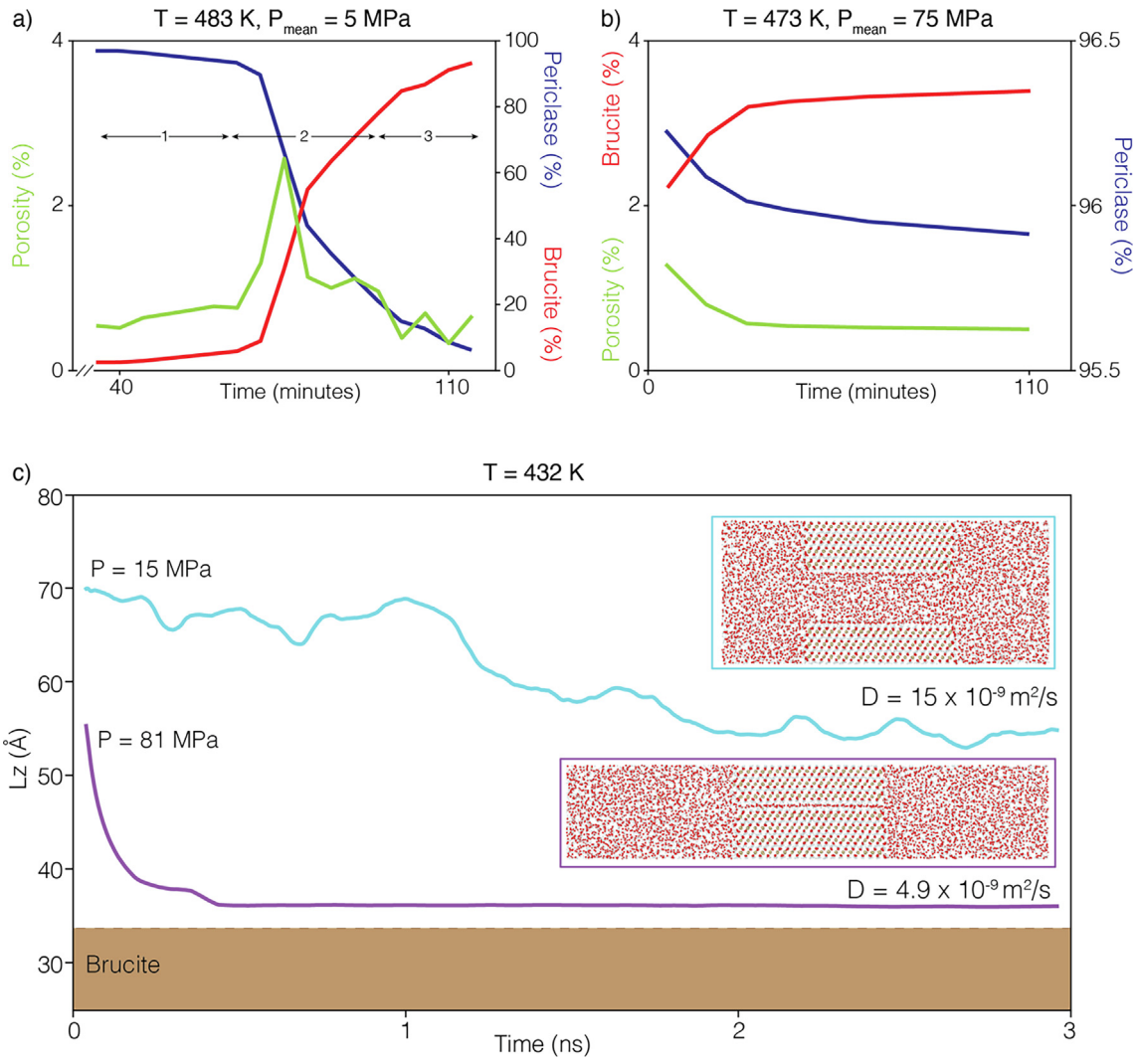

Fig. 7. (a) Evolution of porosity (green), periclase content (blue) and brucite content (red) at a temperature of 483 K and an effective mean stress of 5 MPa during the periclase to brucite reaction (modified from Zheng et al., 2018). The three stages of reaction progress and reaction-induced fracturing are indicated (1: onset of reaction, 2: fracturing induced porosity pulse and 3: pore collapse until complete reaction). (b) Evolution at a temperature of 473 K and an effective mean stress of 75 MPa. No reaction-induced fracturing occurred during the experiment (modified from Zheng et al., 2018). (c) Thickness (Lz) of the simulation domain in the z-direction as a function of time at temperature 432 K with pressures of 15 and 81 MPa. D is the self-diffusion coefficient of the water molecules in water films with the thickness at 3 ns. The inset figures are snapshots at 3 ns, visualizing the water film thickness between the two brucite blocks. (For interpretation of the references to colour in this figure legend, the reader is referred to the web version of this article.)

2, the rate of replacement increased due to the onset of reaction-driven fracturing and a pulse-like porosity increase was observed (Zheng et al., 2018). The example in Fig. 7a shows that a maximum porosity of ~2.5% was reached before the pore space collapsed to less than 1%. When the porosity decreases to 1% or less, the fluid transport must occur along the grain boundaries. Even though some void space along triple junctions exists in natural systems, our 3D simulations of water confined between two parallel plates is relevant to water confined along grain boundaries because in low porosity rocks, the behavior of the confined water films is the determining factor for whether water supply is shut off such that the periclase to brucite reaction stops. During stage 3, the reaction rate decreased until the replacement was complete. After 110 min (Fig. 7a), 95% of the periclase was replaced by brucite.

In contrast, for experiments carried out at mean stress above 30 MPa, reaction-induced fracturing was not observed. During the reaction, the porosity decreased from the initial 1.3% to 0.5% (Fig. 7b), and at the same time, the brucite volume increased to ~3%, suggesting that the initial pores were clogged with brucite without producing new fractures (Zheng et al., 2018).

Fig. 7a and b show the behavior of experiments performed at 473–483 K and 5 MPa and 75 MPa, respectively. Our molecular dynamics simulations performed under similar conditions, 432 K and 15 MPa and 81 MPa (Fig. 7c) show that when the pressure is 15 MPa, below the 30 MPa limit observed in the experiments by Zheng et al. (2018), the water film thickness between two brucite surfaces consists of six water layers after 3 ns, and the self-diffusion coefficient of the water molecules is 15×10^{-9} m^2/s. However, at 81 MPa, the water film thickness is decreased to one water layer thickness within 0.5 ns, and the self-diffusion coefficient of water molecules is reduced to 4.9×10^{-9} m^2/s. The observed occurrence of higher porosity in the experiments below the 30 MPa limit is consistent with our simulations (Fig. 6) and indicate the reaction and fracturing can be maintained in the system when the applied pressure is reduced. However, when the pressure in the experiment is increased to 75 MPa, the reaction slows down and no fracturing occurred. Similarly, the simulation at 81 MPa shows that the water film rapidly collapses to one water layer, and the access of water to the reacting surface and ion-transportation is therefore limited.

To maintain the ion-transport along grain boundaries, the water film has to be thick enough to accommodate the hydration shell of Mg^{2+}. As periclase dissolves, the Mg^{2+} ions hydrate, and the water hydration layers are strongly bonded to the Mg^{2+} (e.g. Bo et al., 2017). Several studies have shown that the first hydration shell around Mg^{2+} ions contains six water molecules, creating a stable octahedral structure, and the second hydration shell contains twelve water molecules which are connected to the first hydration shell with hydrogen bonds (Bol et al., 1970; Pavlov et al., 1998; Bo et al., 2017). The average bond length between Mg^{2+}-water and water-water is 2.07 Å (Pavlov et al., 1998), and the distance for the second hydration shell is reported to be about 4.2 Å from the Mg^{2+}-ion (Bol et al., 1970). This implies that when the water film thickness is reduced to one or two water layers (~3–6 Å), the transfer of Mg^{2+}-ions would be limited due to space restrictions, therefore slowing down the kinetics of reaction-induced fracturing.

5. CONCLUSION

- We propose that reaction-induced fracturing requires a stable water film to proceed during the formation of brucite from hydration of periclase, and our simulations show that the pressure where the water film remains stable is below a few tens of MPa.
- When the pressure reaches a few tens of MPa, the water film between grains collapses, a process which reduces the water film thickness and the self-diffusion coefficient of water molecules. The thickness of this water film is smaller than the hydration shell around Mg^{2+}-ions which will limit ion-transportation.
- The observed slowdown in reaction-induced fracturing in the periclase-brucite system above 30 MPa effective pressure can be explained by an insufficient hydration force. When the effective pressure increases to a few tens of MPa, the access to water inside the grain contact decreases and a thin water film layer limits ion-transfer to the reacting surface.
- Our results propose that the rate of reaction-induced fracturing could be limited by the access of water to the grain boundaries, limiting the chemical reaction there. This result provides an explanation of the slowdown of reaction-induced fracturing rate observed in experimental studies of the hydration of calcium and magnesium oxides.

Declaration of Competing Interest

The authors declare that they have no known competing financial interests or personal relationships that could have appeared to influence the work reported in this paper.

ACKNOWLEDGEMENT

B.J. received support from the European Union's Horizon 2020 Research and Innovation Programm under the ERC Advanced Grant Agreement no. 669972, 'Disequilibrium Metamorphism' ('DIME'). Some of the simulations were performed using computer resources provided by UNINETT Sigma2 - The National Infrastructure for High Performance Computing and Data Storage in Norway, project number NN9272K. We thank the Associate Editor Lawrence M. Anovitz and the three anonymous reviewers for their constructive reviews that improved our manuscript.

RESEARCH DATA

Research data associated with this article can be accessed from Zenodo at https://doi.org/10.5281/zenodo.3931763.

APPENDIX A. SUPPLEMENTARY MATERIAL

Supplementary data to this article can be found online at https://doi.org/10.1016/j.gca.2020.11.016.

REFERENCES

Allen M. P. and Tildesley D. J. (1987) *Computer Simulation of Liquids*. Oxford Science Publications.

Asaduzzaman A. (2020) The hydration of periclase: atomistic insights from quantum-chemical look. *Chem. Phys.* **532**. https://doi.org/10.1016/j.chemphys.2020.110694 110694.

Becker G. F. and Day A. L. (1916) Note on the linear force of growing crystals. *J. Geol.* **24**, 313–333. https://doi.org/10.1017/CBO9781107415324.004.

Berendsen H. J. C., Grigera J. R. and Straatsma T. P. (1987) The missing term in effective pair potentials. *J. Phys. Chem.* **91**, 6269–6271. https://doi.org/10.1021/j100308a038.

Bo J., Zhang Yife and Zhang Y (2017) Mechanism, kinetic model and hydrogen ion apparent diffusion coefficient in magnesium hydroxide dissolution by pressurized carbonated water. *React. Kinet. Mech. Catal.* **122**, 819–838. https://doi.org/10.1007/s11144-017-1230-y.

Bol W., Gerrits G. J. A. and van Panthaleon Eck C. L. (1970) The hydration of divalent cations in aqueous solution. An X-ray investigation with isomorphous replacement. *J. Appl. Crystallogr.* **3**, 486–492. https://doi.org/10.1107/s0021889870006738.

Brekke-Svaland G. and Bresme F. (2018) Interactions between hydrated calcium carbonate surfaces at nanoconfinement conditions. *J. Phys. Chem. C* **122**, 7321–7330. https://doi.org/10.1021/acs.jpcc.8b01557.

Catti M., Ferraris G., Hull S. and Pavese A. (1995) Static compression and H disorder in brucite, Mg(OH)2, to 11 GPa: a powder neutron diffraction study. *Phys. Chem. Miner.* **22**(3), 200–206. https://doi.org/10.1007/BF00202300.

Cygan R. T., Liang J.-J. and Kalinichev A. G. (2004) Molecular models of hydroxide, oxyhydroxide, and clay phases and the development of a general force field. *J. Phys. Chem. B* **108**, 1255–1266. https://doi.org/10.1021/jp0363287.

Correns C. W. (1949) Growth and dissolution of crystals under linear pressure. *Discuss. Faraday Soc.* **5**, 267–271.

Ding W., Palaiokostas M. and Orsi M. (2016) Stress testing the ELBA water model. *Mol. Simul.* **42**(4), 337–346. https://doi.org/10.1080/08927022.2015.1047367.

Duffy T. S., Shu J., Mao H. kwan and Hemley R. J. (1995) Single-crystal X-ray diffraction of brucite to 14 GPa. *Phys. Chem. Miner.* **22**(5), 277–281. https://doi.org/10.1007/BF00202767.

Dysthe D. K., Renard F., Porcheron F. and Rousseau B. (2002) Fluid in mineral interfaces – molecular simulations of structure and diffusion 13–1-13–4. *Geophys. Res. Lett.* **29**. https://doi.org/10.1029/2001GL013208.

Easteal A. J., Price W. E. and Woolf L. A. (1989) Diaphragm cell for high-temperature diffusion measurements. Tracer diffusion coefficients for water to 363 K. *J. Chem. Soc. Faraday Trans. 1* **85**(5), 1091–1097. https://doi.org/10.1039/F19898501091.

Engkvist O. and Stone A. J. (1999) Adsorption of water on the MgO(001) surface. *Surf. Sci.* **437**, 239–248. https://doi.org/10.1016/S0039-6028(99)00730-X.

Espinosa J. R., Sanz E., Valeriani C. and Vega C. (2014) Homogeneous ice nucleation evaluated for several water models. *J. Chem. Phys.* **141**(18). https://doi.org/10.1063/1.4897524.

Fukui H., Ohtaka O., Suzuki T. and Funakoshi K. (2003) Thermal expansion of Mg(OH)2 brucite under high pressure and pressure dependence of entropy. *Phys. Chem. Miner.* **30**(9), 511–516. https://doi.org/10.1007/s00269-003-0353-z.

Guevara-Carrion G., Vrabec J. and Hasse H. (2011) Prediction of self-diffusion coefficient and shear velocity of water and its binary mixtures with methanol and ethanol by molecular simulations. *J. Chem. Phys.* **134**. https://doi.org/10.1063/1.3515262.

Harlov D. and Austrheim H. (2012) *Metasomatism and the Chemical Transformation of Rock: The Role of Fluids in Terrestrial and Extraterrestrial Processes*. Springer Science & Business Media.

Holz M., Heil S. R. and Sacco A. (2000) Temperature-dependent self-diffusion coefficients of water and six selected molecular liquids for calibration in accurate 1H NMR PFG measurements. *Phys. Chem. Chem. Phys.* **2**, 4740–4742. https://doi.org/10.1039/b005319h.

Hövelmann J., Putnis C. V., Ruiz-Agudo E. and Austrheim H. (2012) Direct nanoscale observations of CO2 sequestration during brucite [Mg(OH)2] dissolution. *Environ. Sci. Technol.* **46**, 5253–5260. https://doi.org/10.1021/es300403n.

Israelachvili J. N. (2011) *Intermolecular and Surface Forces*, third ed. Academic Press, Amsterdam.

Iyer K., Jamtveit B., Mathiesen J., Malthe-Sørenssen A. and Feder J. (2008) Reaction-assisted hierarchical fracturing during serpentinization. *Earth Planet. Sci. Lett.* **267**(3–4), 503–516. https://doi.org/10.1016/j.epsl.2007.11.060.

Jamtveit B., Putnis C. V. and Malthe-Sørenssen A. (2009) Reaction induced fracturing during replacement processes. *Contrib. Mineral. Petrol.* **157**, 127–133. https://doi.org/10.1007/s00410-008-0324-y.

Jamtveit B. and Hammer Ø. (2012) Sculpting of rocks by reactive fluids. *Geochem. Perspect.* **1**(3), 341–491. https://doi.org/10.7185/geochempersp.1.3.

Jug K., Heidberg B. and Bredow T. (2007) Cyclic cluster study on the formation of brucite from periclase and water. *J. Phys. Chem. C* **111**, 13103–13108. https://doi.org/10.1021/jp072889c.

Kelemen P. B., Matter J., Streit E. E., Rudge J. F., Curry W. B. and Blusztajn J. (2011) Rates and mechanisms of mineral carbonation in peridotite: natural processes and recipes for enhanced, in situ CO 2 capture and storage. *Annu. Rev. Earth Planet. Sci.* **39**, 545–576. https://doi.org/10.1146/annurev-earth-092010-152509.

Kelemen P. B. and Hirth G. (2012) Reaction-driven cracking during retrograde metamorphism: olivine hydration and carbonation. *Earth Planet. Sci. Lett.* **345**, 81–89. https://doi.org/10.1016/j.epsl.2012.06.018.

Kilpatrick J. I., Loh S. H. and Jarvis S. P. (2013) Directly probing the effects of ions on hydration forces at interfaces. *J. Am. Chem. Soc.* **135**, 2628–2634. https://doi.org/10.1021/ja310255s.

Kuleci H., Schmidt C., Rybacki E., Petrishcheva E. and Abart R. (2016) Hydration of periclase at 350 °C to 620 °C and 200 MPa: experimental calibration of reaction rate. *Mineral. Petrol.* **110**, 1–10. https://doi.org/10.1007/s00710-015-0414-2.

Langmuir I. (1938) The role of attractive and repulsive forces in the formation of tactoids, thixotropic gels, protein crystals and coacervates. *J. Chem. Phys.* **6**, 873–896. https://doi.org/10.1063/1.1750183.

Larsen A. H., Mortensen J. J., Blomqvist J., Castelli I. E., Christensen R., Dułak M., Friis J., Groves M. N., Hammer B., Hargus C., Hermes E. D., Jennings P. C., Jensen P. B., Kermode J., Kitchin J. R., Kolsbjerg E. L., Kubal J., Kaasbjerg K., Lysgaard S., Maronsson J. B., Maxson T., Olsen T., Pastewka L., Peterson A., Rostgaard C., Schiøtz J., Schütt O., Strange M., Thygesen K. S., Vegge T., Vilhelmsen L., Walter M., Zeng Z. and Jacobsen K. W. (2017) The atomic simulation environment – a Python library for working with atoms. *J.*

Phys. Condens. Matter **29**. https://doi.org/10.1088/1361-648X/aa680e.

Lee S. H. and Rossky P. J. (1994) A comparison of the structure and dynamics of liquid water at Hydrophobic and hydrophilic surfaces – a molecular dynamics simulation study. *J. Chem. Phys.* **100**, 3334–3345. https://doi.org/10.1063/1.466425.

Lee J. H., Eun J. H., Kim S. G., Park S. Y., Lee M. J. and Kim H. J. (2003) Hydration behavior of MgO single crystals and thin films. *J. Mater. Res.* **18**, 2895–2903. https://doi.org/10.1557/JMR.2003.0404.

Malani A., Ayappa K. G. and Murad S. (2009) Influence of hydrophilic surface specificity on the structural properties of confined water. *J. Phys. Chem. B* **113**, 13825–13839. https://doi.org/10.1021/jp902562v.

Malvoisin B., Brantut N. and Kaczmarek M. A. (2017) Control of serpentinisation rate by reaction-induced cracking. *Earth Planet. Sci. Lett.* **476**, 143–152. https://doi.org/10.1016/j.epsl.2017.07.042.

Marmier A., Hoang P. N. M., Picaud S., Girardet C. and Lynden-Bell R. M. (1998) A molecular dynamics study of the structure of water layers adsorbed on MgO(100). *J. Chem. Phys.* **109**, 3245–3254. https://doi.org/10.1063/1.476915.

Martin B. and Fyfe W. S. (1970) Some experimental and theoretical observations on the kinetics of hydration reactions with particular reference to serpentinization. *Chem. Geol.* **6**, 185–202. https://doi.org/10.1016/0009-2541(70)90018-5.

Martinez M. J. and Martinez L. (2003) Packing optimization for automated generation of complex system's initial configurations for molecular dynamics and docking. *J. Comput. Chem.* **24**, 819–825.

Mills R. (1973) Self-diffusion in normal and heavy water in the range 1–45°. *J. Phys. Chem.* **77**, 685–688. https://doi.org/10.1021/j100624a025.

Nagai T., Hattori T. and Yamanaka T. (2000) Compression mechanism of brucite: an investigation by structural refinement under pressure. *Am. Mineral.* **85**(5–6), 760–764. https://doi.org/10.2138/am-2000-5-615.

Ostapenko G. T. (1976) Excess pressure on the solid phase generated by hydration (according to experimental data on hydration of periclase). *Geochemistry Int.*, 120–138.

Ou X., Li J. and Lin Z. (2014) Dynamic behavior of interfacial water on Mg(OH)2 (001) surface: a molecular dynamics simulation work. *J. Phys. Chem. C* **118**, 29887–29895. https://doi.org/10.1021/jp509373d.

Oviedo J., Calzado C. J. and Sanz J. F. (1998) Molecular dynamics simulations of the MgO (001) surface hydroxylation. *J. Chem. Phys.* **108**, 4219–4225. https://doi.org/10.1063/1.475820.

Parsegian V. A. and Zemb T. (2011) Hydration forces: observations, explanations, expectations, questions. *Curr. Opin. Colloid Interface Sci.* **16**, 618–624. https://doi.org/10.1016/j.cocis.2011.06.010.

Pavlov M., Siegbahn P. E. M. and Sandström M. (1998) Hydration of beryllium, magnesium, calcium, and zinc ions using density functional theory. *J. Phys. Chem. A* **102**, 219–228. https://doi.org/10.1021/jp972072r.

Phan A., Ho T. A., Cole D. R. and Striolo A. (2012) Molecular structure and dynamics in thin water films at metal oxide surfaces: magnesium, aluminum, and silicon oxide surfaces. *J. Phys. Chem. C* **116**, 15962–15973. https://doi.org/10.1021/jp300679v.

Plimpton S. (1995) Fast parallel algorithms for short-range molecular dynamics. *J. Comput. Phys.* **117**, 1–19. https://doi.org/10.1006/jcph.1995.1039.

Plümper O., Røyne A., Magrasó A. and Jamtveit B. (2012) The interface-scale mechanism of reaction-induced fracturing during serpentinization. *Geology* **40**, 1103–1106. https://doi.org/10.1130/G33390.1.

Pouvreau M., Greathouse J. A., Cygan R. T. and Kalinichev A. G. (2017) Structure of hydrated gibbsite and brucite edge surfaces: DFT results and further development of the ClayFF classical force field with metal-O-H angle bending terms. *J. Phys. Chem. C* **121**, 14757–14771. https://doi.org/10.1021/acs.jpcc.7b05362.

Putnis A. (2002) Mineral replacement reactions: from macroscopic observations to microscopic mechanisms. *Mineral. Mag.* **66**, 689–708. https://doi.org/10.1180/0026461026650056.

Putnis A. (2014) Why mineral interfaces matter. *Science* **343**, 1441–1442. https://doi.org/10.1126/science.1250884.

Renard F. and Ortoleva P. (1997) Water films at grain-grain contacts: Debye-Hückel, osmotic model of stress, salinity, and mineralogy dependence. *Geochim. Cosmochim. Acta* **61**, 1963–1970. https://doi.org/10.1016/S0016-7037(97)00036-7.

Refson K., Wogelius R. A., Fraser D. G., Payne M. C., Lee M. H. and Milman V. (1995) Water chemisorption and reconstruction of the MgO surface. *Phys. Rev. B* **52**, 10823–10826. https://doi.org/10.1103/PhysRevB.52.10823.

Ryckaert J. P., Ciccotti G. and Berendsen H. J. C. (1977) Numerical integration of the cartesian equations of motion of a system with constraints: molecular dynamics of n-alkanes. *J. Comput. Phys.* **23**, 327–341. https://doi.org/10.1016/0021-9991(77)90098-5.

Røyne A., Jamtveit B., Mathiesen J. and Malthe-Sørenssen A. (2008) Controls on rock weathering rates by reaction-induced hierarchical fracturing. *Earth Planet. Sci. Lett.* **275**, 364–369. https://doi.org/10.1016/j.epsl.2008.08.035.

Røyne A. and Jamtveit B. (2015) Pore-scale controls on reaction-driven fracturing. *Rev. Mineral. Geochem.* **80**, 25–44. https://doi.org/10.2138/rmg.2015.80.02.

Sakuma H., Tsuchiya T., Kawamura K. and Otsuki K. (2004) Local behavior of water molecules on brucite, talc, and halite surfaces: a molecular dynamics study. *Mol. Simul.* **30**(13–15), 861–871. https://doi.org/10.1080/08927020412331299350.

Sasaki S., Takeuchi Y. and Fujino K. (1979) X-Ray determination of electron-density distributions in oxides, MgO, MnO, CoO, and NiO, and atomic scattering factors of their constituent atoms. *Proc. Jpn. Acad. Ser. B Phys. Biol. Sci.* **55**, 43–48. https://doi.org/10.2183/pjab.55.43.

Scherer G. W. (2004) Stress from crystallization of salt. *Cem. Concr. Res.* **34**, 1613–1624. https://doi.org/10.1016/j.cemconres.2003.12.034.

Shen Z., Chun J., Rosso K. M. and Mundy C. J. (2018) Surface chemistry affects the efficacy of the hydration force between Two ZnO(1010) surfaces. *J. Phys. Chem. C* **122**, 12259–12266. https://doi.org/10.1021/acs.jpcc.8b02421.

Shinoda W., Shiga M. and Mikami M. (2004) Rapid estimation of elastic constants by molecular dynamics simulation under constant stress. *Phys. Rev. B – Condens. Matter Mater. Phys.* **69**(13), 16–18. https://doi.org/10.1103/PhysRevB.69.134103.

Stirniman M. J., Huang C., Smith R. S., Joyce S. A. and Kay B. D. (1996) The adsorption and desorption of water on single crystal MgO(100): the role of surface defects. *J. Chem. Phys.* **105**, 1295–1298. https://doi.org/10.1063/1.471993.

Tsimpanogiannis I. N., Moultos O. A., Franco L. F. M., Spera M. B. d. M., Erdős M. and Economou I. G. (2019) Self-diffusion coefficient of bulk and confined water: a critical review of classical molecular simulation studies. *Mol. Simul.* **45**, 425–453. https://doi.org/10.1080/08927022.2018.1511903.

Wang J., Kalinichev A. G. and Kirkpatrick R. J. (2004) Molecular modeling of water structure in nano-pores between brucite (001) surfaces. *Geochim. Cosmochim. Acta* **68**, 3351–3365. https://doi.org/10.1016/j.gca.2004.02.016.

Weyl P. K. (1959) Pressure solution and the force of crystallization: a phenomenological theory. *J. Geophys. Res.* **64**, 2001–2025. https://doi.org/10.1029/jz064i011p02001.

Wogelius R. A., Refson K., Fraser D. G., Grime G. W. and Goff J. P. (1995) Periclase surface hydroxylation during dissolution. *Geochim. Cosmochim. Acta* **59**, 1875–1881. https://doi.org/10.1016/0016-7037(95)00070-G.

Wolterbeek T. K. T., van Noort R. and Spiers C. J. (2018) Reaction-driven casing expansion: potential for wellbore leakage mitigation. *Acta Geotech.* **13**, 341–366. https://doi.org/10.1007/s11440-017-0533-5.

Yu H. and van Gunsteren W. F. (2004) Charge-on-spring polarizable water model revisited: from water clusters to liquid water on ice. *J. Chem. Phys.* **121**, 9549–9564. https://doi.org/10.1063/1.1805516.

Zeitler T. R., Greathouse J. A., Gale J. D. and Cygan R. T. (2014) Vibrational analysis of brucite surfaces and the development of an improved force field for molecular simulation of interfaces. *J. Phys. Chem. C* **118**, 7946–7953. https://doi.org/10.1021/jp411092b.

Zhang L., Nasika C., Donzé F. V., Zheng X., Renard F. and Scholtès L. (2019) Modeling porosity evolution throughout reaction-induced fracturing in rocks with implications for serpentinization. *J. Geophys. Res. Solid Earth* **124**, 5708–5733. https://doi.org/10.1029/2018JB016872.

Zheng X., Cordonnier B., Zhu W., Renard F. and Jamtveit B. (2018) Effects of confinement on reaction-induced fracturing during hydration of periclase. *Geochemistry. Geophys. Geosystems* **19**, 2661–2672. https://doi.org/10.1029/2017GC007322.

Zigan F. and Rothbauer R. (1967) Neutronenbeugungsmessungen am brucit. *Neues Jahrb. für Mineral. Monatshefte*, 137–143.

Associate editor: lawrence M Anovitz

APPENDIX

The Appendix contains three texts and eight figures. The first two texts present an additional method to calculate the effect of pressure on the water film thickness between two grains, and the corresponding results. The third text demonstrates that the ClayFF force field can be used at the pressure and temperature conditions in the present study. The first two figures show the method and result presented in the Appendix. Figure A3 show how the ClayFF properties correspond with experimental values. Figures A4-A8 support results discussed in the main text.

Text A.1 Additional Method

Section 2.2 describes the main method to move two interfaces towards each other with a constant pressure added by a global pressure tensor to a periodic solid with a water gap and allow the volume of the simulation domain to vary with time. An additional method is described here with the corresponding results that are consistent with the results in the main text. Unlike to the main method, the volume is kept constant and a solid is moved downward by adding a force to the atoms.

The *Periclase-nvt* simulations were run in the NVT ensemble (number of atoms, volume and temperature are constant), and the setup consists of one slab and one cuboid of periclase and water (Fig. A1). The slab is periodic in the x- and y-directions, the cuboid is located above the slab, and water molecules are filling the space between and around these two solids. To displace the cuboid towards the slab with time, we applied a constant downward force on each atom of the cuboid, following equation A1:

$$P_{wanted} = \frac{\sum F_{atom}}{A_{cube}} \quad \text{(A1)}$$

where P_{wanted} is the macroscopic pressure applied in the confined water film at the grain-grain interface, F_{atom} is the force applied on each atom in the cuboid and A_{cube} is the surface area of the cuboid (Fig. A1). The atoms in the bottom part of the slab are fixed, such that they keep the slab in position throughout the simulation.

The initial distance between the slab and cuboid was 15 Å, and the dimensions are 40x40x5 unit cell repetition for the slab and 9x9x9 for the cuboid. The simulations were performed at pressures in the range 10-100 MPa at 453 K. In laboratory experiments of reaction-induced fracturing (e.g. Zheng et al., 2018), the periclase to brucite reaction occurred not only on crystallographic planes but also on other surfaces of the grains. Therefore, we developed a procedure to build cuboids with faces with different orientations (Fig. A1c). To prepare surfaces

at different angles from the (100) periclase surface, the cuboid was rotated around the x- or z-axis with angles between 0.5° and 45° and a surface was cut (Fig. A1c). These surfaces of the rotated cuboid are not atomically flat. They contain a roughness at the atomic scale larger than if the surfaces had been cut along preexisting crystallographic planes.

For these simulations, we report the duration required to reach a water film thickness of one or two water layers. We observe that the last two layers of water are never removed, because of the strong binding of water molecules to the periclase surfaces.

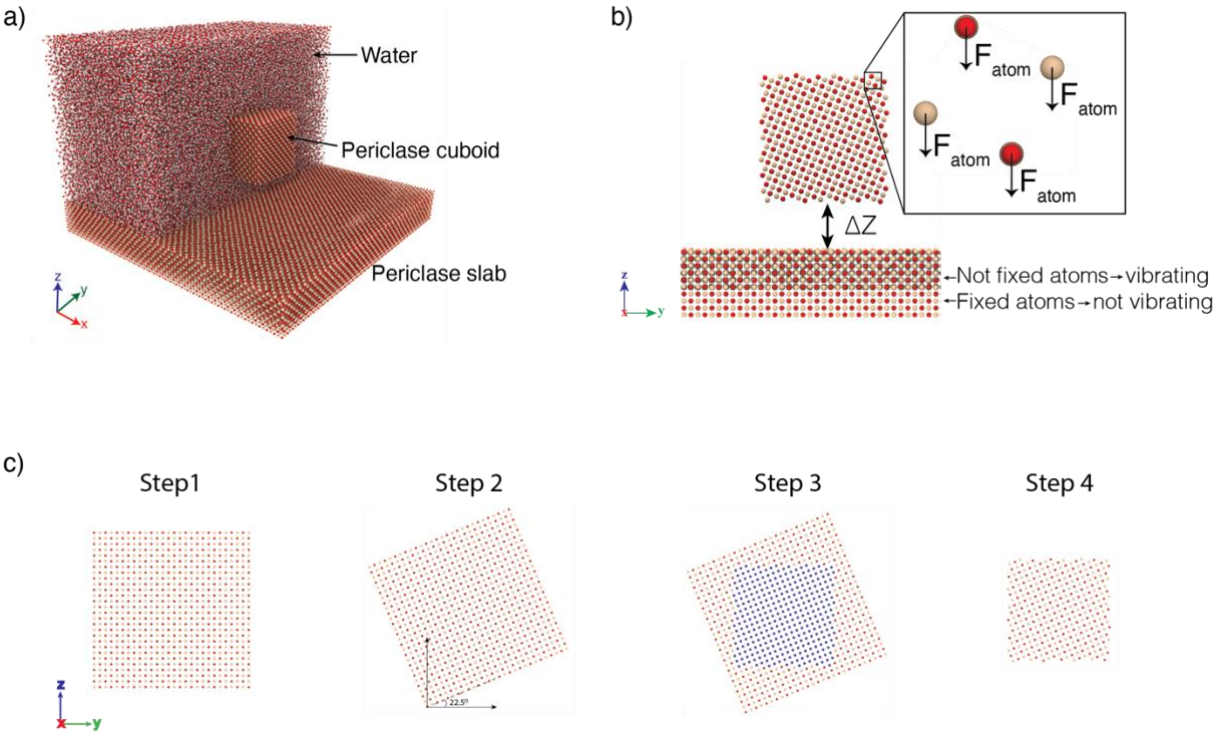

Figure A1. Molecular dynamics setups for the *Periclase-nvt* simulations. The setup consists of a mineral slab at the bottom of the simulation domain, a cuboid placed at a given distance above the slab, and water that fills the remaining volume. The slab is periodic in the x- and y-directions. a) Overview of the simulation domain where half of the water molecules is removed such that the periclase cuboid is visible. b) Simulation procedure for the NVT simulations. An external force (F_{atom}) is applied in the downward direction on each atom of the periclase cuboid. The cuboid is rotated to illustrate a rough surface, the slab is cut in the x-direction and water is removed for clarity. The atoms at the bottom of the slab are frozen to keep the slab at a fixed position through the simulation. c) Sketch of the procedure developed to create a periclase cuboid with different surface orientations in periclase. Step 1: Creation of a crystal cuboid larger than the final cuboid. Step 2: Rotation of the cuboid of 22.5°. Step 3: Selection of a smaller cuboid of the desired dimension that is then used for the simulations. The faces of the new cuboid do not follow crystallographic planes.

Text A.2 Additional Results

The duration to reach a water layer thickness of two water layers is close to 3 ns (Fig. A2). At pressures lower than 30 MPa, this duration varies depending on the crystallographic orientation, from up to 12 ns when the surface is the crystallographic plane (100) of periclase, to 3-10 ns when the cuboid surface is produced by rotation around the z-axis, to 2-4 ns for a rotation around the x-axis, which has a rougher surface. Above 30 MPa the duration required to reduce the water film thickness to two water layers is lower than 3 ns, whatever the crystallographic orientation.

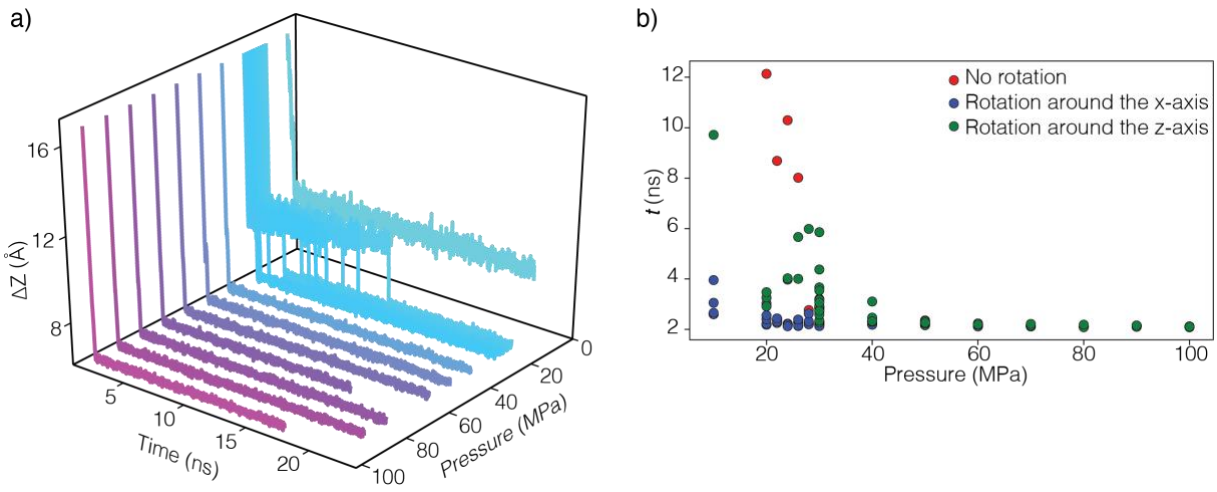

Figure A2. *Periclase-nvt* simulations (see Fig. A1 for geometry). a) Evolution of the thickness (ΔZ) of the water film with time and pressure. Each line displays one simulation at a given pressure. The color-coding is changing with pressure from 10 (light blue) to 100 (purple) MPa and shows a transition in behavior at around 30 MPa. b) Time (t) in each simulation to reach a thickness of two water layers depending on the rotation angle of the periclase cuboid around the (100) crystallographic plane.

Text A.3 ClayFF at higher pressures and temperatures

To justify that we can use the ClayFF force field at pressures up to 100 MPa and temperatures in the range 300-519 K, we calculated the unit cell parameters of brucite in the pressure range 0-1.5 GPa and temperature range 300-700 K (Fig. A3), and compared the results with experimentally measured values in the same pressure and temperature ranges (Catti et al., 1995; Duffy et al., 1995; Nagai et al., 2000; Fukui et al., 2003). We observe that the accuracy of the lattice parameters are similar under ambient conditions and up to pressures and temperatures that exceeds the conditions in our simulations. There is a small shift less than 5 % in the unit cell length of the a-axis, but this shift remains rather constant for different pressures. We observe a slightly elevated thermal expansion of ClayFF compared to experiments, but the

absolute effect on the lattice parameters is very small, so we do not expect this to be an issue when computing properties of brucite and water in contact.

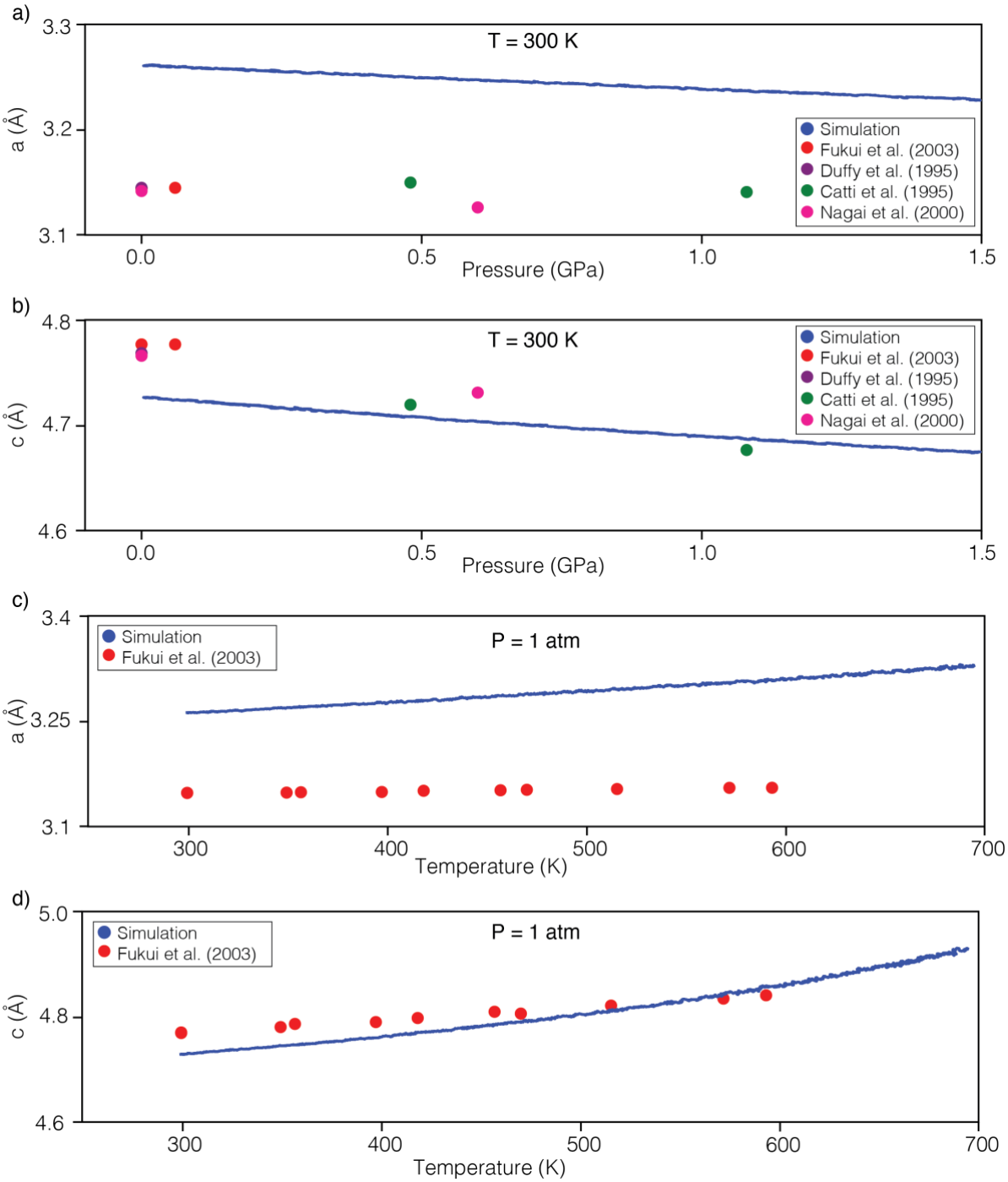

Figure A3. Unit cell parameters for brucite in the pressure range 0-1.5 GPa and temperature range 300-700 K. Changes in the a-axis (a) and c-axis (b) parameter at temperature 300 K in the range 0-1.5 GPa, compared with experimental values from four different studies. Changes in the a-axis (c) and c-axis (d) parameter at a pressure of 0 GPa and in the pressure range 300-700 K.

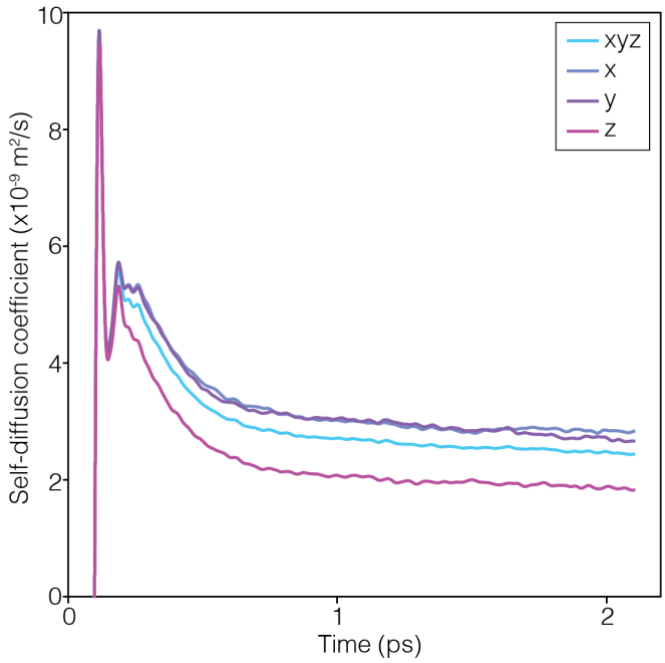

Figure A4. Self-diffusion coefficients of water molecules between brucite surfaces calculated from velocity autocorrelation function. The values are taken when a plateau is reached after 2 ps. The bulk diffusion coefficient of the water molecules (xyz), and the diffusion coefficients in the x-, y- and z-directions are plotted separately. The diffusion in x- and y-directions is higher than in the z-direction.

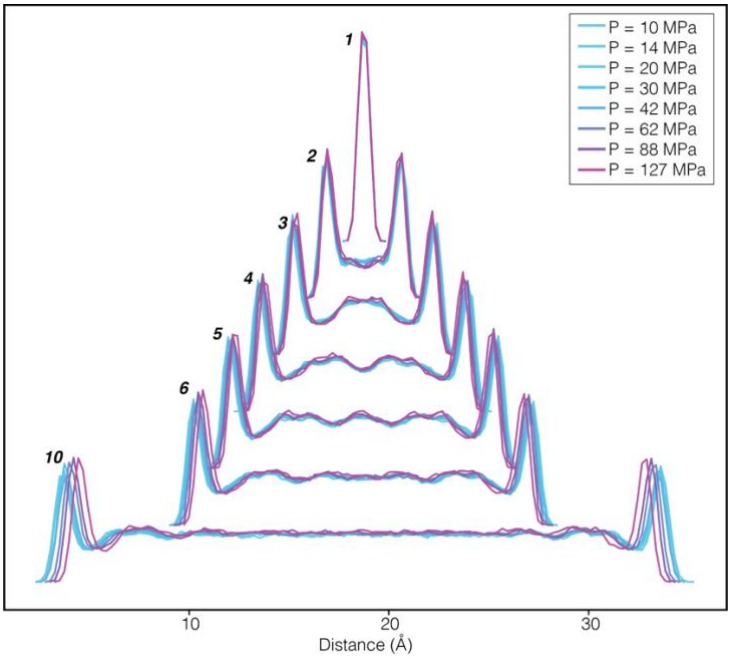

Figure A5. Atomic density profiles of hydrogen atoms in a water film confined between brucite surfaces. Similar profiles for oxygen atoms are displayed in Fig. 4a.

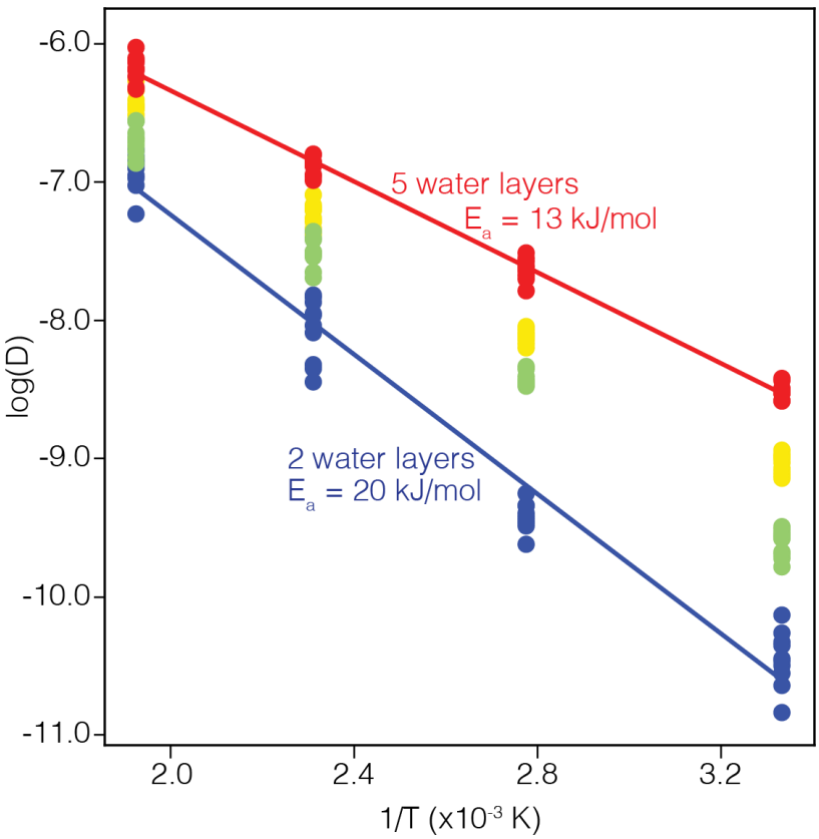

Figure A6. Diffusion coefficient as a function of 1/T for two (dark blue) to five (red) water layers between periclase surfaces. E_a=activation energy. Fig. 4b displays a similar plot for brucite.

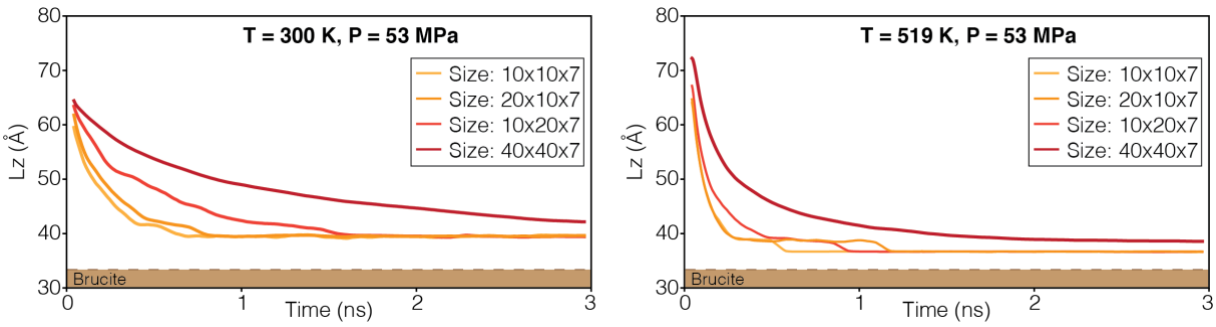

Figure A7. Thickness (Lz) of the simulation domain in the z-direction as a function of time in the *Brucite-squeeze* simulations (see Fig. 3a for the geometry). Evolution of the water film thickness as a function of time for four different sizes of the brucite slab at a constant pressure (53 MPa) and at two temperatures (300 and 519 K).

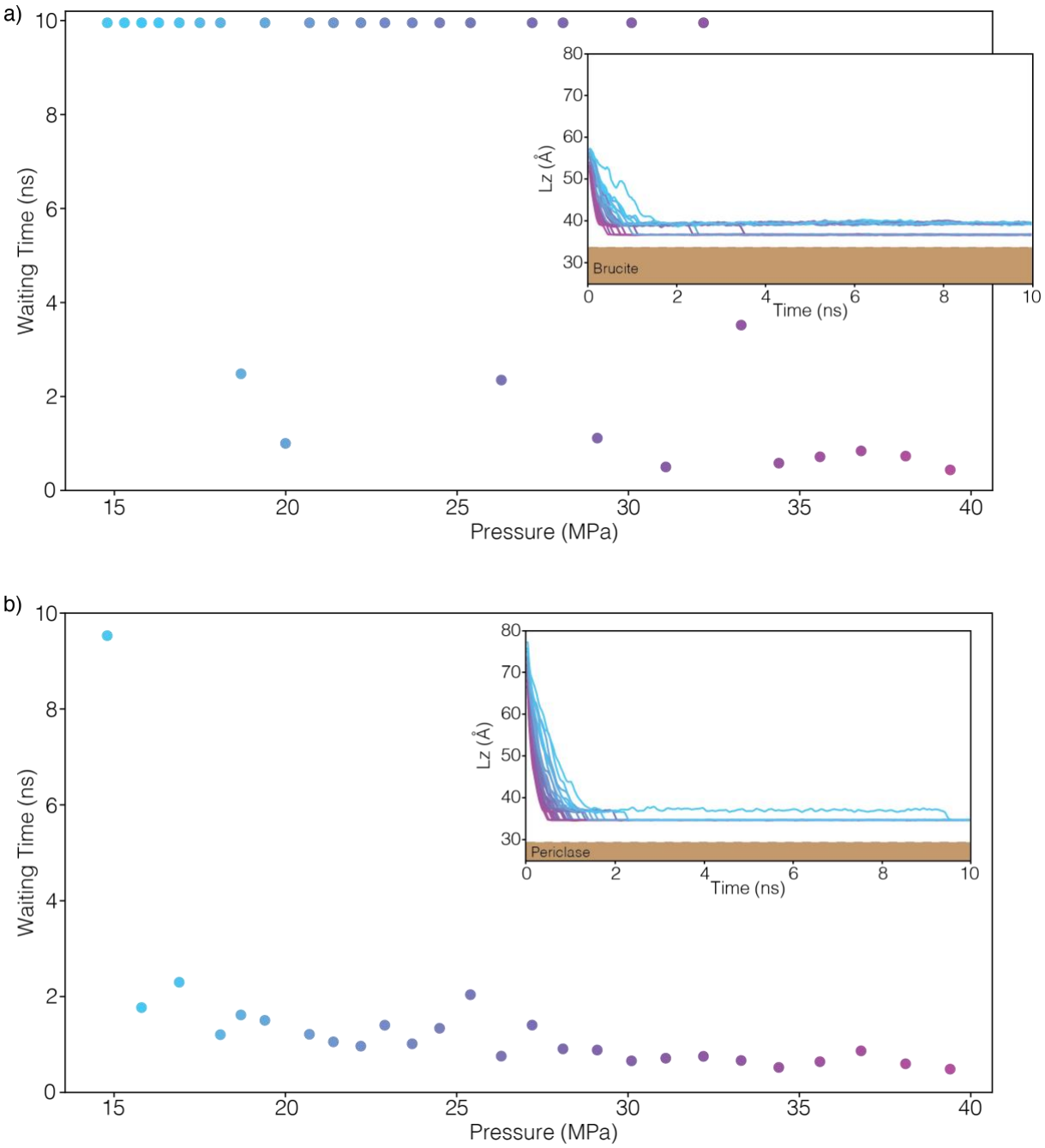

Figure A8. Waiting time to reach two water layers for simulations in the pressure range 15-40 MPa at 519 K for a) the *Brucite*-squeeze simulations with and initial distance of 17 Å and b) the *Periclase-squeeze* simulations. The inset shows how the thickness (Lz) of the simulation domain change as a function of time during 10 ns.